https://doi.org/10.15388/vu.thesis.1024
https://orcid.org/0000-0002-8412-0020

VILNIUS UNIVERSITY
CENTER FOR PHYSICAL SCIENCES AND TECHNOLOGY

Mykola Koliada

Magnetoresistive Properties of Nonstoichiometric Lanthanum Manganite Films and Hybrid Manganite–Graphene Structures for Magnetic Sensors Development

DOCTORAL DISSERTATION

Natural Sciences,
Physics, N 002

VILNIUS 2026

This dissertation was prepared between 2020 and 2026 at the Center for Physical Sciences and Technology.

Academic supervisor:
Prof. Dr. Nerija Žurauskienė (Center for Physical Sciences and Technology, Natural Sciences, Physics, N 002).

This doctoral dissertation will be defended in a public meeting of the Dissertation Defence Panel:
Chairman – Prof. Dr. Jonas Gradauskas (Center for Physical Sciences and Technology, Natural Sciences, Physics, N 002).
Members:
Assoc. Prof. Dr. Zigmas Balevičius (Center for Physical Sciences and Technology, Natural Sciences, Physics, N 002).
Prof. Dr. Jurij Novickij (Vilnius Gediminas Technical University, Technological Sciences, Electrical and Electronics Engineering, T 001).
Dr. Pāvels Onufrijevs (Riga Technical University, Latvia, Natural Sciences, Physics, N 002)
Dr. Paulius Ragulis (Center for Physical Sciences and Technology, Natural Sciences, Physics – N 002).

The dissertation shall be defended at a public meeting of the Dissertation Defence Panel at 10:00 on 18 of December, 2026 in the meeting room D401 of the Center for Physical Sciences and Technology.
Address: Saulėtekio ave. 3, Vilnius, Lithuania.
Tel. +370 645 15550; e-mail: info@ftmc.lt

https://doi.org/10.15388/vu.thesis.1024
https://orcid.org/0000-0002-8412-0020

VILNIAUS UNIVERSITETAS
FIZINIŲ IR TECHNOLOGIJOS MOKSLŲ CENTRAS

Mykola Koliada

Nestechiometrinių lantano manganito sluoksnių ir hibridinių manganito–grafeno struktūrų magnetovaržinės savybės magnetinio lauko jutiklių kūrimui

DAKTARO DISERTACIJA

Gamtos mokslai,
Fizika, N 002

VILNIUS 2026

Disertacija rengta 2020–2026 metais Fizinių ir technologijos mokslų centre.

Mokslinė vadovė:
prof. dr. Nerija Žurauskienė (Fizinių ir technologijos mokslų centras, gamtos mokslai, fizika – N 002)

Gynimo taryba:
Pirmininkas – prof. dr. Jonas Gradauskas (Fizinių ir technologijos mokslų centras, gamtos mokslai, fizika, N 002).
Nariai:
doc. dr. Zigmas Balevičius (Fizinių ir technologijos mokslų centras, gamtos mokslai, fizika, N 002);
prof. dr. Jurij Novickij (Vilniaus Gedimino technikos universitetas, technologijos mokslai, elektros ir elektronikos inžinerija, T 001);
dr. Pāvels Onufrijevs (Rygos technikos universitetas, Latvija, gamtos mokslai, fizika, N 002);
dr. Paulius Ragulis (Fizinių ir technologijos mokslų centras, gamtos mokslai, fizika, N 002).

Disertacija ginama viešame Gynimo tarybos posėdyje 2026 m. gruodžio mėn. 18 d. 10 val. Fizinių ir technologijų mokslų centro posėdžių salėje D401.
Adresas: Saulėtekio al. 3, Vilnius, Lietuva.
Tel. +370 645 15550; el. paštas: info@ftmc.lt

LIST OF ABBREVIATIONS

2D – Two-dimensional;
AFM – Atomic force microscopy;
AMR – Anisotropic magnetoresistance;
CMR – Colossal magnetoresistance;
CNI – Spin-canted insulator;
DE – Double exchange;
EDX – Energy-dispersive X-ray spectroscopy;
FI – Ferromagnetic insulator;
FM – Ferromagnetic metal;
GB – Grain boundary;
GMR – Giant magnetoresistance;
HFMR – High-field magnetoresistance;
HRTEM – High resolution TEM;
ICP-MS – Inductively coupled plasma high-resolution mass spectrometry;
KWW – Kohlrausch-Williams-Watts;
LAO – $LaAlO_3$;
LFMR – Low-field magnetoresistance;
LMR – Linear magnetoresistance;
LSMCO or La-Sr-Mn-Co-O – Lanthanum strontium manganite-cobaltite oxide;
LSMO or La-Sr-Mn-O – Lanthanum strontium manganite oxide, $La_{1-x}Sr_xMn_yO_3$;
MC – Magnetoconductance;
MOCVD – Metal-organic chemical vapour deposition;
MR – Magnetoresistance;
MRA – Magnetoresistance anisotropy;
PI MOCVD – Pulse-injection MOCVD;
PI – Paramagnetic insulator;
PM – Paramagnetic metal;
PMMA – Poly(methyl methacrylate) polymer;
RF – Relaxation function;
SEM – Scanning electron microscopy;
SLG – Single-layer graphene;
STEM-EDX – Scanning TEM;
TEM – Transmission electron microscopy;
TMR – Tunnelling magnetoresistance;
VRH – Variable range hopping.

CONTENT

INTRODUCTION 9
Motivation and problem formulation of the work 9
The aim of this work 10
The tasks of the work 10
Scientific novelty 11
Practical significance 11
Statements for defence 12
Author's contribution 12
Structure of the dissertation 13
Acknowledgement 13
LIST OF PUBLICATIONS 14
1. REVIEW OF PHYSICAL PROPERTIES OF LANTHANUM MANGANITES AND GRAPHENE 16
1.1 Crystallographic structure 16
1.2 Electronic structure 17
1.3 Electrical conductivity 18
1.3.1 Double exchange model 18
1.3.2 Metal-insulator transition 19
1.4 Colossal magnetoresistance of manganites 19
1.4.1 Magnetoresistance of high quality (crystals or epitaxial films) manganites 19
1.4.2 Magnetoresistance of polycrystalline manganites 22
1.4.2.1 Low-field magnetoresistance 23
1.4.2.2 High-field magnetoresistance 25
1.5 Sensors based on colossal magnetoresistance effect 30
1.6 Ageing behaviour of manganite films 32
1.7 Magnetism of graphene 35
1.7.1 Magnetoresistance of graphene 35
1.7.2 Magnetic sensors based on graphene 39
2. PREPARATION OF SAMPLES AND MEASUREMENT METHODOLOGY 42
2.1 Preparation of samples and their characterisation 42
2.1.1 Deposition of La-Sr-Mn-O films by using PI MOCVD 42
2.1.2 Graphene transfer procedure 43
2.1.3 Characterisation of graphene and manganite structure 44
2.2 Measurement equipment and methods 44
2.2.1 Resistivity and low-field magnetoresistance measurement system 44

2.2.2 Measurement system of magnetoresistance dependence on field direction 45
2.2.3 Measurement of magnetoresistance in high magnetic fields 46
3. RESULTS AND DISCUSSION 47
3.1 Magnetoresistance of nanostructured lanthanum manganite films 47
3.1.1 Morphology and microstructure of LSMO films 47
3.1.2 Resistivity and metal-insulator transition temperature of nanostructured LSMO films: dependence on Sr content and excess of Mn 49
3.1.3 Magnetoresistance of nanostructured LSMO films 51
3.2 Accelerated ageing of nonstoichiometric LSMO films 57
3.2.1 Structural and compositional characterisation of the LSMO films 58
3.2.2 Influence of accelerated ageing on resistivity 60
3.2.3 Influence of ageing on magnetoresistance 63
3.3 Magnetoresistive properties of lanthanum manganite-graphene nanostructures 65
3.3.1 Characterisation of graphene 65
3.3.2 Characterisation of LSMO manganite film 66
3.3.3 Magnetoresistance of graphene 68
3.3.4 Magnetoresistance of manganite 70
3.3.5 Design and fabrication of a hybrid lanthanum manganite-graphene sensor 71
3.3.6 Testing results of hybrid sensor 72
GENERAL CONCLUSIONS 79
SANTRAUKA 81
ĮVADAS 81
Darbo motyvacija ir problemos formulavimas 81
Darbo tikslas 82
Darbo uždaviniai 83
Mokslinis naujumas 83
Praktinė reikšmė 84
Ginamieji teiginiai 84
Autoriaus indėlis 85
Disertacijos struktūra 85
1. LANTANO MANGANITŲ IR GRAFENO FIZIKINIŲ SAVYBIŲ APŽVALGA 86
2. BANDINIŲ PARUOŠIMAS IR MATAVIMO METODIKA 86
2.1 Bandinių paruošimas ir jų charakterizavimas 86
2.1.1 La-Sr-Mn-O sluoksnių nusodinimas PI MOCVD metodu 86
2.1.2 Grafeno perkėlimo procedūra 88
2.1.3 Grafeno ir manganito struktūros charakterizavimas 88

2.2 Matavimo aparatūra ir metodai 89
2.2.1 Savitosios varžos ir silpno magnetinio lauko magnetovaržos matavimo sistema 89
2.2.2 Magnetovaržos priklausomybės nuo magnetinio lauko krypties matavimo sistema 90
2.2.3 Magnetovaržos matavimo sistema esant stipriems magnetiniams laukams 91
3. REZULTATAI IR JŲ APTARIMAS 92
3.1 Nanostruktūrizuotų lantano manganito sluoksnių magnetovarža 92
3.1.1 LSMO sluoksnių morfologija ir mikrostruktūra 92
3.1.2 Nanostruktūrizuotų LSMO sluoksnių savitosios varžos ir metalo-izoliatoriaus virsmo temperatūros priklausomybė nuo Sr kiekio ir Mn pertekliaus 93
3.1.3 Nanostruktūrizuotų LSMO sluoksnių magnetovarža 94
3.2 Nestechiometrinių LSMO sluoksnių pagreitintas sendinimas 98
3.2.1 Pagreitinto sendinimo įtaka savitajai varžai 98
3.2.2 Pagreitinto sendinimo įtaka magnetovaržai 102
3.3 Lantano manganito-grafeno struktūrų magnetovaržinės savybės 103
3.3.1 Grafeno magnetovarža 104
3.3.2 Manganito magnetovarža 105
3.3.3 Hibridinio lantano manganito-grafeno jutiklio kūrimas 106
3.3.4 Hibridinio jutiklio testavimo rezultatai 107
BENDROSIOS IŠVADOS 111
REFERENCES 113
Curriculum Vitae 124

INTRODUCTION

Motivation and problem formulation of the work

The precise detection and measurement of magnetic fields is crucial for a wide range of applications [1]. These include magnetometry, magnetic storage, automation and various industries such as automotive industry. Modern advances require sensors that are not only highly sensitive, but also compact and efficient over a wide temperature range. Different applications have different requirements in terms of sensitivity, temperature and magnetic field ranges, accuracy, etc. Commercially available magnetoresistive (MR) sensors (tunnelling TMR, giant GMR, anisotropic AMR and others) have a high sensitivity in the range of weak magnetic fields (less than 1 T) and are used to measure magnetic fields in this range [2]. At stronger fields, however, their response saturates and, therefore, these sensors can not be used for higher field measurements. This limitation is particularly important for advanced magnetic field generation systems [3], which extend the field range used for scientific, industrial and medical applications. These applications require sensors that are able to measure magnetic fields over a broad range and at different temperatures, while simultaneously determining the direction of these fields and tracking their changes. Therefore, the selection of materials with special properties and the design of effective sensor elements are crucial in the development of sensors operating in a wide magnetic field range [4].

Among the various materials being researched, manganites and graphene have proven to be particularly promising candidates due to their unique magnetoresistive properties at high magnetic fields [5, 6, 7, 8]. In a recent study [9], a hybrid sensor combining single-layer graphene (SLG) and a thin nanostructured manganite film of $La_{0.8}Sr_{0.2}MnO_3$ (LSMO) was proposed. In this sensor, the SLG and LSMO elements were arranged in a voltage divider configuration, utilizing two different effects of the nanomaterials. Nanostructured manganite films consisting of polycrystalline grains exhibit negative colossal magnetoresistance (CMR) effect and are sensitive to magnetic fields over a wide temperature (4–320 K) and magnetic field ranges (from millitesla up to hundred Teslas) [10]. This sensitivity is attributed to the mechanism of double exchange, which increases conductivity when the magnetic moments of the manganese ions align with an external field. In addition, these films are relatively insensitive to the direction of the magnetic field at high intensities, making them ideal for B-scalar sensor applications [11]. Moreover, previous studies have shown that nonstoichiometric lanthanum manganite $La_{1-x}Sr_xMn_yO_3$ films with manganese

excess ratio $y = \mathrm{Mn}/(\mathrm{La} + \mathrm{Sr}) > 1$ have shifted metal-insulator transition temperature T_m to higher temperatures and reduced the resistivity maximum, improving magnetoresistive performance at higher than room temperatures [12]. However, there is a lack of studies on how nonstoichiometric chemical composition influences the stability of resistivity and magnetoresistive properties of the films.

Graphene, a two-dimensional zero-gap semiconductor, also shows remarkable potential for magnetic field sensing [8,9]. It has extremely high carrier mobility and resistance change in a magnetic field based on the positive magnetoresistance phenomenon induced by the Lorentz force. It was also demonstrated that the combination of two sensors, in which the graphene layer has a large positive magnetoresistance while the nanostructured manganite-cobaltite (LSMCO) film has a negative colossal magnetoresistance, leads to a significant increase in sensitivity compared to single few-layer graphene and LSMCO sensors [13]. Moreover, in contrast to nanostructured manganite, which has an isotropic response to the field direction at large fields (above 0.5 T), graphene's magnetoresistance strongly depends on the direction of the field. Therefore, the investigation of lanthanum manganite and graphene magnetoresistive properties and their optimisation for the development of modern magnetic field sensors with extended application areas is of great importance.

The aim of this work

To investigate the features of negative magnetoresistance of nonstoichiometric lanthanum manganite $La_{1-x}Sr_xMn_yO_3$ films and positive magnetoresistance of graphene, and to develop compact hybrid manganite-graphene sensor exhibiting higher sensitivity than individual graphene or manganite sensors, and extended functionality by enabling measurement of both magnitude and direction of the magnetic field with respect to the plane of the hybrid structure.

The tasks of the work

1. To investigate how chemical composition of nonstoichiometric $La_{1-x}Sr_xMn_yO_3$ films grown on polycrystalline Al_2O_3 substrate influences the magnetoresistance of these films in a wide range of temperatures (5–300 K) and magnetic fields (up to 20 T).
2. To investigate influence of accelerated thermal ageing on nonstoichiometric $La_{1-x}Sr_xMn_yO_3$ film properties and identify optimal

conditions which could be used to stabilize resistance and magnetoresistance of these films.

3. To study positive magnetoresistance of graphene in low (0.1–2.4 T) and high (up to 20 T) magnetic fields at room temperature.
4. To fabricate hybrid nonstoichiometric lanthanum manganite-graphene structure and to investigate how negative magnetoresistance of manganite and positive magnetoresistance of graphene, and zero-field resistances of the single manganite and graphene elements influence the magnetoresistive properties of the hybrid structure.
5. To develop high pulsed magnetic field sensor based on hybrid manganite-graphene structure capable to measure magnetic field magnitude and direction with respect to the sensor's plane.

Scientific novelty

1. The impact of chemical composition on metal-insulator transition temperature and magnetoresistance in nonstoichiometric $La_{1-x}Sr_xMn_yO_3$ films grown on polycrystalline Al_2O_3 substrates was investigated across temperatures from 5 to 300 K and magnetic fields up to 20 T, and the mechanisms responsible for the resulting characteristics were identified.
2. The main mechanisms responsible for accelerated thermal ageing at 100°C of nonstoichiometric $La_{1-x}Sr_xMn_yO_3$ films were identified and optimal conditions which could be used to stabilize resistance and magnetoresistance of these films were determined.
3. A hybrid nonstoichiometric lanthanum manganite-graphene structure was fabricated, and its magnetoresistive properties were investigated for the development of high-pulsed magnetic field sensor capable to measure magnetic field magnitude and direction to sensor's plane.

Practical significance

A high-pulsed magnetic field sensor based on hybrid nonstoichiometric lanthanum manganite-graphene structure was developed and its properties were investigated and optimized for the measurement of both the magnitude and direction of magnetic field relative to the sensor's plane. This novel sensor is important for the high-power industrial applications when magnetic field direction is not known in advance.

Statements for defence

1. In nonstoichiometric $La_{1-x}Sr_xMn_yO_3$ films ($y \geq 1.05$) deposited on polycrystalline Al_2O_3 substrates, the metal-insulator transition temperature reaches a maximum at x = 0.15–0.18 within the compositional range $0.05 \leq x \leq 0.3$ (at y = 1.05) and can be further elevated by increasing the Mn excess y. Raising y to 1.15 produces a twofold enhancement of room-temperature low-field magnetoresistance in applied fields of 50–100 mT.
2. Accelerated thermal ageing of nonstoichiometric $La_{1-x}Sr_xMn_yO_3$ films in argon atmosphere at 100°C causes a monotonic increase in room-temperature resistance, which follows a stretched-exponential growth law and tends to saturation after approximately 20 hours. The stretched-exponential kinetics are consistent with relaxation in topologically disordered systems and identify oxygen release and redistribution at grain boundaries as the primary ageing mechanism, rather than Mn-excess-induced disorder within the crystallites. This interpretation is corroborated by the magnetoresistance remaining unchanged within 5% throughout the ageing process.
3. A hybrid nonstoichiometric manganite-graphene structure – Al_2O_3//$La_{1-x}Sr_xMn_yO_3$/Al_2O_3/Graphene, connected as a voltage divider, enables simultaneous measurement of both the magnitude and the out-of-plane angle of an external magnetic field. The field range of peak sensitivity is governed by the ratio $k = R_{Gr}/R_{Man}$ of the zero-field resistances of the graphene and manganite elements, providing a practical means to tune the sensor to a chosen operating field range, with peak sensitivity of approximately 60 mV/(V·T) achieved at 0.9–2.5 T obtained in this work for k = 0.23.

Author's contribution

All the results presented in this dissertation were obtained by the author together with the co-authors of the articles. The author performed preparations for the experiments, carried out experiments investigating the transport and magnetoresistive properties of LSMO and graphene films in the whole temperature and magnetic field range, and processing of the obtained data. The interpretation and analysis of these results was done by the author together with the academic supervisor and co-authors.

Structure of the dissertation

The dissertation consists of an introduction, three main chapters, general conclusions, references, and list of publications. The main three chapters are the following: literature review, description of samples preparation and measurement setup, obtained results and their analysis.

Acknowledgement

At first, I would like to thank my supervisor Nerija Žurauskiene for supervising my work during all PhD studies and her help and support.

I am grateful to all colleagues in the laboratory, especially to Skirmantas Keršulis, Vakaris Rudokas, Voitech Stankevič. Many thanks to Valentina Plaušinaitienė and Milita Vagner for preparation of thin films and help with interpretation of characterisation results of lanthanum manganites.

I would like to thank my family and friends in Ukraine and Lithuania for continues support and understanding.

LIST OF PUBLICATIONS

Basis of the thesis

[P1] Zurauskiene, N.; Stankevic, V.; Kersulis, S.; Vagner, M.; Plausinaitiene, V.; Dobilas, J.; Vasiliauskas, R.; Skapas, M.; Koliada, M.; Pietosa, J.; Wisniewski, A., Enhancement of Room-Temperature Low-Field Magnetoresistance in Nanostructured Lanthanum Manganite Films for Magnetic Sensor Applications. *Sensors*, 2022, 22, 4004. DOI: 10.3390/s22114004.

[P2] Rudokas, V.; Koliada, M.; Stankevič, V.; Keršulis S.; Vertelis, V.; Tolvaišienė, S.; Skapas, M.; Vagner, M.; Plaušinaitienė, V. and Žurauskienė, N., Stabilization of Transport Properties in Thin Nonstoichiometric $La_{1-x}Sr_xMn_yO_3$ Films via Accelerated Ageing for Magnetic Field Sensors, *Sensors*, 2026, 26, 2711. DOI: 10.3390/s26092711.

[P3] Žurauskienė, N.; Stankevič, V.; Keršulis, S.; Vertelis, V.; Koliada, M.; Rudokas, V.; Skapas, M.; Vagner, M.; Plaušinaitienė, V.; Guobienė, A.; Meškinis, Š., Hybrid manganite-graphene sensor for magnetic field magnitude and direction measurement, *Scientific Reports*, 2025, 15, 9100. DOI: 10.1038/s41598-025-94248-y.

List of conference presentations

C1 M. Koliada, N. Žurauskienė, R. Lukošė, S. Keršulis, V. Stankevič, V. Plaušinaitienė, M. Vagner, S. Balevičius. Hybrid magnetoresistive sensor based on manganite-graphene structure prepared on Al_2O_3 substrate. 44th Lithuanian National Physics Conference, Vilnius, October 6-8, 2021.

C2 M. Koliada, V. Rudokas, M. Vagner, K. Motiejuitis, V. Stankevič, V. Plaušinaitienė, N. Žurauskienė. Investigation of Long-Term Stability of Resistivity and Magnetoresistance of Nanostructured La-Sr-Mn-Co-O Films. 23rd International Conference-School "Advanced Materials and Technologies" Palanga, August 23-27, 2021.

C3 N. Žurauskienė, S. Keršulis, V. Rudokas, M. Vagner, K. Motiejuitis, M. Koliada, V. Stankevič, D. Pavilonis, V. Plaušinaitienė, Influence of Preparation Conditions on Long-Term Stability of Magnetoresistive Properties of Nanostructured La-Sr-Mn-Co-O Films Grown by PI MOCVD, INTERMAG-2021, Virtual conference, April 26-30, 2021.

C4 M. Koliada, N. Žurauskienė, S. Keršulis, V. Stankevič, M. Vagner, V. Plaušinaitienė, J. Dobilas, R. Vasiliauskas, M. Skapas. Enhancement of room-temperature low-field magnetoresistance in nanostructured lanthanum

manganite films for magnetic sensor applications. 12th Conference of Doctoral Students and Young Scientists FizTeCh-2022, Vilnius, October 19 – 20, 2022.

C5 A. Guobiene, M. Koliada, S. Keršulis, V. Stankevič, V. Vertelis, V. Plaušinaitienė, Š. Jankauskas, Š. Meškinis, N. Žurauskienė. Graphene-manganite structures for magnetic sensors applications. European Material Research Society EMRS 2022 Spring meeting, online May 30 - June 3, 2022.

C6 M. Koliada, N. Žurauskienė. Graphene-manganite structures for magnetic sensors applications. 13th Conference of Doctoral Students and Young Scientists FizTeCh-2023, Vilnius, October 18-19, 2023.

C7 N. Zurauskiene, V. Stankevic, S. Kersulis, V. Vertelis, M. Koliada, V. Rudokas, M. Skapas, M. Vagner, V. Plausinaitiene, A. Guobiene, S. Meskinis, Development of hybrid manganite-graphene sensor for measurement of magnetic field magnitude and direction, Joint European Magnetic Symposia JEMS, Frankfurt, August 24-29, 2025.

C8 V. Vertelis, V. Rudokas, M. Koliada, V. Stankevič, S. Keršulis, S. Tolvaišienė, M. Skapas, M. Vagner, V. Plaušinaitienė, N. Žurauskienė, Accelerated ageing of $La_{1-x}Sr_xMn_yO_3$ thin films for high-field CMR sensor applications, Euro-Asian Pulsed Power Conference EAPPC/BEAMS/EML-2026, Nagaoka, Japan, September 13-17, 2026.

1. REVIEW OF PHYSICAL PROPERTIES OF LANTHANUM MANGANITES AND GRAPHENE

This chapter reviews physical properties of lanthanum perovskites, particularly manganese-based compounds (manganites). Magnetoresistance phenomena were presented. Significant consideration was given to colossal magnetoresistance and its application. Magnetism of graphene was introduced in this chapter. This Chapter concludes by the formulation of the main objective and tasks of the investigation.

1.1 Crystallographic structure

Manganite oxides, which possess a perovskite structure, are represented by the chemical formula $RE_{1-x}A_xMnO_3$ (where RE is a rare earth element and A is typically an alkaline element) [14, 15]. While most manganites exhibit a nearly cubic, perovskite-like crystal lattice (Figure 1.1.1), doping with lighter ions such as Strontium (Sr) or Calcium (Ca) introduces rhomboidal or orthorhombic lattice distortions. These distortions arise from either the tilting or stretching (Jahn-Teller effect) of the oxygen octahedra surrounding the Manganese (Mn) ions. Ultimately, this structural flexibility allows the material to accommodate ionic size mismatches and electronically induced deformations through various types of distortions, leading to larger unit cells with reduced symmetry [16]

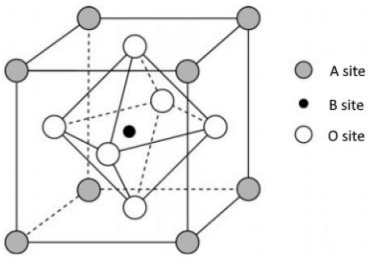


Figure 1.1.1 Ideal cubic perovskite structure. A site is occupied by La, Sr, Ca, while small B cation is a host for Mn. Oxygen takes positions at O sites. Adopted from [16].

Stability of the structure is determined by tolerance factor *t*,

$$t = \frac{rA+rO}{\sqrt{2}(rB+rO)}, \quad (1.1.1)$$

where *rA*, *rB*, *rO* represent radius of ions at A, B and O sites, respectively. The perovskite structure is stable for $0.89 < t < 1.02$, $t = 1$ corresponding to the perfect cubic structure [16].

Large RE trivalent ions (such as La) and A divalent ions (like Sr and Ca) occupy the A-site, featuring a 12-fold coordination with oxygen. In contrast, the smaller Mn ions, which exist in a mixed-valence state of Mn^{3+} and Mn^{4+}, are situated at the center of an oxygen octahedron at the B-site, where they have a 6-fold coordination.

1.2 Electronic structure

The magnetic and electrical properties of manganites are influenced by the arrangement of the valence electrons in the 3d shell of the Mn ions (see Figure 1.2.1). An isolated Mn ion has five degenerate orbital states for its 3d electrons. However, in a basic MnO_6 crystal, this degeneracy is partially lifted; the five d orbitals split into three t_{2g} orbitals and two e_g orbitals due to the cubic crystal field. In the compound $R_{1-x}A_xMnO_3$, the extreme cases of $x = 0$ and $x = 1$ ideally contain only Mn^{3+} and Mn^{4+}, respectively. In the intermediate range ($0 < x < 1$), both Mn^{3+} and Mn^{4+} coexist. The electronic configuration of the Mn^{3+} ion in a crystal field is $t_{2g}^3 e_g^1$, with the degeneration lifted due to the axial elongation of the oxygen octahedron resulting from Jahn-Teller distortion. In contrast, Mn^{4+} does not exhibit a tendency to distort its octahedral environment, leading to a complete occupation of the t_{2g} levels. Due to significant Hund's energy, the electrons occupy all levels with the same spin state. Generally, t_{2g} electrons are highly localized, while e_g electrons are weaker localized, playing a key role in determining the compound's electrical conductivity [17, 18].

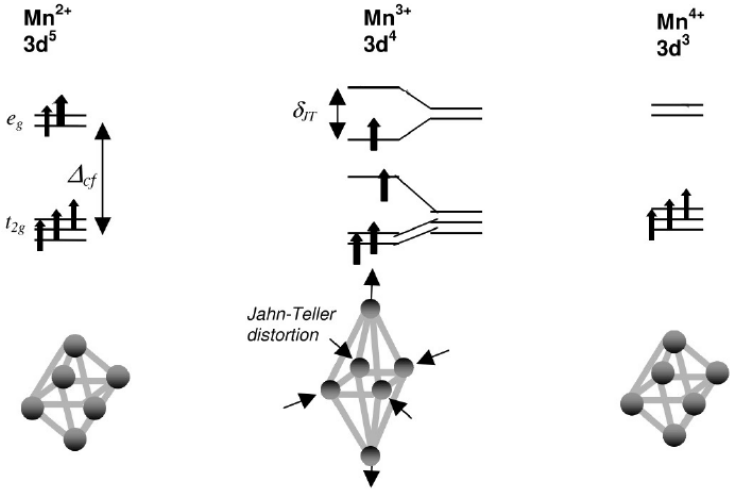


Figure 1.2.1 Single ion scheme of 3d electron states in Mn^{2+}, Mn^{3+} and Mn^{4+} ions in perovskite manganites. Adopted from [15].

1.3 Electrical conductivity

1.3.1 Double exchange model

The electrical transport in manganites is explained by the double exchange (DE) model, initially proposed by Zener [17, 18, 19]. This theory posits that electrons concurrently transfer from the e_g level of an Mn^{3+} ion, through an O^{2-} ion, to the vacant e_g level of a neighbouring Mn^{4+} ion. Under conditions of strong DE, particularly when doping concentration (x) is approximately 1/3, the e_g electrons become delocalized within the ferromagnetic phase.

Due to the interatomic Hund's rule, spin-up and spin-down bands are separated by 1 eV or more [16, 20] (Figure 1.3.1), with the upper band remaining empty. This leads to a half-metallic state where the conduction band is entirely spin-polarized, meaning charge carriers retain their spin orientation as they hop between adjacent Mn^{3+} and Mn^{4+} ions. The likelihood of this transport mechanism is contingent upon the angle (θ) between the magnetic moments of neighbouring Mn ions [19]:

$$P \propto cos\left(\frac{\theta}{2}\right). \tag{1.3.1}$$

Although the DE model offers a qualitative explanation for the change in resistivity during the ferromagnetic (FM) to paramagnetic (PM) phase transition, a precise quantitative description necessitates the inclusion of electron-lattice coupling. De Gennes showed that for low doping levels (small x), local distortions within the antiferromagnetic structure can trap

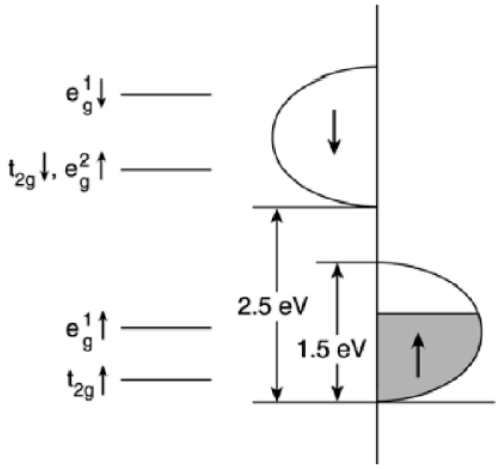


Figure 1.3.1 Schematic view of the band structure of $La_{2/3}Sr_{1/3}MnO_3$. Adapted from [16]

charge carriers [21]. This localization enhances their interaction with the surrounding magnetic field, consequently increasing the effective mass of the hopping electrons. Moreover, charge hopping is also affected by lattice distortions, as described by the Jahn-Teller effect. This intertwined carrier transport, influenced by both lattice and spin distortions, is commonly referred to as magnetic polarons. Some research indicates the presence of charge localization and the formation of small (unit-cell-sized) polarons in perovskite manganites above their Curie temperature (T_C) [22-26].

1.3.2 Metal-insulator transition

Manganite compounds with strong double exchange, such as $La_{1-x}Sr_xMnO_3$ or $La_{1-x}Ca_xMnO_3$ (with $x \approx 0.3$), exhibit transition from a high-temperature paramagnetic semiconducting or insulating state to a low-temperature, highly conductive ferromagnetic phase.

In the PM phase, electrical resistivity exhibits significant temperature dependence. Experimental data is commonly fitted by either a semiconducting behavior, described by $\ln(\rho/\rho_\infty) = E_a/kT$ (suggesting a pseudo-gap at the Fermi level [26, 27]), or the Variable Range Hopping (VRH) model:

$$\ln(\rho/\rho_\infty) = (T_0/T)^{1/4}, \qquad (1.3.2)$$

which is attributed to charge carrier localization due to magnetic disorder [28, 29].

At lower temperatures, below the Curie temperature, the spontaneous alignment of Mn spins leads to the delocalization of e_g electrons. This results in a low-resistivity FM phase, typically characterized by a $\rho \approx \rho_0 + aT^2$ dependence for $T << T_C$. An external magnetic field can either induce this Mn spin alignment above T_C or enhance it below T_C. This effect is most pronounced near T_C, where the initial magnetic susceptibility diverges [30, 31].

1.4 Colossal magnetoresistance of manganites

1.4.1 Magnetoresistance of high quality (crystals or epitaxial films) manganites

The observation of the so-called colossal magnetoresistance (CMR) effect in the 1990s in high-quality epitaxial films of doped manganites renewed interest in these materials [17,18]. It was found that the CMR at room temperatures can be much larger (~60% at 5 T, normalizing the resistivity change to the zero-field value) in comparison with multilayer structures of

ferromagnetic/nonmagnetic materials [32], which were proposed for use in magnetic recording. The magnetoresistance (*MR*) for manganites is negative, because the resistivity decreases with applied magnetic field and is usually defined as follows:

$$MR(B) = 100\% \times \frac{R(B)-R(0)}{R(0)}, \qquad (1.4.1)$$

where $R(B)$ and $R(0)$ are electrical resistance values in magnetic field and without it, respectively.

Urushibara et al. [33] investigated $La_{1-x}Sr_xMnO_3$ single crystals over a broad composition range ($0 \le x \le 0.6$). Figure 1.4.1 reproduces their original resistivity-versus-temperature data. For $x \le 0.05$ no ferromagnetic transition is evident, whereas higher Sr concentrations produce a pronounced resistivity

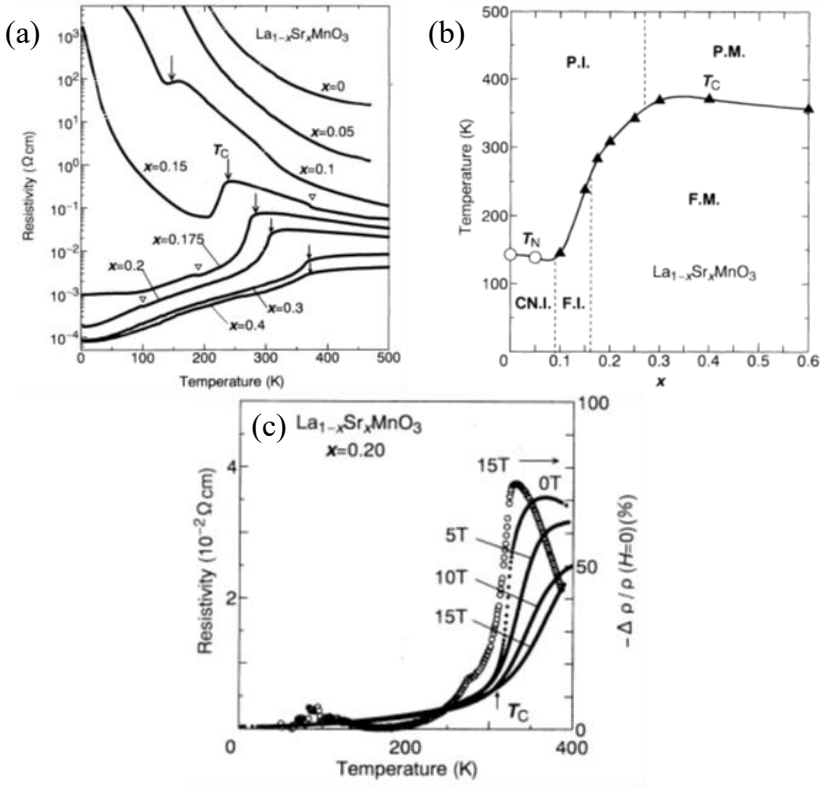


Figure 1.4.1 Main characteristics for $La_{0.8}Sr_{0.2}MnO_3$ crystals: (a) resistivity vs. temperature dependences. Arrows indicate the critical temperature for the paramagnetic-ferromagnetic phase transition. Open triangles indicate structural transition; (b) electronic phase diagram. Open circles and filled triangles indicate the Neel (T_N) and Curie (T_C) temperatures, respectively. The meaning of abbreviations: paramagnetic insulator (PI), paramagnetic metal (PM), spin-canted insulator (CNI), ferromagnetic insulator (FI), and ferromagnetic metal (FM); and (c) resistivity vs. temperature dependence for chemical composition $x = 0.20$ under various magnetic fields [32]. Adapted from Urushibara et al. [33].

anomaly close to the Curie temperature. The coincidence of magnetic ordering and the metal-insulator transition is one of the characteristic features of this system.

The colossal magnetoresistance effect in manganites can be qualitatively explained by a double-exchange mechanism between manganese ions Mn^{4+} and Mn^{3+}, as an applied magnetic field aligns their spins and, therefore, this leads to a decrease in resistivity. However, the double exchange model alone is not sufficient to explain the CMR effect, and in addition a strong electron-phonon interaction arising from the Jahn-Teller effect must be considered [34].

As the mixed-valence manganite perovskites exhibit very rich variety of crystallographic, electronic, and magnetic phases, numerous investigations of the CMR effect in a variety of chemical compositions were performed. One can find more information in a comprehensive review by Coey [14] followed by other reviews with different aspects on preparation methods, chemical composition, structure and microstructure, material properties and various areas of applications [35-43]. It is worth mentioning the difference between the intrinsic and extrinsic properties of the manganites. Whereas intrinsic effects are found in bulk single crystals or high-quality epitaxial films and are determined by material parameters, the extrinsic effects are only found in polycrystalline materials with defected structures having grain boundaries and artificial heterostructures [38]. Moreover, the high-quality crystals or epitaxial films exhibit the highest *MR* values only close to T_C, which is a drawback for applications. Therefore, much attention was paid to polycrystalline or nanostructured films exhibiting so-called extrinsic magnetotransport phenomena [43]. The *MR* of such films is significant in a wide range of temperatures starting from $T_{M\text{-}I}$ down to cryogenic temperatures (see Figure 1.4.2) [43].

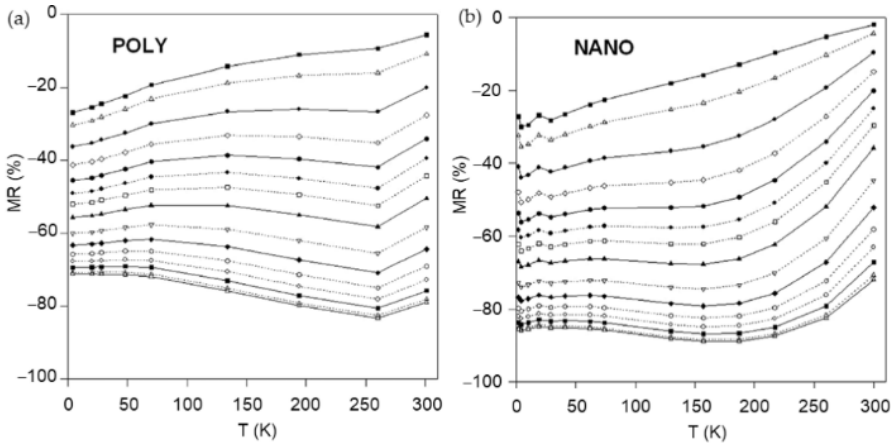


Figure 1.4.2 Temperature dependences of magnetoresistance for poly- (a); and nanocrystalline (b) manganites $La_{0.8}Sr_{0.2}MnO_3$ upon applied different magnetic fields: 1, 2, 4, 6, 8, 10, 12, 15, 20, 25, 30, 35, 40, 45, and 47 T (from top to bottom) [43].

1.4.2 Magnetoresistance of polycrystalline manganites

Most of the studies performed so far considered two main magnetic field ranges and related effects induced by a disorder in ferromagnetic perovskites: a low-field magnetoresistance (LFMR) and a high-field magnetoresistance (HFMR) [44-46].

Hwang et al. [44] directly compared a $La_{2/3}Sr_{1/3}MnO_3$ single crystal with two polycrystalline samples. In Figure 1.4.3a, the single crystal shows no sharp low-field resistance drop. By contrast, the ceramic samples in Figure 1.4.3c, e exhibit an abrupt decrease at low fields, although their magnetization curves (Figure 1.4.3d, f) remain similar to that of the single crystal. The additional resistance change is therefore attributed to spin-polarized tunnelling across grain boundaries.

At higher fields, the resistivity of polycrystalline manganites continues to decrease with a smaller, nearly linear slope. This high-field contribution is associated with disordered grain-boundary material having reduced magnetization and Curie temperature [46] and with thermally assisted hopping through an energy barrier, as described by modified Mott variable-range-hopping models [47, 48]. In a separate pulsed-field study, a 400 nm $La_{0.83}Sr_{0.17}MnO_3$ film retained a non-saturating response up to 91.4 T at 77 K and up to 60 T at room temperature [10]. The reported sensor response at 91 T was approximately 2 mV/T.

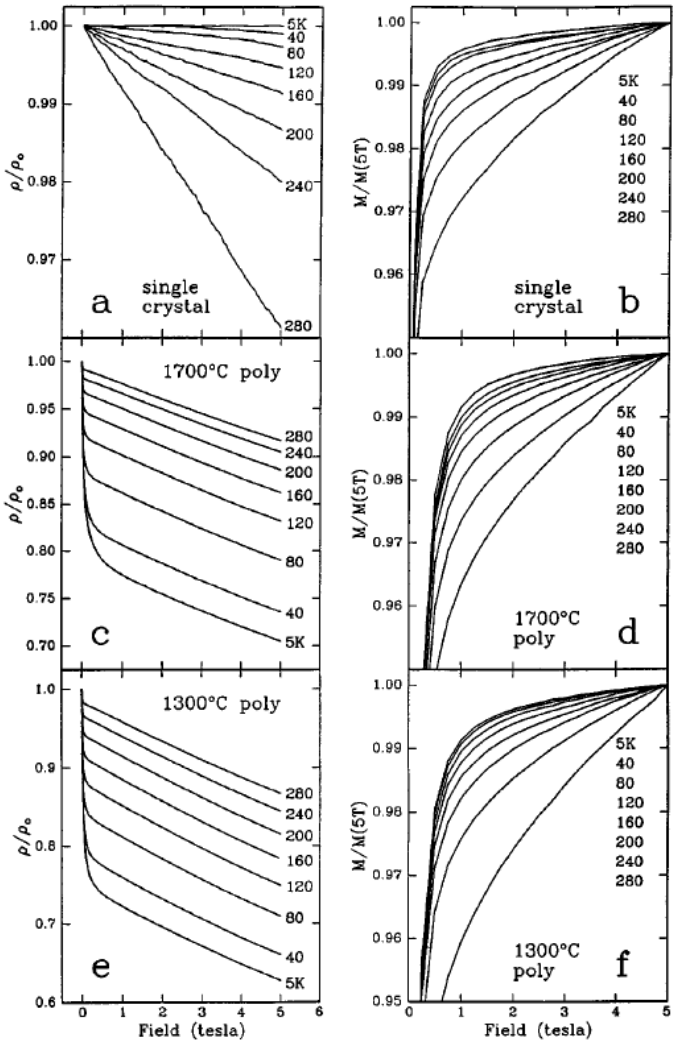


Figure 1.4.3 Magnetic-field dependences of normalized resistance (a,c,e) and magnetization (b,d,f) for a $La_{2/3}Sr_{1/3}MnO_3$ single crystal and ceramic samples sintered at 1700 °C and 1300 °C at temperatures from 5 to 280 K. Adapted from Hwang et al. [44].

1.4.2.1 Low-field magnetoresistance

The observation of the low-field magnetoresistance at low temperatures is one of the main features of polycrystalline manganites. In comparison with Giant magnetoresistance multilayered structures, the LFMR effect can extend the sensing magnetic field region up to hundreds of millitesla, what is an advantage for low-field magnetic sensors applications. Considering magnetic sensors for high-field measurements, the LFMR is important for pulsed field

sensing, when not only amplitude, but also the whole pulse shape must be recorded. Lee et al. [46] predicted that the upper limit of conductivity change due to the LFMR effect could be up to 33.3% not depending on chemical composition. Therefore, during the last decades the major focus of scientific investigations has been on increasing the LFMR by introducing various artificial grain boundaries in thin-film structures to ensure a thin-energy barrier for spin-polarized tunnelling [49, 50]. In some cases, an insulating thin layer was used (for example, $SrTiO_3$ multijunction La- Sr- Mn- O/$SrTiO_3$/La- Sr-Mn-O), or composite manganite films were grown with a second insulating oxide phase of ZnO, NiO or CeO_2. It was demonstrated, that for layered structure of LSMO/$SrTiO_3$/LSMO the LFMR = 50% could be found at 4.2 K in magnetic field of 20 mT [51].

Although LFMR is generally strongest at low temperatures, nanostructuring can enhance it sufficiently for sensor-oriented studies. Sadhu and Bhattacharyya [50] reported $La_{0.71}Sr_{0.29}MnO_3$ nanoparticles with an LFMR of 29.8% at 50 mT and 30 K. Their original field- and temperature-dependent data are shown in Figure 1.4.4. The result was attributed to spin-polarized tunnelling across the natural grain boundaries of approximately 20 nm particles.

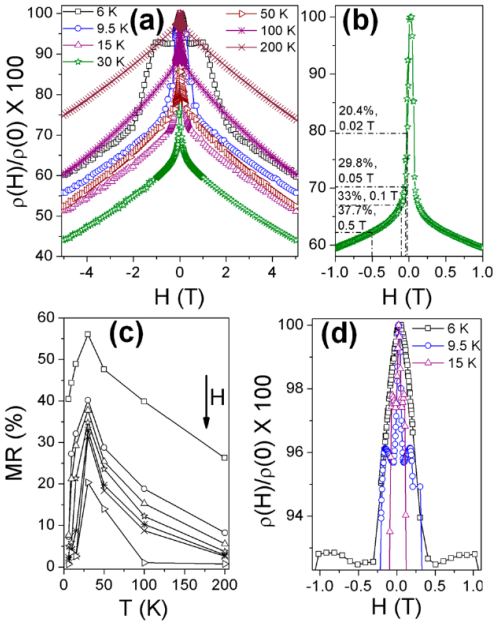


Figure 1.4.4 Magnetoresistance of $La_{0.71}Sr_{0.29}MnO_3$ nanoparticles: (a) normalized resistance at different temperatures; (b) low-field magnetoresistance at 30 K; (c) temperature dependence of MR at decreasing applied fields; and (d) enlarged low-field region at 6, 9.5 and 15 K. Adapted from Sadhu and Bhattacharyya [50].

A separate thin-film study [52] showed that polycrystalline $La_{0.8}Sr_{0.2}Mn_{1.21}O_3$ grown on quartz reached an LFMR of 31% at 0.7 T and 25 K, approximately twice the values obtained on polycrystalline Al_2O_3 or SiO_2 substrates. This comparison demonstrates that the substrate and the resulting grain-boundary network can substantially modify the low-field response.

For nanostructured $La_{1-x}Sr_xMn_yO_3$ films with Mn excess ($y > 1$), adjustment of composition and growth conditions produced magnetoresistance values of −1.23% to −0.8% at 50 mT in the temperature range 250−290 K [52].

1.4.2.2 High-field magnetoresistance

High-field magnetoresistance depends strongly on crystallite size. Balcells et al. [53] found that reducing the mean grain diameter of $La_{2/3}Sr_{1/3}MnO_3$ ceramics from micrometre to nanometre scale increased the *MR* at 5.5 T. Pękała et al. [43] subsequently compared polycrystalline and nanocrystalline $La_{0.8}Sr_{0.2}MnO_3$ over fields up to 47 T. Their original isothermal *MR* curves are reproduced in Figure 1.4.5. The response remained non-saturating, and the nanocrystalline material generally reached the larger high-field *MR* magnitude. The authors reported high-field sensitivities of approximately 0.2–0.4%/T for the polycrystalline sample and 0.2–0.6%/T for the nanocrystalline sample at 47 T.

The lack of complete *MR* saturation in nano- and polycrystalline manganites is commonly related to the high fields required to align magnetic moments in structurally disordered grain boundaries. These regions may remain paramagnetic or antiferromagnetic over a broad temperature interval. Lee et al. [45] described the high-field magnetoconductance using contributions associated with the magnetized grains and grain-boundary susceptibility. At lower magnetization, several manganites show an approximately proportional relationship between *MR* and $-M^2$, whereas deviations at higher magnetization indicate an increasing contribution from the grain-boundary term.

The observed decrease in resistivity of polycrystalline films is dominated by the grain boundary (GB) effects [43, 54-55]. The lack of saturation measured up to 50–60 T was explained by various models. It could be attributed to strong antiferromagnetic coupling of spins in the GBs. The high-field magnetization has been studied in $Sm_{0.5}Ca_{0.5}MnO_3$ manganites and almost constant increase up to high magnetic fields up to 100 T was found [56]. These films exhibited metamagnetic transitions, which were

attributed to the field-induced collapse of the charge-ordered state. It should be noted that such antiferromagnetic manganites cannot be used for very high magnetic field sensors, because the metamagnetic transitions is a drawback for calibration of such sensors.

A single linear conductance law does not describe all polycrystalline manganites. Gangineni et al. [57] found that a quadratic polynomial, $G(H) = a + bH + cH^2$, represented conductance up to 47 T for several bulk and thin-film compositions. Wagner et al. [48,49] instead incorporated the field-dependent hopping barrier into a modified Mott model and showed that the resistivity decrease of epitaxial $Nd_{0.52}Sr_{0.48}MnO_3$ scales with the Brillouin function in the ferromagnetic state and with its square in the paramagnetic state.

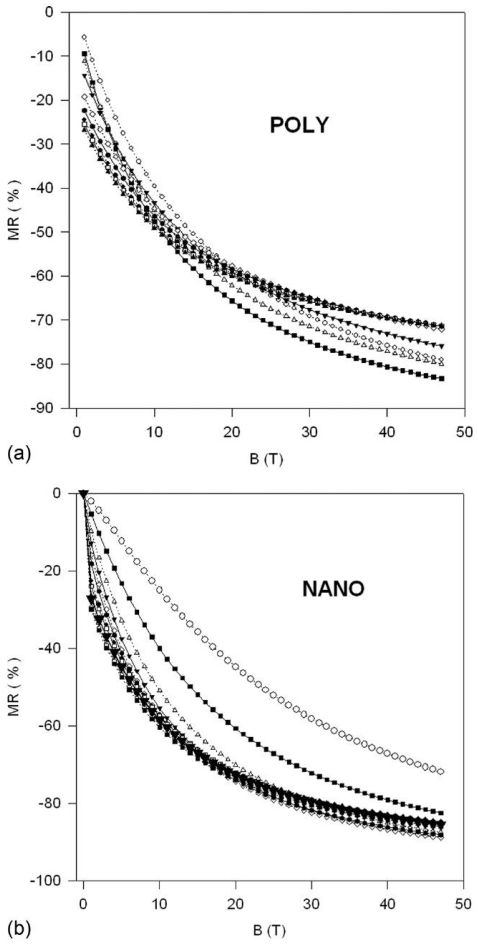


Figure 1.4.5 Magnetic-field dependence of magnetoresistance for polycrystalline (a) and nanocrystalline (b) $La_{0.8}Sr_{0.2}MnO_3$ at multiple temperatures up to 47 T. Adapted from Pękała et al. [43].

The authors obtained high value of spin moment $J = 60$ using the scaling the MR dependences by Brillouin function in the vicinity of the phase transition and attributed it to the presence of large magnetic clusters due to the short-range ferromagnetic ordering. Considering nanostructured films (polycrystalline with nano-size crystallites) having wide (7–10 nm) mesoscopic regions of grain boundaries, Balevicius et al. proposed to use a simple approach, where both crystallites and grain boundaries are connected in series [10]. In such case the magnetoresistance was analysed by the sum of the two contributions:

$$MR = f \times A_C \times Ɓ(x) + (1 - f) \times A_{GB} \times Ɓ(x_{GB}) + LFMR\ for\ FM \quad (1.4.2)$$

$$MR = f \times A_C \times Ɓ^2(x) + (1 - f) \times A_{GB} \times Ɓ^2(x_{GB}) + LFMR\ for\ PM \quad (1.4.3)$$

where f is the crystallite-material fraction, $(1 - f)$ is the grain boundary fraction, $Ɓ(x)$ is the Brillouin function, $x_{C(GB)} = g\mu_B J_{C(GB)} B/k_B T$. The spin-orbit quantum numbers of the crystallites (J_C) and grain boundaries (J_{GB}), and the magnetoresistance amplitudes (A_C) as well as (A_{GB}), respectively, are used as parameters. Low-field magnetoresistance (LFMR) in this study was obtained from the low-field measurements performed in magnetic fields aligned parallel to the film plane.

The two-component crystallite/grain-boundary model was applied separately to La-Ca-Mn-O films measured in ferromagnetic and paramagnetic states [58]. The fitted parameters indicated distinct magnetic responses of the crystallites and grain-boundary material, consistent with magnetically aligned polarons in wider disordered regions. More broadly, magnetoresistance can be tuned through substrate selection, growth conditions, film thickness, chemical composition and substitution at the A and B sites of the perovskite lattice.

Žurauskienė et al. [59] examined nanostructured La-Sr-Mn-O films grown by pulsed-injection MOCVD on glass-ceramics. Figure 1.4.6 reproduces their original comparison of resistivity and high-field *MR* as functions of temperature for films of different thicknesses and for films deposited at different temperatures. The largest *MR* occurs near the metal-insulator transition, while changes in film microstructure shift the transition and alter both resistivity and *MR*. Separate studies showed related effects of MOCVD pressure in La-Ca-Mn-O films [60], substrate-dependent low- and high-field *MR* [52], and Co substitution at the Mn site [61, 62]. Grain-size reduction does not always increase disorder-driven *MR*; under some conditions it can suppress variable-range hopping and promote ferromagnetism.

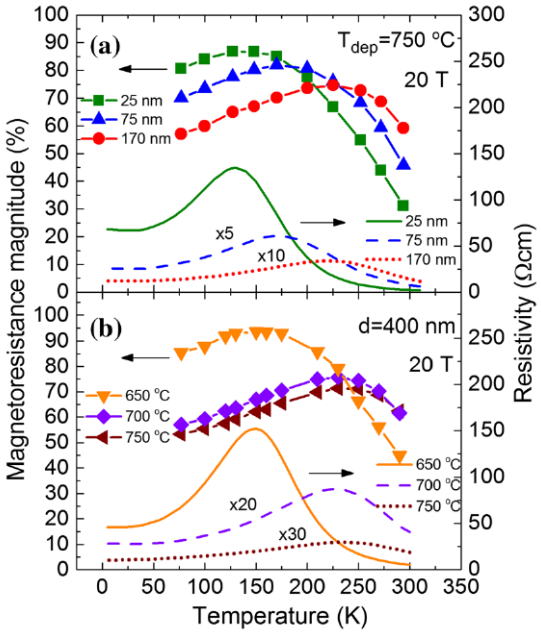


Figure 1.4.6 Resistivity (right scale) and magnetoresistance magnitude at 20 T (left scale) as functions of temperature for nanostructured La-Sr-Mn-O films with different thicknesses (a) and different deposition temperatures (b). Adapted from Žurauskienė et al. [59].

Zurauskiene in a review [4] summarized the results presented in literature on magnetoresistance magnitudes measured at high magnetic fields at low and high temperatures. Table 1.1 adopted from [4] presents typical magnetoresistance values for La-Sr-Mn(Co)-O and La-Ca-Mn-O films. Table 1.1 also presents some typical results reported on different chemical compositions such as $La_{0.67}Ba_{0.33}MnO_3$ [63], $La_{0.4}Gd_{0.1}Ca_{0.5}MnO_3$ [64], $La_{0.45}Ho_{0.05}Ca_{0.5}MnO_3$ [65], $La_{0.45}Ca_{0.55}MnO_3$ [66] and $La_{0.5}Ca_{0.4}Li_{0.1}MnO_3$ [67] materials.

Table 1.1 Overview of high magnetoresistance magnitudes in polycrystalline manganites measured at low and close to room temperatures in high magnetic fields. The MR at intermediate temperature corresponding to the highest MR value is marked by *. Adopted from [4].

Composition	Preparation Peculiarities	Temperature, K	Magnetic Field, T	MR Magnitude, %	Ref.
$La_{0.7}Ca_{0.3}MnO_3$	Nano-crystalline	4-150	15-47	80-98	[55]
		* 150	47	~98	
		302	47	~68	
	Micro-crystalline	4.2	47	~80	
		* 250	47	~92	
		300	47	~85	
$La_{0.59}Ca_{0.41}MnO_3$	Film; Substrate: lucalox (glass ceramics)	77	60	~95	[58]
		294	60	~80	
$La_{0.72}Ca_{0.28}Mn_{0.98}O_3$	Film; Substrate: lucalox; gas pressure in growth chamber 3 Torr	1.3	60	85	[60]
		* 225	60	98	
		290	60	85	
	Film; Substrate: lucalox; gas pressure in growth chamber 7 Torr	1.3	60	75	
		* 225	60	92	
		290	60	80	
$La_{2/3}Sr_{1/3}MnO_3$	Ceramics, average size 25 nm	10	5.5	50	[53]
$La_{0.8}Sr_{0.2}MnO_3$	Nano-crystalline	4	47	85	[43]
		* 157	47	89	
		300	47	70	
	Micro-crystalline	4.2	47	71	
		* 260	47	83	
		300	47	78	
$La_{0.83}Sr_{0.17}MnO_3$	Film; Substrate: glass ceramics; film thickness 25 nm	77	20	81	[59]
		* 130	20	87	
		294	20	31	
	Film; Substrate: glass ceramics; film thickness 400 nm	77	20	53	
		* 230	20	71	
		294	20	62	
$La_{0.83}Sr_{0.17}MnO_3$	Film; Substrate: lucalox (glass ceramics); film	77	91.4	78	[10]
		290	58	85	

	thickness 400 nm				
$La_{0.82}Sr_{0.18}Mn_{1.15}O_3$	Film; Substrate: polycrystalline Al_2O_3; film thickness 360 nm; Mn excess 1.21	77	20	56	[52]
		* 250	20	66	
		363	20	38	
$La_{0.79}Sr_{0.21}Mn_{1.05}Co_{0.12}O_3$	Film; Substrate: polycrystalline Al_2O_3; Co/(La + Sr) = 0.12	4	60	82	[62]
		* 220	60	83	
$La_{0.67}Ba_{0.33}MnO_3$	ceramics	4.2	8	50	[63]
		294	8	29	
$La_{0.4}Gd_{0.1}Ca_{0.5}MnO_3$		5	10	60-85	[64]
		125	10	98	
$La_{0.45}Ho_{0.05}Ca_{0.5}MnO_3$		130	8	18	[65]
$La_{0.45}Ca_{0.55}MnO_3$	Nanoparticles; average size 70 nm	80	7	99	[66]
$La_{0.5}Ca_{0.4}Li_{0.1}MnO_3$	Grain size 5-10 μm	5	14	82	[67]
		300	14	30	

1.5 Sensors based on colossal magnetoresistance effect

As it was mentioned in the Introduction, the sensors based on AMR, GMR or TMR effects are widely used in industry, however, are limited in high magnetic field sensing range and cannot be used to measure moderate or high-amplitude fields. The requirements for magnetic-field sensors vary depending on the specific application and may include the operating magnetic-field and temperature ranges, sensitivity, measurement accuracy, dependence on the field direction, operating frequency, and other parameters. In high-field measurements, however, detectivity is typically of less critical importance than the ability to accurately measure large magnetic-field amplitudes.

High-field magnetic sensors based on polycrystalline manganites can retain a useful, nearly isotropic response at fields where many AMR, GMR and TMR devices saturate. Xu et al. [63] measured the field sensitivity of La-Sr-Mn-O and La-Ba-Mn-O sensors for three field orientations. Their original sensitivity data are reproduced in Figure 1.5.1. At fields above approximately 3 T, the orientation-dependent curves converge toward a sensitivity magnitude of about 5%/T.

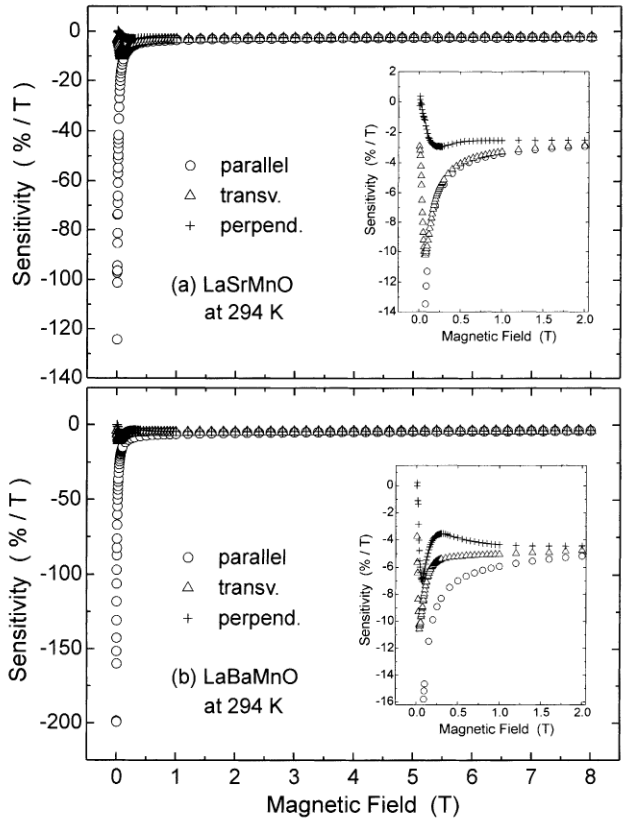


Figure 1.5.1 Field sensitivity at 294 K for (a) $La_{0.67}Sr_{0.33}MnO_3$ and (b) $La_{0.67}Ba_{0.33}MnO_3$ sensors with the magnetic field applied parallel, transverse and perpendicular to the sensor. Insets show the low-field region. Adapted from Xu et al. [63].

One can see that at room temperature the maximal sensitivity of ~200%/T is achieved for La-Ba-Mn-O films in the range of 1–3 mT. At a high magnetic field the absolute value of S_{MR} is decreased to 5%/T. It was concluded that nearly isotropic behaviour is very promising for sensors applications in high magnetic fields. From this point of view, the CMR sensors are preferable for some applications in comparison with Hall sensors which sense only one component of the field, especially when the field direction is not known in advance and probing areas are very small (impossible to use three sensors installed in different directions).

Stankevič et al. [11] developed the four-channel pulsed-field measurement system shown in Figure 1.5.2. Four CMR-B-scalar sensors are connected to individual recording modules, and optical links transfer the stored waveforms to a computer. Calibration curves measured over temperature are used by the software to convert the recorded voltage into magnetic flux density. Further

modification of CMR magnetic sensor/meter system was realized as a hand-held CMR-B-scalar meter [68]. Arrays of CMR-B-scalar sensors have been used to measure magnetic-field distribution and diffusion in electromagnetic launchers, pulsed magnets and magnetic-forming systems [69-71].

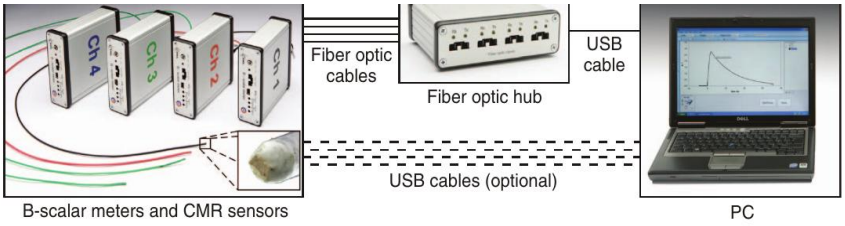


Figure 1.5.2 Outside view and schematic diagram of a four-channel pulsed magnetic-field measurement system based on CMR-B-scalar sensors. Adapted from Stankevič et al. [11].

1.6 Ageing behaviour of manganite films

For a manganite magnetic-field sensor, ageing is not the same as the reversible change in resistance caused by ambient temperature. In pulsed-field measurements, the zero-field resistance can be recorded immediately before the field pulse and used for temperature determination. This procedure does not correct a permanent drift of the resistance or a change in the magnetoresistance calibration. Long-term stability is, therefore, a separate sensor requirement [63,72-74].

The most plausible source of this drift in nanostructured La-Sr-Mn-O films is the oxygen-sensitive, disordered material at grain boundaries. Oxygen nonstoichiometry changes the Mn^{3+}/Mn^{4+} balance and the concentration of holes involved in double exchange. Weakly bound oxygen can be released from grain-boundary regions and diffuse towards the film surface; grain boundaries provide much faster diffusion paths than the crystalline bulk [75- 77]. Oxygen loss consequently increases resistivity and weakens magnetic coupling between neighbouring grains. Comparable time-dependent resistance changes have also been reported in cobalt-based perovskites [78], while metastability and oxygen-deficiency effects have been observed in LSMO and LCMO materials [76, 79-80]. These results support an oxygen-related explanation, although the relative contributions of diffusion, defect redistribution and structural relaxation depend on composition and microstructure.

The effect is expected to be pronounced in polycrystalline and nanostructured films because a substantial part of the current crosses

structurally and magnetically disordered grain boundaries. The crystallites may remain comparatively stable while the intergranular regions continue to evolve. Very thin epitaxial films can also exhibit resistance drift, so ageing should not be attributed to grain boundaries alone; nevertheless, the grain-boundary network provides a consistent explanation for the strong response of the films considered here [72-75].

Natural ageing is slow enough to require measurements over months or years. It can be accelerated by annealing above the intended operating temperature. In the study reported by Simkevicius et al. [73], uncovered LSMO films were annealed in argon at 50, 100, 150, 200 and 250 °C. Between 50 and 200 °C, the resistivity increased most rapidly during the first hours and then approached saturation. The sample treated at 250 °C behaved differently: after the first five hours, further annealing reduced its resistivity, and those data were excluded from the relaxation analysis considering the influence of oxygen diffusion from crystallites. This result shows that a higher temperature does not merely accelerate the same process. For the films annealed at 100 °C, eight hours of treatment was insufficient: the resistivity still changed by about 12% during the first year and by a further 3% during the second. After 24 hours at 100 °C, the drift over almost two years was approximately 1.5% [73].

A single Debye exponential does not reproduce the broad time dependence observed in these disordered materials. Ageing in manganite ceramics and films has instead been described with the Kohlrausch-Williams-Watts (KWW) stretched-exponential function. The general basis of this approach is discussed in studies of dispersive relaxation [81], while its application to manganite ceramics and films is reported in [82-84]. For a resistivity that increases towards a limiting value, the form used in these studies is the following:

$$(\rho_t-\rho_0)/\rho_0=[(\rho_\infty-\rho_0)/\rho_0]\{1-\exp[-(t/\tau)^k]\}, \quad (1.6.1)$$

where ρ_0 is the resistivity before ageing, ρ_t is the value after treatment time t, ρ_∞ is the limiting value, τ is the characteristic time and k is the stretching exponent. When $k = 1$, the expression reduces to a single exponential. Values below unity indicate a distribution of relaxation times rather than one uniform process [81,82].

The fitted value of k is useful, but it should not be treated as a unique fingerprint of the microscopic mechanism. Refs. [73, 74] associated k values of about 0.43-0.60 with dispersive transport and repeated trapping and release events, whereas values near 0.8-0.9 are more consistent with hierarchically limited relaxation, in which one local rearrangement depends on earlier events [73, 74, 81]. For the uncovered films [73], k decreased from 0.88 at

50 °C to 0.83, 0.74 and 0.66 at 100, 150 and 200 °C, respectively. A film annealed for 24 hours at 100 °C gave $k \approx 0.8$ [73]. The trend suggests a change in the balance of relaxation processes as the annealing temperature increases.

The high-temperature transport data were also examined using Mott's variable-range-hopping (VRH) model [28, 73]. This interpretation requires some caution. For the investigated films, the available 265–310 K interval was too narrow to distinguish decisively between VRH and small-polaron hopping. In addition, the localisation lengths obtained from the VRH fit were not compatible with the usual physical limits of the model. Simkevicius et al. [73] therefore used the fitted localisation parameter mainly to compare changes with annealing time and temperature. VRH is thus a plausible phenomenological description of the ageing data, not proof of a single transport mechanism.

Ageing changes the zero-field resistivity much more than the normalised magnetoresistance at moderate and high fields. During long-term tests, the change in magnetoresistance amplitude at 2 T remained below about 0.5%; in pulsed fields up to 20 T, it remained below 2%, even though the resistance changed markedly [73, 74]. The low-field response was not invariant. Annealing reduced the demagnetising field and the magnetoresistance anisotropy, especially when the field was perpendicular to the film plane [73]. Pre-ageing can therefore improve long-term stability without seriously degrading the high-field response, but the low-field and orientation-dependent calibration must still be checked.

A coating should not be treated as a passive barrier without qualification. In the experiments with a polyethylene-based hot-melt adhesive, coating altered the resistance during annealing and shortened the time required to approach a stable state; the accelerated process was reported to be almost three times faster. The observed resistance decrease may have involved oxygen exchange between the adhesive and the film, but this mechanism was not established conclusively [74]. The protective material and the thermal-treatment schedule must therefore be evaluated together.

For the present work, ageing is best treated as an oxygen-related defect-relaxation process concentrated mainly in the disordered regions of the film. Its practical indicators are the drift of resistivity at zero magnetic field, the KWW parameters τ and k, and any accompanying change in magnetoresistance or magnetoresistance anisotropy. Annealing in argon near 100 °C for approximately 24-28 hours is a reasonable starting condition for stabilisation, but it is not a universal prescription [73, 74]. Manganese nonstoichiometry, substrate-induced microstructure and encapsulation all change the initial defect state and may change the required treatment. This

provides the basis for examining how manganese content, substrate type and annealing time affect the stability of $La_{1-x}Sr_xMn_yO_3$ films.

1.7 Magnetism of graphene

1.7.1 Magnetoresistance of graphene

Future miniaturization of magnetic sensors leads to the search of advanced materials, in which magnetic field induced phenomena are significant when reducing dimensions to nanoscale. Although magnetic sensors based on three-dimensional bulk materials or thin films exhibit relatively high magnetoresistance and sensitivity to magnetic fields, the dimension reduction to nanoscales is sometimes a challenge for device fabrication. The engineering of advanced materials on the nano-microscales also leads to new phenomena and increased functional possibilities of such materials [35]. During the last decades the attention to two-dimensional (2D) materials, such as graphene, which is a 2D Dirac semimetal and exhibits very high mobility of charge carriers [7], has rapidly increased. Graphene demonstrates remarkable electronic, magnetic, mechanical, and thermal properties and can be used for a number of different applications [85-87]. For magnetic sensing and magnetoelectronics, the large positive magnetoresistance induced by the Lorentz force has attracted attention of many scientific groups [88-91].

In low magnetic fields ($B < 1$ T), the MR has classical quadratic dependence on B [7, 88-90] and normally must saturate to a relatively small magnitude. However, due to various inhomogeneities it can show non-saturating linear dependence in higher fields. The linear magnetoresistance (LMR) in high magnetic fields was reported in few-layer or multilayer graphene even at room and above temperatures [8, 88-94].

Kisslinger et al. [8] measured reproducible linear magnetoresistance in bilayer graphene up to 62 T. Figure 1.7.1 reproduces the experimental figure from that publication, comparing epitaxial bilayer graphene with quasi-free-standing bilayer graphene and showing the low-temperature quantum features superimposed on the high-field response.

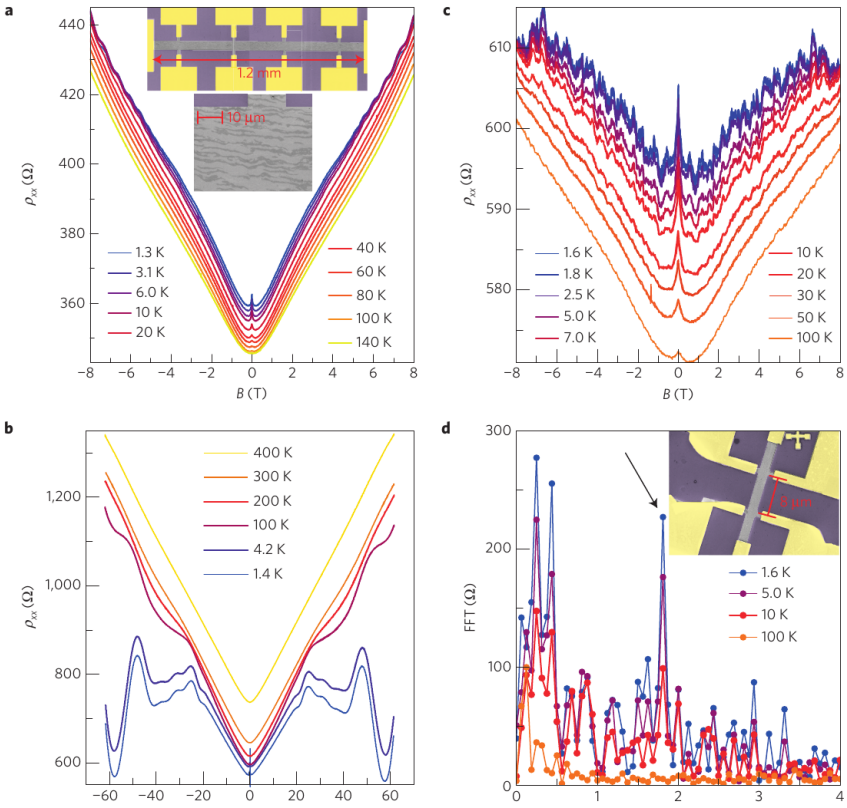


Figure 1.7.1 Experimental magnetoresistance data for epitaxial and quasi-free-standing bilayer graphene: (a, c) field dependences at different temperatures; (b) pulsed-field measurements up to 62 T; and (d) low-temperature quantum oscillations. Adapted from Kisslinger et al. [8].

Different theories were proposed to explain the LMR in graphene. Hu and Rosenbaum proposed that for a disordered conductor both classical [94-96] and quantum effects could compete and both models could explain the observed effects under certain conditions. The quantum origin of the LMR could be proven by observation of Shubnikov-de Haas oscillations and quantum Hall effect which are superimposed on the LMR dependence on the magnetic field and are more pronounced at low temperatures in high magnetic fields, when so-called "extreme quantum limit" is achieved. Friedman et al. [88] explained the observed results by quantum model.

In classical approach (Parish and Littlewood model) some defects or impurities could cause spatial charge inhomogeneities, which introduce mobility fluctuations and increase magnetoresistance values proportionally to the applied magnetic field. In the PL model the crossover magnetic field B_c, at which the transition from quadratic to LMR is observed, is proportional to

inverse Hall mobility μ and should increase with temperature. In addition, the slope $dMR(T)/dB \propto \mu(T)$.

It was shown that the LMR can be tuned by changing Hall mobility by various methods, for example, by adsorption or desorption of gas molecules in graphene by annealing it in helium atmosphere [97]. Usually at room temperatures in intermediate fields (~9 T) the magnetoresistance is observed in the range of 50–200% in single layer graphene prepared on SiO_2 [91] or SiC [90] substrates. Many attempts were made to increase the magnetoresistance values by decorating monolayer graphene surface with ferromagnetic transition metals adatoms (Co)[92], choosing special substrate (black phosphorus [91] or boron nitride [98]). Larger magnetoresistance could be more likely observed in few-layer stacked or multilayer graphene because of increased level of disorder and interlayer interactions.

In the latter case, when few-layer graphene structure is used, the two/multiband model [98] must be considered. According to it, when more than two conducting channels with different charge carrier mobility (μ) exist, the current at low magnetic field flows through the channel with higher mobility. When magnetic field is increased, the current will flow mostly through the channel with lower mobility, because the conductivity of the channels decreases as $1/[1 + (\mu B)^2]$. Gopinathan et al. [98] studied few-layer graphene/boron-nitride heterostructures and observed extremely large magnetoresistance, which was considered as local and nonlocal. The authors defined the local magnetoresistance as arising from differential carrier mobility across various layers of graphene upon a normal magnetic field. The non-local magnetoresistance was supposed to be due to the magnetic field induced Ettingshausen-Nernst effect [98].

Very high *MR* values (see Table 1.2) are promising for magnetic sensors applications. It was proposed to increase the *MR* by laminating single layer graphene (G) on a terraced substrate, such as TiO_2-terminated $SrTiO_3$ (STO). Hu et al. reported an *MR* of 5000% at 9 T and room temperature for graphene laminated on a terraced $SrTiO_3$ substrate [93].

Table 1.2 (adopted from [4]) presents some examples of magnetoresistance in intermediate and high magnetic fields observed in single, few-layer or multilayer graphene prepared on different substrates. One of the important parameters of 2D-material based magnetic sensors is magnetoresistance anisotropy. As the charge carriers are confined in the 2D film plane, the action of a Lorentz force when applying magnetic field perpendicular to the film plane results in the maximal magnetoresistance value.

Table 1.2 Some examples of magnetoresistance magnitude in single, few-layer and multi-layered graphene measured at low and room temperatures in high magnetic fields.

Number of Graphene Layers	Substrate; Preparation Peculiarities	Temperature, K	Magnetic Field, T	MR Magnitude, %	Ref.
1	SiO_2; exfoliation from Kish graphite	300	9	200	[91]
4	SiO_2, wet transfer	300	6	27	[92]
	SiO_2, wet transfer; surface decoration with Co particles			36	
4	SiO_2; mechanically peeling Kish graphite and transfer on SiO_2	400	9	330	[98]
1	SiC; growth by thermal sublimation of substrate; change of annealing time	300	9	40-80	[90]
	SiC; growth by thermal sublimation of substrate	2		100	
multilayer	Grown on SiC	300	9	80	[88]
		4.2	12	250	
2	SiC; hydrogen intercalation	300	62	90	[8]
1	Polycrystalline Al_2O_3; wet transfer	300	9	160	[13]
			20	450	
3			9	325	
			20	760	
1	Black phosphorus (BP); dry transfer	300	9	780	[91]
4	Boron nitride (BN); mechanical peeling of Kish graphite and transfer on BN	400	10	900	[98]
6				2000	
		2	12	6000	
1	$SrTiO_3$; laminating on terraced substrate	300	9	5000	[93]

In the case of in-plane magnetic field, it would be hard to change the trajectories of charge carriers by the action of Lorentz force in the direction of film thickness. An anisotropic magnetoresistance effect was reported in few-layer graphene stacks performing vertical transport measurements, when the angle θ between magnetic field and graphene plane was changed. Considering both quadratic and linear $MR(B)$ dependences, the experimental data of

resistance dependence on θ at B = 14 T were well fitted by considering the vertical component of the field $B_{\perp}\cos(\theta)$, where $B_{\perp}$ is magnetic field perpendicular to the graphene stack plane ($\theta = 0$). The carrier mobility values calculated from the fitting results were related to the carrier transport through the graphene stack corresponding to combined effects of both perpendicular and in-plane charge movement. It was found that the higher the mobility is, the larger the *MR* magnitude could be obtained. Liu et al. [99] have demonstrated that the AMR in graphene can be optimized by tuning sample shape, electrode distribution and gasses adsorptions. It was demonstrated that a two-fold symmetric AMR dependence on the angle between magnetic field and graphene plane observed at high temperatures could be changed into a one-fold dependence at low temperature for a graphene sample with an irregular shape. This "anomalous" AMR behaviour was explained by an anisotropic scattering of carriers from asymmetric edges and the boundaries of electrodes which could serve as active adsorption sites for gas molecules at low temperatures. The AMR effect observed in graphene could be used for the development of ultra-thin AMR devices.

1.7.2 Magnetic sensors based on graphene

Technological control of disorder in graphene creates opportunities for compact magnetic-field sensors. Pezeshki et al. [100] studied gated single-layer graphene devices with different densities of charged impurities. Figure 1.7.2 reproduces their original comparison of drain current and magnetoresistance as functions of gate voltage at 50 K and 300 K. The cleaner type-I devices reached the larger, gate-tunable response, while the more disordered type-II devices showed lower *MR*. The result demonstrates that gate voltage and extrinsic disorder must be considered together when optimizing graphene magnetosensors.

A different sensor concept combines the positive magnetoresistance of graphene with the negative magnetoresistance of a lanthanum manganite film [9]. The original device layout from that study is reproduced separately in Figure 1.7.3. The graphene and LSMO elements were formed on opposite sides of the same Al_2O_3 substrate and connected as a voltage divider. Because their resistances change in opposite directions under magnetic field, the combined output exceeded that of either element alone and remained non-saturating up to 20 T. The reported maximum normalized sensitivity was 72 mV/(V·T) in the 1–3 T range [9].

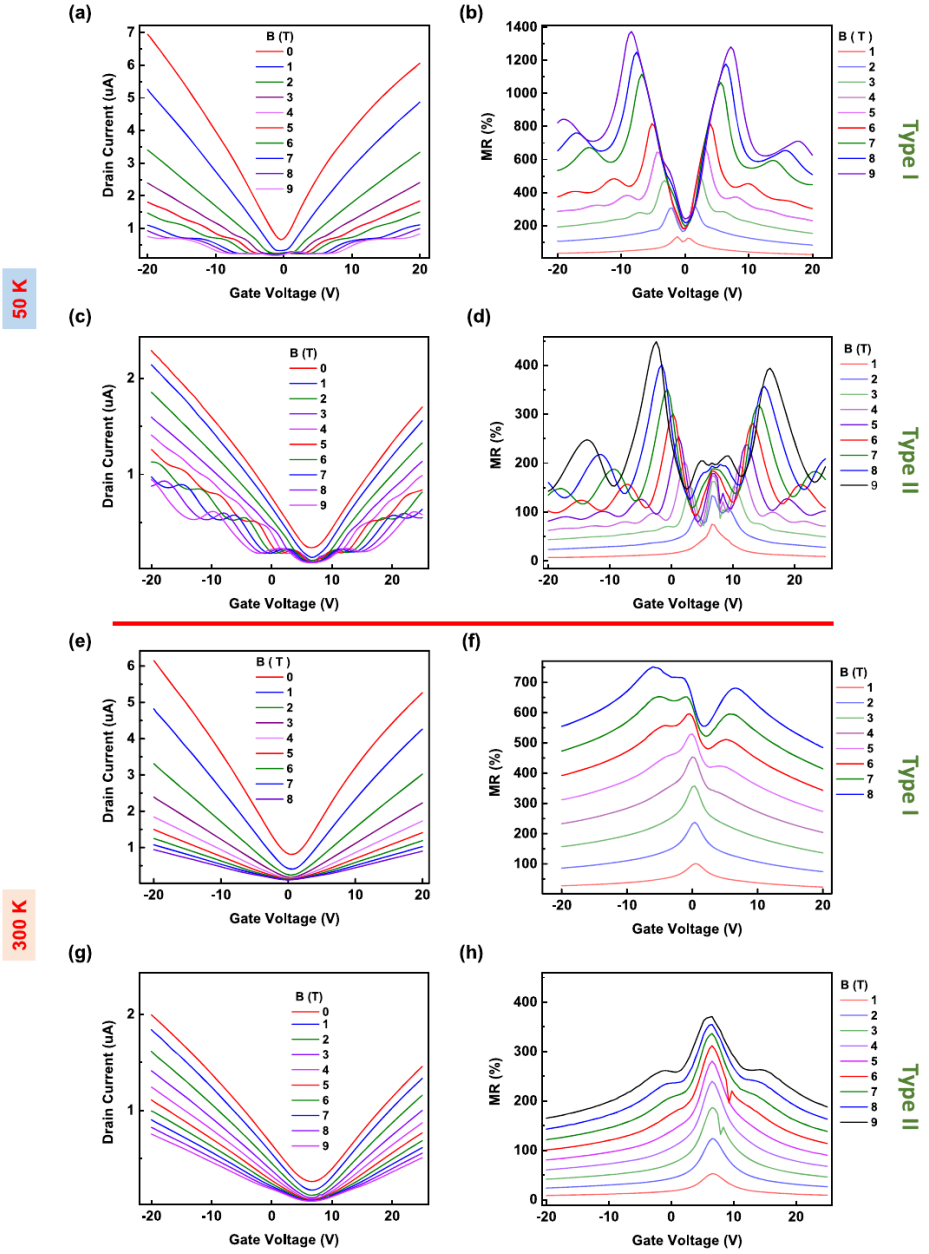


Figure 1.7.2 Drain current and magnetoresistance as functions of gate voltage for type-I and type-II single-layer graphene devices at 50 K (a-d) and 300 K (e-h) under magnetic fields up to 9 T. Adapted from Pezeshki et al. [100].

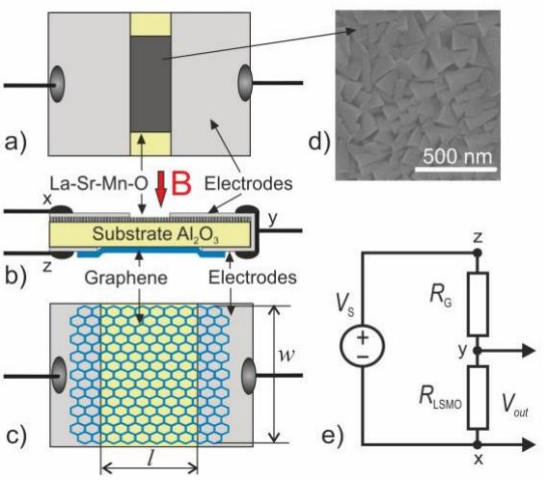


Figure 1.7.3 Original design of the manganite/graphene sensor: (a-c) layer and electrode arrangement, (d) SEM image of the LSMO film, and (e) voltage-divider circuit. Adapted from [9].

It has to be concluded, that despite various commercially available magnetic field sensors based on GMR, TMR and AMR effects, there is still a need of novel systems for the measurement of intermediate/high magnetic fields. Advanced magnetic field generation systems require sensors that are able to measure magnetic fields over a broad range of magnitudes and at different temperatures, while simultaneously determining the direction of these fields and tracking their changes. Therefore, the selection of materials with special properties and the design of effective sensor elements are very important. Many efforts were done to develop so-called CMR-sensors based on stoichiometric polycrystalline $La_{1-x}Sr_xMn_yO_3$ films. However, the optimization of their operation requires a comprehensive study on how chemical composition (x and y) influences their magnetoresistive properties and stability. Moreover, the need of local measurements of magnetic field and its direction encourages searching for advanced materials or their hybrid structures with 2D nanolayers exhibiting extended functionalities.

2. PREPARATION OF SAMPLES AND MEASUREMENT METHODOLOGY

2.1 Preparation of samples and their characterisation

This subchapter describes the fabrication methods of the samples used in this study and their characterisation techniques. The LSMO samples were prepared for the investigation of their individual properties as well as hybrid structures with graphene, while graphene single layers were investigated after transfer procedure on Al_2O_3.

2.1.1 Deposition of La-Sr-Mn-O films by using PI MOCVD

Lanthanum manganite $La_{1-x}Sr_xMn_yO_3$ (LSMO) films with different Sr (x) content and excess of Mn (y) were deposited onto a polycrystalline Al_2O_3 substrate by using a PI MOCVD technique. The temperature of the substrate was kept constant (750 °C) during the growth process. The thickness of the films was estimated by using a profilometer and it was found in the range of 350–360 nm. As precursors, toluene-dissolved $La(thd)_3$, $Sr(thd)_2$, and $Mn(thd)_3$ (thd is 2,2,6,6-tetramethyl-3,5-heptandionate) were prepared. A 2 Hz frequency was used to inject microdoses of approximately 3 mg of an organic solution with a mixture of dissolved precursors. The flash evaporation of the microdoses was performed at ~270 °C and the obtained vapor mixture was transported in the reaction chamber towards the heated substrate by a gas flow (~95 l/h) of argon and oxygen with ratio of 5:1, respectively. The growth rate of all investigated films was approximately 28 nm/min. Different groups of the films with different Mn excess y = Mn/(La + Sr) were prepared: the composition of precursors' solution was chosen to obtain the films with constant content of Mn (y = 1.05, 1.10, 1.15 and 1.20) while changing the composition of Sr (x = 0.05–0.3). To obtain a pure perovskite phase of the films, the deposition conditions were at first optimized by growing the films on monocrystalline $LaAlO_3$ (LAO) substrates, and only after that the films were deposited on polycrystalline Al_2O_3 substrates. Moreover, both substrates (Al_2O_3 and LAO) were used during final growth of LSMO films with various compositions for further comparison of their properties. After the deposition of the films, the annealing at the same temperature (750 °C) for 10 min in a pure oxygen atmosphere was performed and then the films were slowly (with ~4.7 °C/min rate) cooled down to 350 °C. The samples were prepared by planar photolithography. For electrode formation, a Cr sublayer with Ag

contact pads were thermally deposited. After that, the post-annealing was performed at 450 °C for 1 h in Ar atmosphere.

As seen in Table 2.1, the samples are grouped in few sets depending on growing conditions and measurements purposes. Films of Set 1 were grown with constant Mn excess while changing Sr content. On the other hand, films of Set 2 were grown with constant Sr content while changing amount of Mn. Chemical composition of films of Set 3 was chosen to increase temperature of operation of hybrid manganite-graphene sensor up to 90 °C. Substrate temperature for all sets was the same.

Table 2.1 Main characteristics of polycrystalline LSMO samples.

	T_{dep}, °C	T_m, K	ρ_m, Ωcm	Sr/(La+Sr)	Mn/(La+Sr)
Set 1	750	260	0.58	0.08	1.15
	750	270	0.27	0.18	1.15
	750	255	0.09	0.3	1.15
Set 2	750	240	0.47	0.18	1.05
	750	255	0.37	0.18	1.1
	750	270	0.27	0.18	1.15
Set 3	750	280	0.35	0.1	1.20

2.1.2 Graphene transfer procedure

A single graphene layer was then transferred using a wet chemical etching process. Commercially available, high-quality, single-layer graphene grown on copper foil and coated with poly(methyl methacrylate) polymer (PMMA) was used for this process. The Cu substrate was etched with an ammonium persulfate solution, resulting in a floating graphene/PMMA flake on the surface of the etching solution. The graphene/PMMA flake was then rinsed several times in deionized water and transferred onto the deposited Al_2O_3 layer. The PMMA, which served as a support and protective layer for the graphene, was removed from the graphene surface and the two electrodes were thermally deposited onto the graphene layer. The configuration of these electrodes was such that one of them was common (connected) to one of the manganite electrodes and the other was separate. The distance between these electrodes was 100 μm and the width was 0.7 mm).

2.1.3 Characterisation of graphene and manganite structure

Characterisation of transferred graphene single layer was performed by using Raman spectroscopy. Raman spectra were recorded using the InVia Raman microscope (Renishaw, UK) equipped with a thermoelectrically cooled (– 70 °C) CCD detector and 532 nm laser radiation source. The step size was 4×4 μm in x- and y directions; each map consisted of 50 measurements with 20 s acquisition time at 0.23 mW laser power focused on a sample using 50×/0.75NA objective lens (Leica). 2D and G intensity ratio (2D/G) was plotted using Wire 5.5 (Renishaw, UK). The high 2D/G ratio value (2.9) indicated a single layer, pristine and high-quality graphene.

Characterisation of LSMO film nanostructure was performed using different methods. The Inductively Coupled Plasma High-Resolution Mass Spectrometry (ICP-MS) was used to determine the composition of the films. To study the surface morphology of the films a Scanning Electron Microscope (SEM) (Hitachi SU70) was used. The crystalline structure of the films was investigated by using a Transmission Electron Microscope (TEM) (Tecnai G2F20 X-TWIN) with an Energy Dispersive X-ray spectrometer (EDAX). Also the surface of the LSMO film without and with Al_2O_3 protecting film was characterized using atomic force microscope (AFM). Magnetic characteristic measurements were carried out in magnetic fields up to 50 kOe with an MPMS-5 SQUID (Quantum Design) magnetometer, and the dependences of the magnetic moment on magnetic field at selected temperatures were recorded. The magnetic hysteresis loops were measured after field-cooling at 1000 Oe in the temperature range from 320 K down to 220 K. Magnetization measurements were performed at the Institute of Physics of the Polish Academy of Sciences.

2.2 Measurement equipment and methods

2.2.1 Resistivity and low-field magnetoresistance measurement system

The resistivity and low-field magnetoresistance were measured in the temperature range of T = (5–310) K and (25–300) K, respectively, using a closed-cycle helium gas cryocooler (Janis 4K) and electromagnet (up to 0.8 T). The resistance itself was measured using a two-point measurement configuration. The special preparation technology of electrodes with bifilarly twisted wires makes this possible [6]. The main setup is shown in Figure 2.2.1.

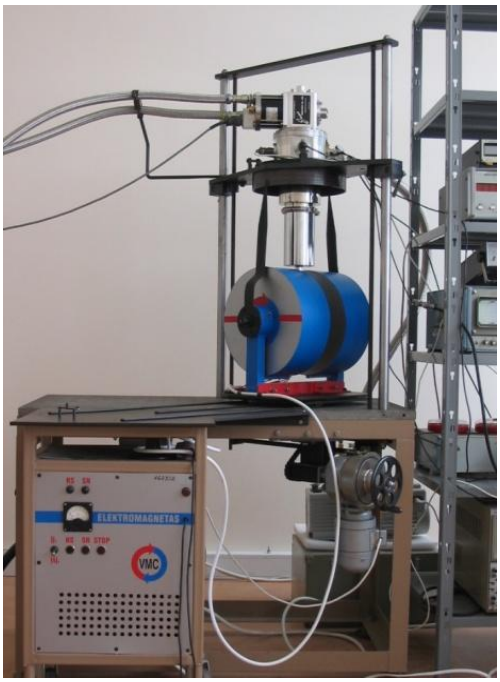


Figure 2.2.1 Resistivity and low-field magnetoresistance measurement system.

2.2.2 Measurement system of magnetoresistance dependence on field direction

Magnetoresistance measurements were conducted in DC magnetic field produced by an electromagnet capable of producing 2.4 T between the poles of a magnetic field concentrator. The experimental setup is presented in Figure 2.2.2. The sample was placed inside a temperature stabilized column in between the poles of an electromagnet. The sample itself was connected to a rod that extended outside of the magnet where the rod could be rotated manually. Once temperature stabilized, magnetic field was applied and resistance values were recorded while rotating the sample from 0 to 180°. After that, the magnetic field was increased and the procedure repeated.

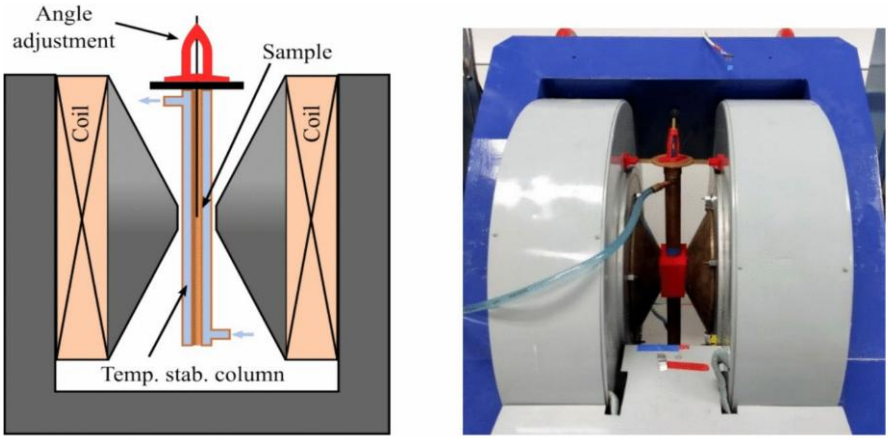


Figure 2.2.2 Schematic (left) and picture (right) of the experimental setup. The temperature stabilized column placed in the middle of the magnetic poles of the electromagnet. The angle adjustment handle is visible on the top of the compass.

2.2.3 Measurement of magnetoresistance in high magnetic fields

The high-field magnetoresistance measurements were performed in pulsed magnetic fields up to 20 T in the temperature range of 80–363 K using a pulsed magnetic field generator based on capacitor bank discharge through a non-destructive coil. The main high magnetic pulse generator block scheme is shown in Figure 2.2.3. Here: 1 – charge/discharge control device, 2 – capacitor bank charging unit, 3 – capacitor bank, 4 – high power semiconductor switch, 5 – coil, 6 – measurement device.

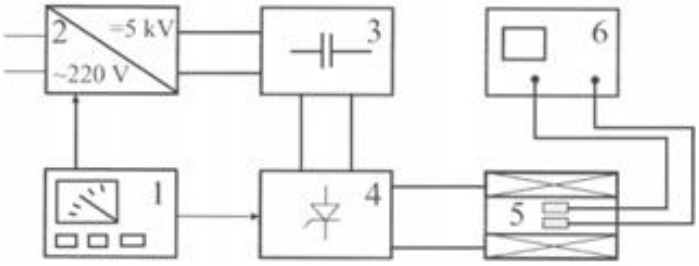


Figure 2.2.3 High magnetic field pulse generator block scheme.

3. RESULTS AND DISCUSSION

3.1 Magnetoresistance of nanostructured lanthanum manganite films

This subchapter investigates the influence of chemical composition on the magnetoresistance of non-stoichiometric nanostructured $La_{1-x}Sr_xMn_yO_3$ films grown on polycrystalline Al_2O_3 substrates. The results cover the temperature range 5–300 K and different magnetic field conditions [P1].

3.1.1 Morphology and microstructure of LSMO films

Figure 3.1.1 shows the surface morphology of LSMO films prepared with different Sr content (x) and a constant Mn excess of y = 1.15. For x = 0.08 (Figure 3.1.1a), the surface consists predominantly of triangular crystallites, together with some polygonal grains. Larger islands containing crystallites of different shapes and sizes are also visible. Their formation may be associated with the structure of the polycrystalline substrate. It should be noted that polycrystalline Al_2O_3 substrates are made from an ingot that consists of grains about 2 micrometres in size. When bulk ceramic is cut into plates, the substrate surface is formed by grains of different sizes and crystallographic planes. Therefore, during the initial growth process, the LSMO film starts to grow on different planes and sizes of Al_2O_3 crystallites, which results in islands with crystallites of different shapes and sizes. Some islands show well-ordered crystallites with a triangular shape. As is known, Al_2O_3 has a trigonal Bravais lattice close to hexagonal. Most likely, in these regions of the substrate the Al_2O_3 crystals are oriented in the C-plane parallel to the surface, and at the initial stage of film growth the nuclei are oriented so that their pseudocubic axis [111] is perpendicular to the surface. As a result, a well-oriented film texture is obtained. In other areas of the substrate surface, the crystallites grow with a more disoriented structure. The surface morphology of the films with x = 0.18 (Figure 3.1.1b) is slightly different. These films consist of crystallites whose surfaces are not only triangular, but increasingly elongated and rectangular, with these crystallites gradually becoming dominant. A further increase in Sr content (Figure 3.1.1c, x = 0.30) leads to the predominance of crystallites with this elongated rectangular surface. In addition, islands containing smaller, triangular crystallites are present in all samples. The average crystallite dimensions do not strongly depend on the Sr content. The most frequently observed crystallite dimensions are 75 nm for x = 0.08, 80 nm for x = 1.18, and 85 nm for x = 0.3. The change in the shape of the crystallite surface with increasing Sr content may be caused by deformation of the crystal

lattice or a change in the crystal structure. This can result in a preferred crystallite orientation perpendicular to the substrate surface. Consequently, a different cut of the crystallite surface is observed.

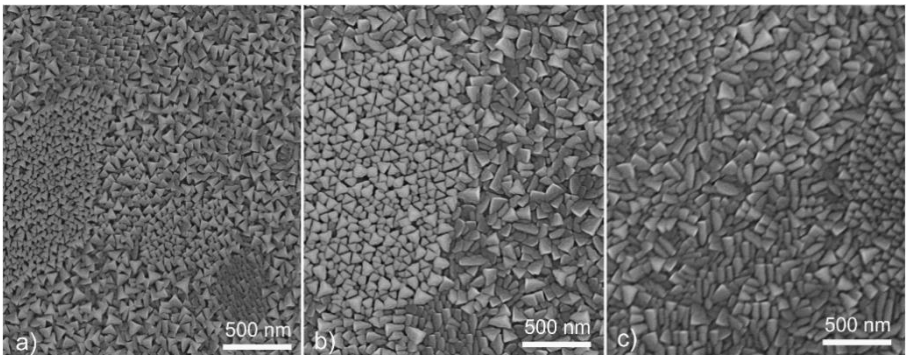


Figure 3.1.1 SEM surface images of LSMO films with different Sr content (x) and constant content of Mn/(La + Sr) (y = 1.15): (a) x = 0.08, (b) x = 0.18, (c) x = 0.3.

Cross-sectional TEM images were examined to obtain further insight into the growth morphology. Figures 3.1.2a and 3.1.2b show films with Sr contents of 0.08 and 0.18, respectively. The films contain vertically aligned columns extending through their thickness, with their long axes perpendicular to the substrate. Typical column widths are approximately 60–75 nm near the upper surface and 30–50 nm close to the substrate.

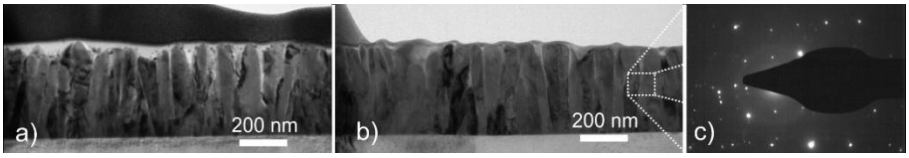


Figure 3.1.2 TEM images of the LSMO films with different Sr content (x) and constant Mn content (y = 1.15): (a) x = 0.08, (b) x = 0.18. (c) Selected area electron diffraction pattern from the region shown in Figure 3.1.2b of the film with Sr content x = 0.18.

At an Sr content of x = 0.08, the films exhibit a porous columnar microstructure. Voids occur both within and between the columns, producing a pronounced dendritic pattern. Separate crystallites are also present, particularly near the substrate. Variations in TEM contrast indicate that individual columns comprise several single-crystal slabs rather than forming a continuous single crystal. The large steps created by these slabs widen the spaces between neighbouring crystallites. Increasing the Sr content improves the structural quality of the columns and their boundaries. At x = 0.18, the lateral crystallite surfaces and adjoining boundaries are flat, without the steps

or zigzag features observed at lower Sr content (Figure 3.1.2b). Although the crystallites have different in-plane orientations, each is monocrystalline, as indicated by the diffraction spots in Figure 3.1.2c. Films with $x = 0.3$ have a microstructure similar to that observed at $x = 0.18$.

3.1.2 Resistivity and metal-insulator transition temperature of nanostructured LSMO films: dependence on Sr content and excess of Mn

As discussed in Chapter 1, the electrical and magnetic behaviour of lanthanum manganites can be understood in terms of double-exchange interactions between Mn^{4+} and Mn^{3+} ions, together with the Jahn-Teller effect. The temperature dependence of resistivity provides an important means of characterising this behaviour. A characteristic feature is the metal-insulator transition at temperature T_m. In monocrystalline films, T_m generally lies close to the Curie temperature, T_C, and is considered to reach its highest value at an Mn^{4+}/Mn^{3+} ratio of 1/3 [14, 16, 41]. Sr substitution controls this ionic ratio. Mn excess provides another means of changing it: even in insulating $LaMnO_3$ films, additional Mn can induce La vacancies and thereby increase the proportion of Mn^{4+} ions [101]. The corresponding relationship may differ in nanostructured polycrystalline films because growth-related lattice distortions and defects influence their electrical and magnetic properties. In particular, La vacancies associated with Mn excess can produce substantial changes in the behaviour of polycrystalline films [102].

The influence of composition on the metal-insulator transition was examined by measuring the temperature dependence of resistivity in nanostructured LSMO films with different $x = Sr/(La + Sr)$ and $y = Mn/(La + Sr)$ ratios. The resulting transition temperatures, T_m, are compared in Figure 3.1.3.

The results show that increasing the Mn/(La + Sr) ratio generally raises T_m, with the strongest compositional influence occurring at low Sr concentrations. The maximum in the T_m dependence on Sr content also shifts slightly towards lower x as the Mn ratio increases. One possible explanation is that additional Mn promotes the formation of La vacancies, increasing the proportion of Mn^{4+} ions [101]. Consequently, less Sr would be required to produce the same Mn^{4+}/Mn^{3+} ratio. At each Sr content, the increase in T_m becomes progressively smaller as the Mn/(La + Sr) ratio rises, indicating saturation. The highest transition temperatures are obtained for $y = 1.15$ and $x = 0.15$–0.18. Epitaxial films grown on LAO show a different compositional dependence: T_m increases throughout the investigated interval, $0.05 \leq x \leq 0.3$, and reaches its maximum at the upper end of this range (Figure 3.1.3). Their transition temperatures are

also higher than those of films deposited on Al_2O_3. These differences may originate from the film microstructure. In polycrystalline films, electrical transport depends on both double exchange through Mn^{3+} – O – Mn^{4+} pathways and the resistance and relative contribution of grain boundaries [103, 104]. The degree of boundary disorder and the amount of boundary material can therefore strongly influence the measured resistivity.

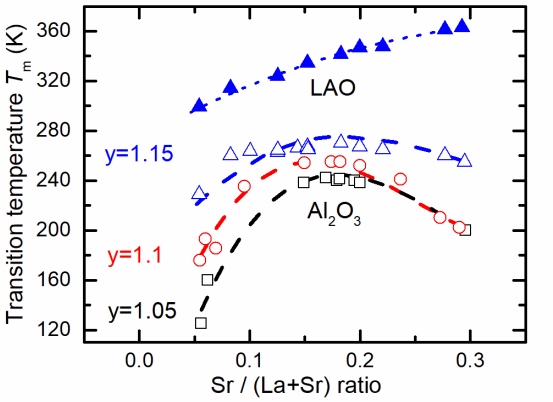


Figure 3.1.3 T_m dependence on Sr content x in nanostructured Al_2O_3//LSMO and epitaxial LAO//LSMO films with different y = Mn/(La + Sr) ratios (symbols). Curves — fit to eyes.

Figure 3.1.4 compares the temperature dependence of resistivity, ρ, for two sets of LSMO films: films with different Sr content at a fixed Mn excess (Figure 3.1.4a), and films with different Mn excesses at a fixed Sr content (Figure 3.1.4b). Each film exhibits a resistivity maximum, ρ_m, at the metal-insulator transition temperature T_m, separating the metal-like and insulator-like regimes. Figure 3.1.3 summarises the corresponding transition temperatures for all investigated compositions. At a constant Mn content, increasing x initially raises T_m, which reaches a maximum at x = 0.15–0.18 before decreasing at higher Sr content. In contrast, ρ_m decreases continuously across the full interval, $0.05 \leq x \leq 0.3$. For the comparison of Mn excesses, $x = 0.18$ was selected as a representative of Sr content near the maxima observed for the different Mn ratios. In this series, increasing Mn excess raises T_m while reducing resistivity. A previous study reported a transition temperature of 285 K when the Mn ratio was increased to 1.21 [102]. However, compositions with $y > 1.15$ exhibit greater non-stoichiometry, making it more difficult to maintain homogeneous films containing only the LSMO phase. The Mn ratio in the present series was therefore limited to $y \leq 1.15$ to maintain a single-phase structure.

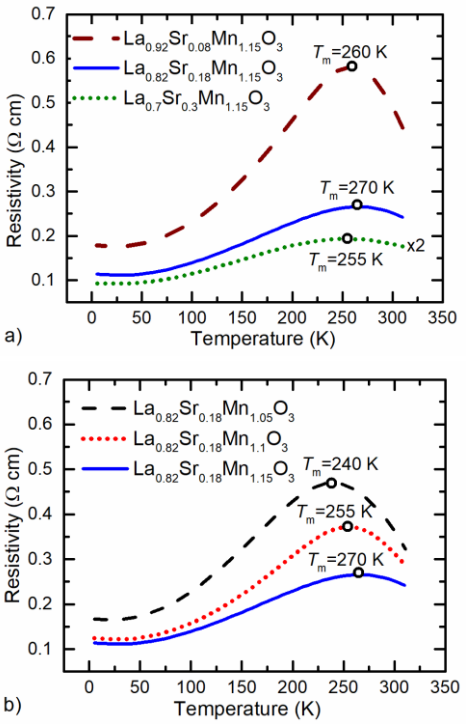


Figure 3.1.4 Resistivity *vs*. temperature dependences of LSMO films with different Sr/(La + Sr) (a) and Mn/(La + Sr) (b) contents.

3.1.3 Magnetoresistance of nanostructured LSMO films

Magnetoresistance (*MR*) was defined according to Equation (1.4.1), taking into account the resistivity of different films:

$$MR(B) = 100\% \times (\rho(B) - \rho(0))/\rho(0) \qquad (3.1.1)$$

where $\rho(B)$ and $\rho(0)$ is resistivity at the applied magnetic flux density B and at zero magnetic field, respectively.

The magnetoresistance dependences on magnetic flux density (B), measured up to 0.2 T at room temperature (290 K), are presented in Figure 3.1.5. The magnetic field was applied in parallel to the film plane. For nanostructured films with Sr content x = 0.18–0.3, a sharp increase in negative magnetoresistance (a large decrease in electrical resistance) at low fields is observed, followed by a much slower increase of negative *MR* with increasing in magnetic field (see Figure 3.1.5a). These effects are usually referred as low-field magnetoresistance (LFMR) and high-field magnetoresistance (), respectively. Furthermore, one can observe some positive *MR* changes at low magnetic fields, with maxima attributed to the films' coercive field.

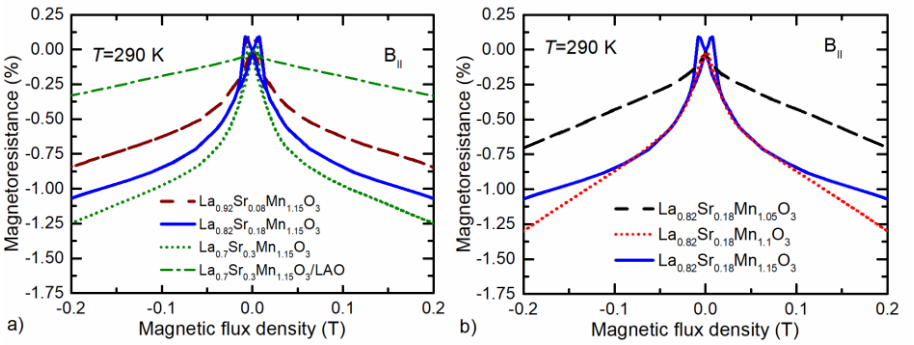


Figure 3.1.5 Low-field magnetoresistance dependences on magnetic flux density for nanostructured films with different Sr content (a) and Mn excess (b). In addition, the dependence for the epitaxial LAO//LSMO film (x = 0.3, y = 1.15) is shown in (a) for comparison. Measurements were performed at ambient temperature 290 K.

In our investigated samples, the LFMR was strongly dependent on the content of Sr. For films with x = 0.3, the LFMR is approx. –0.8% at 50 mT, while for films with x = 0.08, it is approx. –0.48%. At higher fields (0.8 T, not shown in this figure), the HFMR was –4% and –2.5%, respectively. It should be noted that for epitaxial films grown on monocrystalline LAO substrates the LFMR was not observed in all investigated films (see Figure 3.1.5a for x = 0.3). This result suggests that the LFMR is primarily associated with the crystallite and grain-boundary structure of the LSMO films, rather than with changes in the crystal lattice caused by varying Sr content. For nanostructured films with different Mn excess (Figure 3.1.5b), the similar LFMR values were obtained for y = 1.1 and 1.15, while for y = 1.05 the LFMR was very small. However, at 0.8 T the highest LFMR of 4.5% was found for the film with a Mn excess ratio of 1.1. This increase in *MR* at a higher field could be related to a slightly higher disorder level in the grain boundary material, as confirmed by higher resistivity values. Therefore, the higher magnetic field could align Mn moments and, as a result, the resistance change with magnetic field is larger. It should be noted that the LFMR is usually not observed in epitaxial films or monocrystalline manganites [44] but found in films with a large number of grain boundaries having a non-collinear spin structure, in which spin-polarised transport (tunnelling) across the grain boundaries dominates. The LFMR is more pronounced at low temperatures and depends on the thickness and type of grain boundaries, because they decouple the neighbouring ferromagnetic (FM) grains and provide an energy barrier for spin-polarised tunnelling of electrons. The LFMR usually vanishes at room temperature, at which the grains become paramagnetic. However, as shown in Figure 3.1.5, this effect can also be obtained at room temperature for the specific chemical

composition of nanostructured films. This result is promising for the application of LSMO films in low magnetic field sensing at room temperature. It is also worth noting that the LFMR increases continuously with increasing Sr content. This is in contrast to the dependence of T_m on Sr content for nanostructured films (see Figure 3.1.3), for which we observe a decrease in T_m when $x > 0.2$. Moreover, Mn excess significantly influences the LFMR values of the films. This effect was observed at room temperature only for Mn concentrations higher than $y = 1.1$. As shown in Figure 3.1.5b, for Mn concentration $y = 1.05$ (almost stoichiometric films), the LFMR is negligible.

As it was already mentioned, the low-field magnetoresistance is more pronounced at low temperatures. The *MR* of nanostructured LSMO films with Mn excess $y = 0.15$ was measured in the temperature range of (250–290) K. Figure 3.1.6 presents summarised results obtained at two magnetic flux density values: $B = 0.05$ T (a) and 0.8 T (b). It can be seen that the *MR* values gradually increase with decreasing temperature and are highest for films with $x = 0.3$. Therefore, nanostructured films with the chemical composition $La_{0.7}Sr_{0.3}Mn_{1.15}O_3$ could be used for magnetic field sensor applications at room temperature.

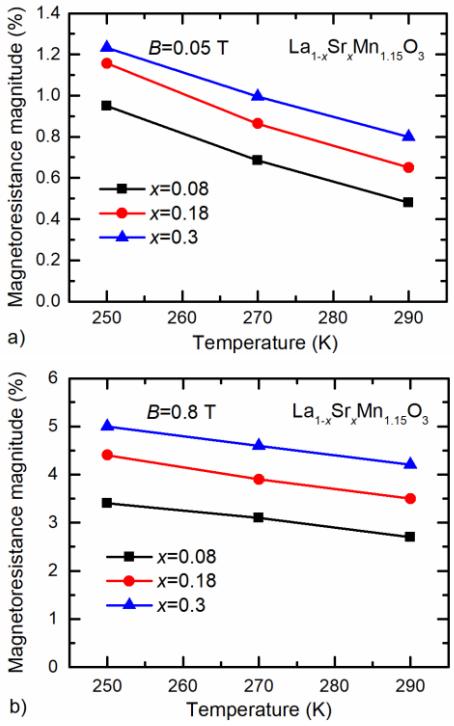


Figure 3.1.6 Temperature dependence of magnetoresistance magnitude of nanostructured LSMO films with Mn excess $y = 1.15$ and different Sr content. Measurements were performed at $B = 0.05$ T (a) and $B = 0.8$ T (b).

The high-field magnetoresistance dependences on Mn excess are presented in Figure 3.1.7. One can see that the highest *MR* values at room temperature are obtained for films with Mn excess (y = 1.1–1.15).

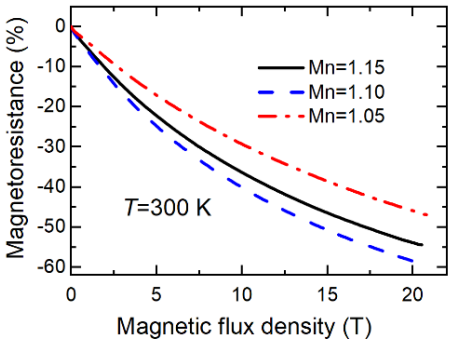


Figure 3.1.7 The *MR vs*. magnetic field dependences of $La_{1-x}Sr_xMn_yO_3$ films with x = 0.2 and different ratios y = Mn/(La+Sr) at 300 K, when a magnetic field was applied parallel to the film plane.

To explain the observed LFMR at room temperature, the magnetisation measurements of these films were carried out.

Figure 3.1.8 shows the temperature dependence of the magnetisation (M), measured after field cooling at 1000 Oe. To enable comparison between compositions, each curve was normalised to the magnetization measured at 10 K. Magnetisation decreases as temperature increases, and all films exhibit a transition from ferromagnetic to paramagnetic behaviour. The Curie temperature, T_C, was identified from the minimum in dM/dT. For the film with x = 0.08, this analysis gives T_C = 300 K. For the remaining compositions, the available measurement range was insufficient to determine T_C directly. Their Curie temperatures were therefore estimated by fitting the experimental data using the Curie-Weiss relation:

$$M=a/(T-\theta)+b \qquad (3.1.2)$$

where $a, b,$ and θ are fitting constants. The curves in Figure 3.1.8 present the fitting results. For the films with x = 0.18 and 0.3, the following T_C values were estimated: 343 K and 383 K, respectively. Thus, the T_C of all films with Mn excess of 1.15 is higher than room temperature, and this explains the LFMR effect observed at room temperature. In addition, it should be noted that the T_C for the film grown on polycrystalline Al_2O_3 and monocrystalline LAO substrates is almost the same, and only the slope of the curves in the region below the transition temperature differs. The studies performed by Chen et al. [105] and Moshnyaga et al. [106] show that the interface strain has a significant effect on the T_C of the manganite-based composites films. In these

studies, the interface strain between the LSMO and NiO nanocolumns causes the LSMO to be in a tensile strain state along the out-of-plane direction, resulting in the changes in the length and angle of Mn–O–Mn bonds. The electron transfer integral of Mn^{3+}–O–Mn^{4+} is reduced and the double-exchange interaction is weakened, leading to a decrease in T_C. In our case, the films consist of column-shaped crystallites that extend throughout the entire film thickness, with their long axes arranged perpendicular to the substrate. The typical column width in all films is about 70–80 nm, and the grain boundary width is only about 2–3 nm. This structure, with sufficiently large crystallites separated by narrow grain boundaries in films with higher Mn and Sr content, could explain why the T_C of films grown on monocrystalline and polycrystalline substrates is similar.

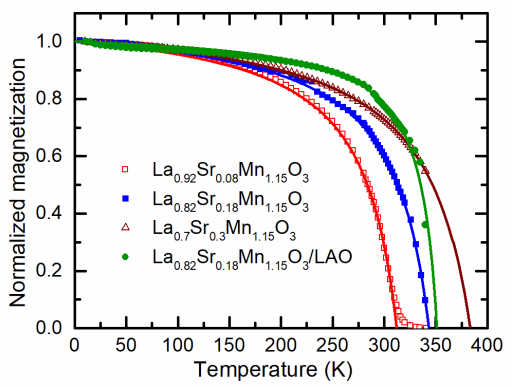


Figure 3.1.8 Symbols – temperature dependence of field-cooled (FC) (H_{FC} = 1000 Oe) magnetization, normalized to the magnetization at 10 K, for films with different Sr content and constant Mn content y = 1.15. Lines – fitting results using the *Curie-Weiss* law approximation (see Equation 3.1.2).

The magnetic hysteresis loops recorded after field-cooling at 1000 Oe in the temperature range from 320 K down to 220 K for the investigated nonstoichiometric (y = 1.15) films are shown in Figure 3.1.9. The saturation magnetisation (M_{sat}) of the films with Sr content of x = 0.08 (Figure 3.1.9a) is smaller than that of the LSMO film with x = 0.3, which may be attributed to the weakened double-exchange interaction and the spin disorder at crystallite-grain boundary interfaces. For example, at temperature T = 220 K the maximal magnetisation of the films with x = 0.08 equals to M = 840 ± 10 emu/cm^3, whereas for films with x = 0.3 it is 1004 emu/cm^3. These are quite large values. For comparison, it was shown in [107] that even at a temperature of 10 K the maximal magnetisation for stoichiometric $La_{0.7}Sr_{0.3}MnO_3$ manganite films was only about 550 ± 10 emu/cm^3. When comparing two films with different Sr contents, it can be seen that at 320 K and x = 0.08, M does not

saturate even at a magnetic field of 50 kOe, whereas when x increases to 0.3, the $M-H$ loops are already saturated at 10 kOe with $M = 870 \pm 10$ emu/cm^3 at room temperature. This means that at this temperature, films with Sr concentration of $x = 0.08$ are in the paramagnetic phase, while films with $x = 0.3$ and $y = 1.15$ are in the saturated ferromagnetic state. Moreover, the hysteresis of this film at room temperature is very narrow, and the coercive field is approximately 2–3 mT. It should be noted that LFMR is associated with a large number of thin grain boundaries with a non-collinear spin structure, good magnetic connectivity between the grains, and a high saturation magnetic moment of the grains. To increase the magnitude of LFMR, many groups have attempted to grow manganite-based nanocomposites by incorporating a secondary insulator phase into single-phase films and introduction and to introduce the artificial GBs [107–111].

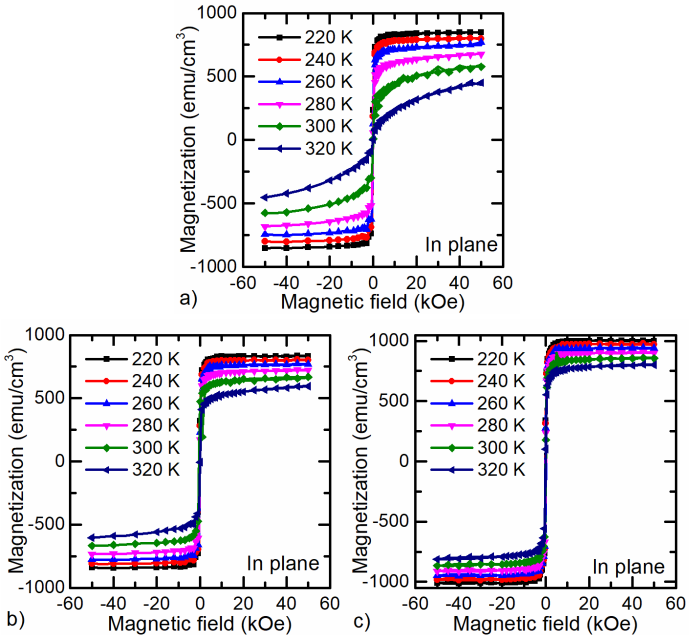


Figure 3.1.9 Magnetic hysteresis loops of LSMO films with different Sr content (a) $La_{0.92}Sr_{0.08}Mn_{1.15}O_3$, (b) $La_{0.82}Sr_{0.18}Mn_{1.15}O_3$, and (c) $La_{0.70}Sr_{0.3}Mn_{1.15}O_3$, over the temperature range 320–220 K along the in-plane direction.

Our research has shown that such results can be achieved without incorporating of the second phase, simply by growing single-phase vertically aligned nanostructures with increased excess of Mn and the optimising the chemical composition of Sr/(La + Sr) in the films. Increasing the Sr content up to 0.3 when the Mn excess in the films exceeds 1.15 leads to higher saturation magnetisation of the column-like crystallites, even at room temperature. Moreover, such composition of the films allows to obtain

crystallites with thinner grain boundaries and improved quality. As a result, the LFMR in such nanostructured films could be observed at room temperature.

For the application of manganite films as low magnetic field sensors, the sensitivity of the measured signal response to changes in magnetic field is very important. In contrast to GMR sensors, whose magnetoresistance saturates at a certain low magnetic field, the magnetoresistance of polycrystalline films exhibiting the CMR effect does not saturate up to very high fields (only the slope of the *MR* dependence on *B* decreases). Therefore, the sensitivity of CMR films can be described as the normalised value of the voltage change across the sensor resistance R_S for an increase in magnetic field of 1 T: $S = \delta(V_{out}/V_0)/\delta B$. The maximal value of sensitivity $S = 137$ mV/V·T at room temperature (T = 290 K), was obtained and remained almost constant up to 10 mT for the film with $x = 0.3$. Then, it gradually decreased to $S = 15$ mV/V·T at a magnetic flux density $B > 100$ mT. The other films with $x = 0.18$ and $x = 0.08$ showed lower sensitivity values: $S = 96$ mV/V·T and $S = 85$ mV/V·T up 10 mT, respectively. A decrease in the temperature increases the *MR* of the films and their sensitivity as well. The sensitivity of the film with $x = 0.3$ at $T = 270$ K was $S = 185$ mV/V·T up to 10 mT, while at $T = 250$ K it was $S = 235$ mV/V·T. This provides the opportunity to develop more sensitive sensors with external cooling options if higher sensitivity is required.

The obtained results indicate that nanostructured $La_{1-x}Sr_xMn_yO_3$ films with $x = 0.3$ and $y = 1.15$, grown on polycrystalline Al_2O_3 substrates, could be used to develop sensors with predetermined characteristics for weak magnetic field measurements at room temperature. For high-field measurements, films with $x = 0.1$–0.2 are preferable.

3.2 Accelerated ageing of nonstoichiometric LSMO films

This subchapter presents the results of an investigation of accelerated thermal ageing of nonstoichiometric nanostructured $La_{1-x}Sr_xMn_yO_3$ films grown on a polycrystalline Al_2O_3 substrate revealing the ageing mechanisms and their influence on the stability of the resistance and magnetoresistance values of these films [P2].

The results of previous chapters have demonstrated that polycrystalline thin films of lanthanum strontium manganite $La_{1-x}Sr_xMn_yO_3$ (LSMO) are technologically important materials because of their colossal magnetoresistance (CMR) over a wide range of temperatures and magnetic fields [4, 10, 11, 35, 63]. These properties make LSMO films suitable for magnetic-field sensing in extreme environments. Compared with Hall, B-dot

and optical Faraday-effect sensors, CMR-B-scalar sensors based on nanostructured manganite films can operate in very high magnetic fields, have weak directional sensitivity and can be used over short time scales and broad temperature intervals.

The main operating principle of such sensors is based on the magnetic field dependence of the electrical resistivity. However, the initial resistance and magnetic field sensitivity are strongly affected by ambient temperature and by the long-term stability of the film structure [73, 74]. Therefore, stabilisation of transport properties is a critical requirement for reliable practical use. In nanostructured manganite films, ageing is associated mainly with defect migration, oxygen vacancy redistribution and relaxation of disordered grain-boundary regions [78, 81, 82, 84, 112].

A separate motivation for the present study is the use of nonstoichiometric $La_{1-x}Sr_xMn_yO_3$ films with excess manganese. Increasing the Mn/(La + Sr) ratio above unity can shift the metal-insulator transition temperature T_m to higher values and reduce resistivity near T_m, which is beneficial for high-temperature and pulsed-field sensor applications [102]. Nevertheless, the influence of accelerated ageing on the magnetotransport properties of Mn-excess films has not been sufficiently clarified. For this reason, the films with $y = 1.05$ and $y = 1.15$ were studied and analysed to determine how manganese nonstoichiometry and grain-boundary structure affect resistance drift and magnetoresistance stability.

3.2.1 Structural and compositional characterisation of the LSMO films

TEM observations (see Figure 3.2.1) showed that films with manganese excess have a columnar microstructure similar to the nominally stoichiometric films. The columns extend through the entire film thickness, and their long axes are mainly perpendicular to the substrate. The typical column width was

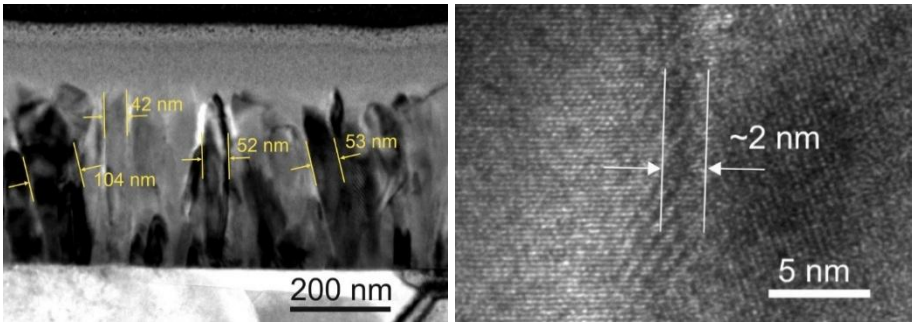


Figure 3.2.1 Cross-sectional TEM images of the Al_2O_3//LSMO film with $y = 1.15$: (a) low-magnification bright-field image showing the columnar microstructure; (b) high-resolution HRTEM image of the grain boundary between two crystallites.

approximately 40–100 nm, while the grain-boundary regions between neighbouring crystallites had widths from approx. 2 nm to 10 nm. These intergranular regions are important because they contain structural disorder and act as preferential pathways for oxygen diffusion during ageing.

STEM-EDX analysis demonstrated that the grain-boundary regions differ chemically from the crystallite interiors. Figure 3.2.2a shows the STEM image of the film and the line along which the distributions of La, Sr, Mn, and C were scanned. The image contrast was influenced by the density and chemical composition of the film. The normalised profiles of these elements across the grain boundary are presented in Figure 3.2.2b. In the Mn-excess film, the main elements La, Sr and Mn decreased in the region where the carbon concentration increased, which indicates accumulation of carbon-containing residues in grain boundaries during MOCVD growth. In Figure 3.2.2c, a normalised profile of only the main elements (La, Sr, and Mn) is presented. It can be seen that at the boundary between the two crystallites, there was an increased concentration of Mn relative to La, with this increase extending over approximately 6 nm. A local increase in the Mn/La ratio was also observed near the boundary region. For the film with $y = 1.05$ (see Figure 3.2.2d, e, f), such pronounced Mn enrichment was not detected. These data confirm that the Mn excess in films with $y = 1.15$ is reflected not only in the average composition but also in the local grain-boundary chemistry.

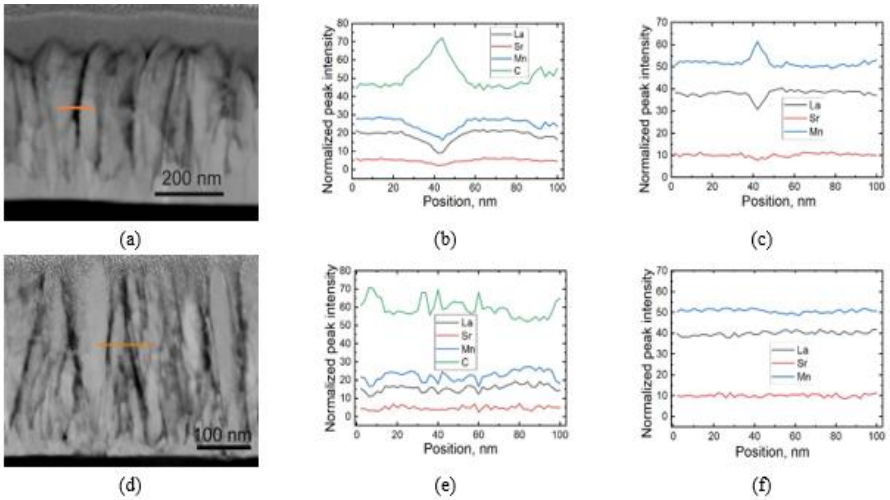


Figure 3.2.2 STEM-EDX analysis of Al_2O_3//LSMO films: (a,d) STEM images showing the line used for elemental scanning; (b,e) normalised peak intensities of La, Sr, Mn and C; (c,f) normalised peak intensities of La, Sr and Mn. Panels (a–c) correspond to the film with $y = 1.15$, while panels (d–f) correspond to the film with $y = 1.05$

X-ray diffraction (see Figure 3.2.3) confirmed that both compositions formed polycrystalline LSMO with a perovskite-like rhombohedral structure. The diffraction peaks of the $y = 1.15$ film were shifted slightly towards higher 2θ values compared with the $y = 1.05$ film, indicating a reduction in the lattice parameter. This behaviour can be associated with an increased fraction of Mn^{4+} ions, which have a smaller ionic radius than Mn^{3+}. The broader peaks in the Mn-excess film also suggest a higher level of microstrain or structural disorder.

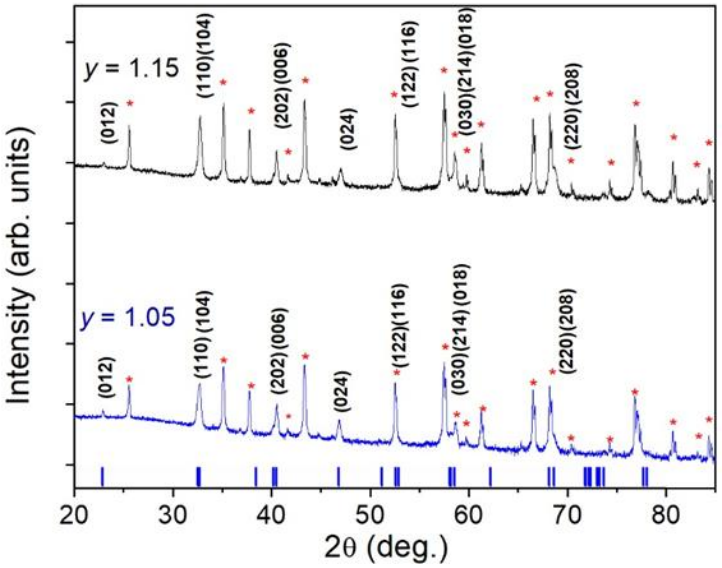
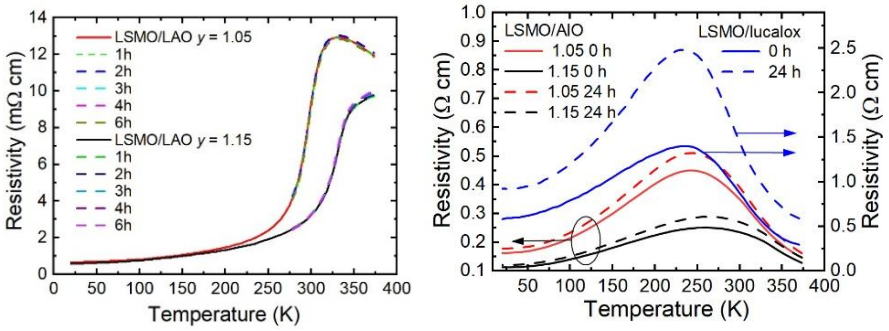


Figure 3.2.3 X-ray diffraction spectra of LSMO films with $y = 1.15$ and $y = 1.05$. The stars indicate characteristic peaks of the Al_2O_3 substrate, while the sticks indicate modelled LSMO peak positions for rhombohedral distortion.

3.2.2 Influence of accelerated ageing on resistivity

The resistivity measurements (see Figure 3.2.4) showed that manganese content and substrate type strongly affect the electrical transport properties. In films grown on monocrystalline $LaAlO_3$, thermal treatment at 100 °C in Ar caused almost no change in resistivity or in the metal-insulator transition temperature (Figure 3.2.4a). This indicates that the crystallites themselves are stable under the selected ageing conditions. In contrast, polycrystalline films grown on Al_2O_3 and lucalox substrates exhibited a clear increase in resistivity after ageing, showing that the dominant ageing processes occur in the grain boundaries (Figure 3.2.4b).



(a) (b)

Figure 3.2.4 Resistivity versus temperature dependences: (a) LSMO films grown on monocrystalline $LaAlO_3$ after different accelerated ageing times; (b) LSMO films grown on polycrystalline Al_2O_3 and lucalox substrates before and after 24 h of thermal treatment at 100 °C in Ar atmosphere.

The relative resistivity change $(\rho_t - \rho_0)/\rho_0$ during ageing (Figure 3.2.5) was described using a stretched-exponential relaxation model [81,82, 84]. This model is suitable for topologically disordered systems where individual relaxation events are not independent but are limited by previous local rearrangements in the structure. The normalised resistivity change was expressed as:

$$(\rho_t - \rho_0)/\rho_0 = [(\rho_\infty - \rho_0)/\rho_0] \times \{1 - \exp[-(t/\tau)^k]\}. \quad (3.2.1)$$

Here ρ_0 is the initial resistivity, ρ_t is the resistivity after ageing time t, ρ_∞ is the limiting resistivity after long ageing time, τ is the characteristic relaxation time and k is the stretching exponent. For films on Al_2O_3, the fitting parameters were similar for the two Mn concentrations: $\tau = 8.5$ h and $k = 0.75$ for $y = 1.05$, and $\tau = 6.8$ h and $k = 0.68$ for $y = 1.15$. Values of $k > 0.6$ indicate a hierarchically limited relaxation mechanism [81]. The lucalox-based film showed a much larger resistivity change, confirming that grain-boundary disorder has a stronger influence on ageing than the small difference in Mn non-stoichiometry.

It should be noted that despite the change in film resistance after the accelerated ageing procedure, no significant changes in the X-ray diffraction patterns were observed for the investigated films. This indicates that annealing at 100 °C did not alter the crystalline structure of the films. The results suggest that the ageing process involves only weakly bound oxygen, and that oxygen loss and diffusion occur mainly along grain boundaries rather than as a result of structural modification of the crystallites. It was found, that accelerated thermal ageing at 100 °C for 20 hours stabilises the resistance of nonstoichiometric $La_{1-x}Sr_xMn_yO_3$ films, and it remains unchanged within 5 %

during longer period (tested after 6 months), regardless of further increase in resistance during longer thermal treatment (see Figure 3.2.5).

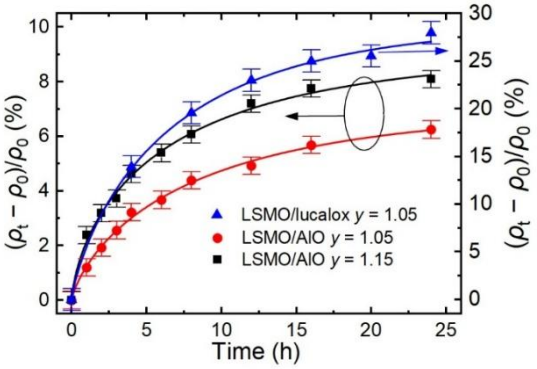


Figure 3.2.5 Kinetics of relative resistivity change measured at 300 K during accelerated ageing of LSMO films with y = 1.05 and y = 1.15 grown on Al_2O_3 substrates, and of the y = 1.05 film grown on lucalox. Points are experimental data and curves are fits to Equation (3.2.1).

For temperatures above T_m, the resistivity data were analysed using Mott variable range hopping (VRH) [28]. This model describes charge transport in the paramagnetic state, where carriers are localised by random spin-dependent potentials and hop between localised states. Considering Equation (1.3.2), the resistivity is written as:

$$\rho = \rho_\infty \exp[(T_0/T)^{1/4}] \tag{3.2.2}$$

The characteristic temperature T_0 is related to the localisation length a and the density of states at the Fermi level $N(E_F)$ as follows:

$$T_0 = 18/[a^3 \, k_B \, N(E_F)] \tag{3.2.3}$$

Figure 3.2.6 presents the resistivity versus temperature data at different accumulated annealing times for the sample with y = 1.15, fitted using Mott's VRH model. The experimental data agree well with Equation (3.2.2) at temperatures higher than 340 K. This suggests that the conduction mechanism at temperatures above T_m is governed by Mott variable range hopping of the localised charge carriers. Figure 3.2.7 shows the change in localisation length during annealing for different samples. These values were calculated according to Equation (3.2.3). It should be noted that the obtained values have no physical meaning because the localisation length must exceed the Mn^{3+} – Mn^{4+} distance [28]. However, the change in localisation length with thermal treatment time can be used in the analysis of charge-carrier transport. The decrease in localisation length during annealing supports the conclusion that oxygen depletion limits the Mn^{3+} – O – Mn^{4+} double-exchange pathway. The largest change occurred during the first few hours of treatment, after which

the system approached a more stable state. Similar results were obtained in our previous study on stoichiometric lucalox//LSMO films [73].

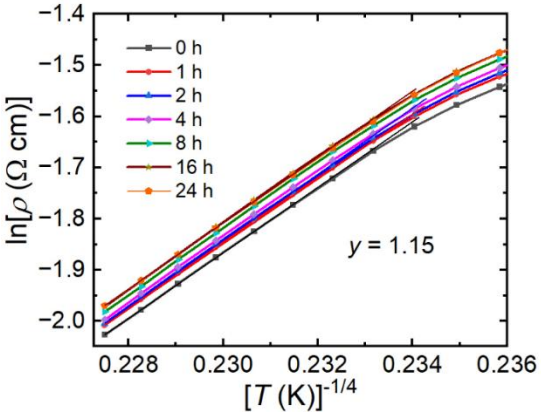


Figure 3.2.6 Plots of ln ρ versus $T^{-1/4}$ for the y = 1.15 sample after different total annealing times at 100 °C.

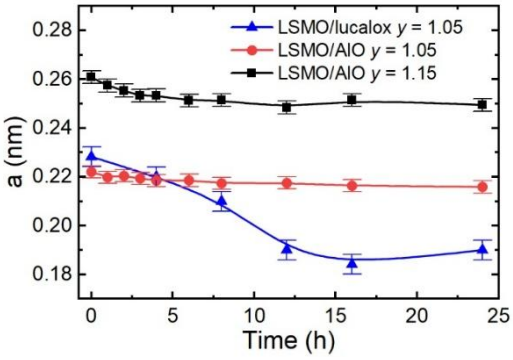


Figure 3.2.7 Change in localisation length during annealing of LSMO samples with y = 1.05 and y = 1.15.

3.2.3 Influence of ageing on magnetoresistance

The magnetoresistance response was analysed in both low and high magnetic fields. Low-field measurements up to 0.7 T were performed at 80 K and 300 K with the magnetic field applied either parallel or perpendicular to the film plane (see Figure 3.2.8). At 80 K (Figure 3.2.8a), the *MR*(*B*) curves showed the typical low-field magnetoresistance and hysteresis characteristic of polycrystalline manganite films. This behaviour originates from spin-polarised tunnelling across grain boundaries. The perpendicular-field geometry (Figure 3.2.8b) produced a more pronounced hysteresis because of the demagnetisation effect in thin films. The difference in *MR* for films with

different Mn concentrations was caused by the difference in the maximum resistance temperature T_m, which was higher for the films with $y = 1.15$.

The essential result is that accelerated ageing produced only small changes in the *MR* curves. Although resistivity increased after 24 h annealing, the magnetic-field-induced relative change in resistivity remained nearly unchanged. This means that ageing alters the absolute resistance of grain-boundary barriers but does not strongly modify the magnetic-field-induced spin alignment responsible for magnetoresistance and has a weaker influence on the long-range interaction between the crystallites.

Only insignificant changes after treatment of the Al_2O_3//LSMO films at 100 °C were also observed at room temperature (see Figure 3.2.8c, d).

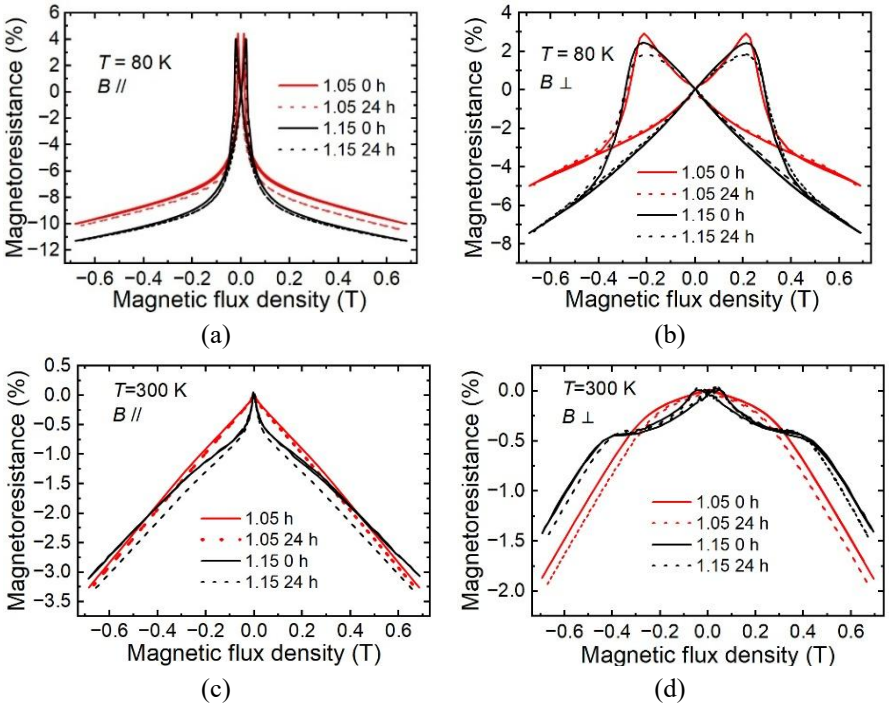
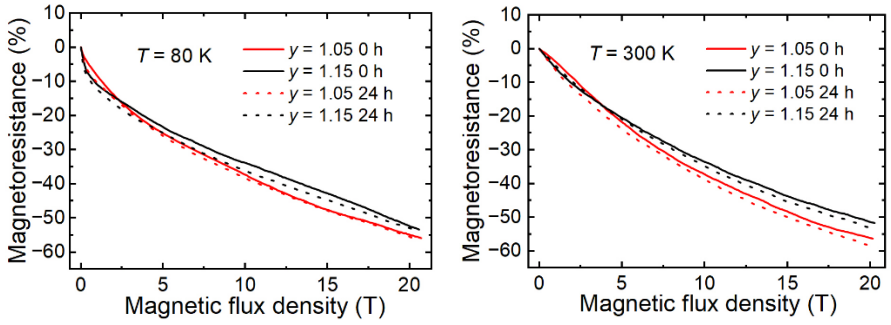


Figure 3.2.8 Low-field magnetoresistance versus magnetic flux density for Al_2O_3//LSMO films with $y = 1.05$ and $y = 1.15$ before and after 24 h of ageing: (a) 80 K, *B* parallel to the film plane; (b) 80 K, *B* perpendicular to the film plane; (c) 300 K, *B* parallel to the film plane; (d) 300 K, *B* perpendicular to the film plane.

High-field measurements up to 20 T further confirmed the stability of the magnetoresistive response (Figure 3.2.9). For both compositions and at temperatures of 80 K and 300 K, the change in magnetoresistance after accelerated ageing remained below approximately 1%. This behaviour is explained by the double-exchange mechanism. Oxygen depletion in grain boundaries reduces the number of active $Mn^{3+} - O - Mn^{4+}$ hopping centres

and increases the resistivity, but the ratio $\rho(B)/\rho(0)$ remains almost unchanged because the magnetic-field-induced alignment of Mn spins is preserved.

Therefore, the accelerated ageing procedure stabilises the transport response without degrading the high-field *MR* characteristics. This result is important for pulsed magnetic-field sensors, where stable calibration and reproducible magnetoresistance values are required under repeated measurements.



(a) (b)

Figure 3.2.9 High-field MR versus B dependences of Al_2O_3//LSMO films with $y = 1.05$ and $y = 1.15$ before and after accelerated ageing: (a) 80 K; (b) 300 K.

3.3 Magnetoresistive properties of lanthanum manganite-graphene nanostructures

This subchapter examines the magnetoresistive properties of a hybrid manganite-graphene nanostructure and the magnetic sensor developed from it. The results demonstrate that the magnetic-field magnitude and direction can be determined by measuring the sensor-system output voltages and processing them with a dedicated algorithm [P3].

3.3.1 Characterisation of graphene

To verify the quality of the graphene, we conducted Raman spectroscopy after transferring the graphene onto the Al_2O_3 protective layer. Figure 3.3.1 presents the average Raman spectrum of pristine graphene. The Raman spectrum exhibits the characteristic C–C stretching mode (G) at 1589 cm^{-1}, a low-intensity, narrow D-band at 1349 cm^{-1}, which is attributed to defects in the graphene structure, and the second-order resonance Raman scattering mode (2D) at 2684 cm^{-1}. The spectral parameters of graphene provide critical insights into its quality, doping level, and the number of layers. A key parameter in Raman spectroscopy for graphene is the intensity ratio of the 2D

and G bands (2D/G). In our measurements, the high 2D/G ratio of 2.5 indicates the presence of monolayer graphene, as multilayer graphene typically exhibits a lower 2D/G ratio due to changes in electronic band structure and interlayer interactions. Furthermore, the sharp and symmetric nature of the 2D peak, along with the negligible D-band intensity, confirms that the graphene is pristine, with minimal structural defects and high crystalline quality. These results demonstrate that the transfer process effectively preserved the integrity of the graphene layer and that its surface is cleaned from PMMA protection layer. Moreover, the high 2D/G ratio also indicates that an increase in the roughness of the protective Al_2O_3 layer (see Figure 3.3.1) did not degrade the quality of the graphene.

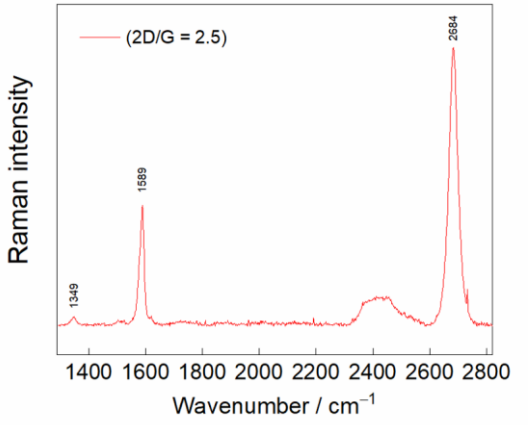


Figure 3.3.1 Raman spectrum of the graphene.

3.3.2 Characterisation of LSMO manganite film

The nanostructure of the LSMO film was examined using transmission electron microscopy (TEM; Tecnai G2 F20X-TWIN) equipped with an energy-dispersive X-ray spectrometer (EDAX). Atomic force microscopy (AFM) was also used to characterise the film surface before and after deposition of the protective Al_2O_3 layer. The low-magnification cross-sectional TEM image in Figure 3.3.2a shows columns extending through the film thickness, with their long axes perpendicular to the substrate. Some columns terminate below the surface, where neighbouring columns continue to grow. Typical column widths are approximately 50–70 nm near the upper surface and 20–50 nm close to the substrate. The contrast of the columns that satisfy Bragg's condition (darker areas) indicates their perfect crystalline

structure. The high-resolution TEM image of the crystalline part of the film further confirms the quality of the crystallites and grain boundaries. Figure 3.3.2b shows the interface between two neighbouring crystallites. It can be seen that each column is monocrystalline and the width of the grain boundary between them is about 1 nm. As will be discussed below, such good crystallite quality makes it possible to minimise the anisotropy of the magnetoresistance of the manganite film in low magnetic fields, which results in increased accuracy of magnetic field measurements.

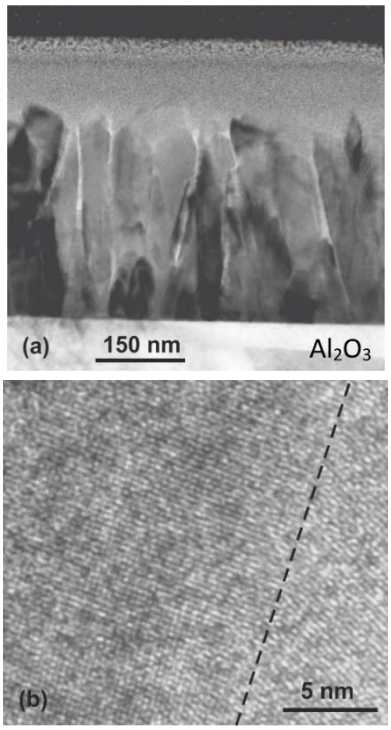


Figure 3.3.2 TEM image of LSMO film grown on Al_2O_3 substrate (a) and high-resolution TEM image of an interface between two adjacent crystallites of the film (b).

The surface of the grown manganite LSMO film was characterised using AFM. The characterisation was performed immediately after the film was grown and additionally after the deposition of the Al_2O_3 protective film on the top. It was important to determine how the surface topography (root-mean-square roughness R_q) could influence the quality of the transferred graphene. Figure 3.3.3 presents these results. Image (a) shows the surface 2D view of the as-grown LSMO film, while image (b) displays the surface 2D view of the Al_2O_3 protective film. It can be observed that the deposition of the protective film increases the R_q by approximately a factor of two: R_q=2.13 nm and R_q=5.16 nm, without and with Al_2O_3 protective layer. However, it remains

within the nanometre scale and does not affect the quality of the transferred graphene. This conclusion is supported by the Raman spectrum shown in Figure 3.3.1.

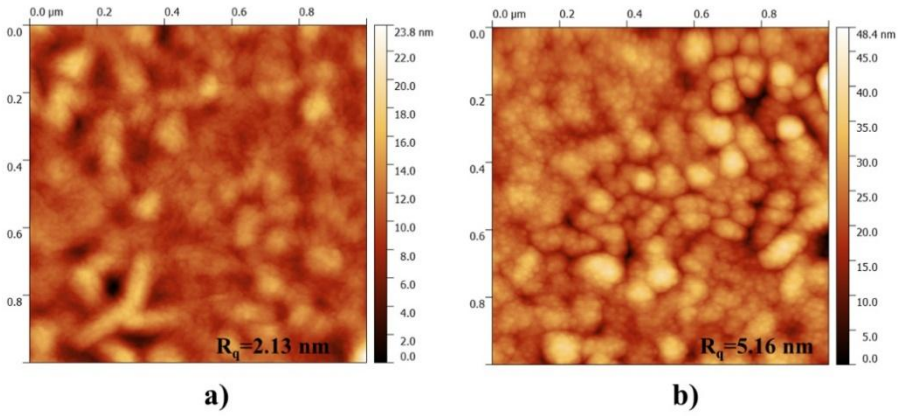


Figure 3.3.3 Manganite surface without a) and with b) Al_2O_3 layer characterisation using AFM.

3.3.3 Magnetoresistance of graphene

As already mentioned, the aim of this work is to develop a magnetic field sensor with which the absolute value of the magnetic flux density and the angle formed between the direction of the magnetic field and the sensor plane can be measured. A sensor based on manganite is used to measure the absolute value of the magnetic field and a sensor based on graphene is used to measure the angle.

The graphene sensor resistance depends on magnetic-field magnitude, temperature, and the angle between the field direction and the graphene plane. Figure 3.3.4a presents the field dependence of graphene magnetoresistance at four temperatures. The magnetoresistance was defined as follows:

$$MR_{Gr} = 100\% \times [R_{Gr}(B) - R_{Gr0}]/R_{Gr0}, \quad (3.3.1)$$

Here, $R_{Gr}(B)$ and R_{Gr0} denote the resistances in an applied magnetic field and at zero field, respectively. As shown in Figure 3.3.4a, the response is parabolic between zero and 1.5 T and becomes approximately linear at higher fields, as illustrated in the inset. Its temperature dependence is comparatively weak.

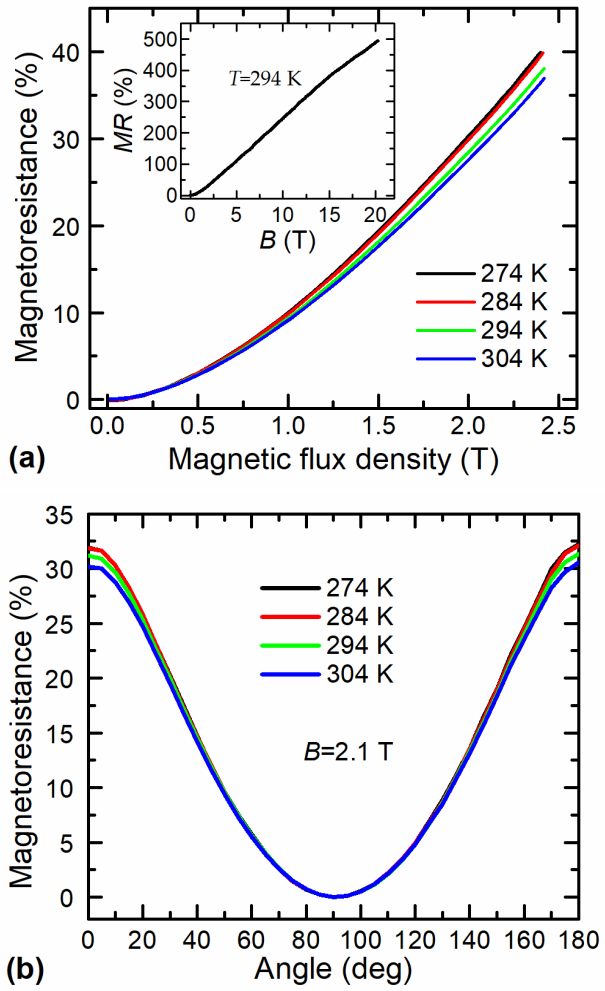


Figure 3.3.4 (a) Magnetoresistance of the graphene layer at different temperatures, when the magnetic flux density (B) is applied perpendicular to the plane of the layer. Inset – MR of graphene at B up to 21 T. (b) Magnetoresistance of the graphene layer at different angles (θ) between the magnetic field and the normal to the plane of the layer at 2.1 T and different temperatures.

The sensitivity of a graphene layer to a magnetic field (i.e. the change in resistance due to a magnetic field) depends on many parameters, e.g. the presence of defects in the layer, the number of layers, the amount of dopants and other parameters. One such parameter is the geometrical factor. The operation of a graphene sensor is based on the phenomenon of positive magnetoresistance induced by the Lorentz force (Gauss effect). However, the Hall voltage reduces this effect; therefore, for the measurement of magnetoresistance in general cases, the Corbino disc configuration must be used. Such a design, however, is not practical for device fabrication; thus, a

short and wide rectangular layer between the electrodes can be formed with the ratio $w/l >> 1$, where l and w are the distance between the electrodes and the width, respectively [113]. As has already been shown for graphene [114], this ratio has to be greater than 3. In our structure, it was $w/l=7$.

The second important characteristic for the measurement of the angle θ between the magnetic field and the normal to sensor's plane is the dependence of the resistance change on this angle. Graphene is an ideal material from this point of view, because if the magnetic field is directed parallel to the surface (θ=90°.) of the graphene layer, the change in resistance is zero. Figure 3.3.4b shows the magnetoresistance of the graphene layer at different angles θ at 2.1 T and different temperatures. This dependence was used to determine the angle from the normal to the surface of the sensor's plane.

3.3.4 Magnetoresistance of manganite

$La_{1-x}Sr_xMn_yO_3$ manganite films with Mn excess were used in the proposed hybrid sensor for measuring the absolute value of the magnetic field. As was previously shown in Section 3.1, the magnitude of magnetoresistance depends on the chemical composition of the film. It was demonstrated that the magnetoresistance can be increased by increasing the Mn/(La+Sr) ratio up to $y \approx 1.15$. Therefore, films with a Mn excess of $y \geq 1.15$ have to be chosen. The films grown for hybrid manganite-graphene structure had the following chemical composition measured by ICP-MS: $La_{0.9}Sr_{0.1}Mn_{1.2}O_3$. Magnetoresistance and its anisotropy of manganite film are shown in Figure 3.3.5a. Figure 3.3.5a also presents low-field *MR* of graphene. Figure 3.3.5b shows the dependence of manganite *MR* on the applied magnetic field at different temperatures when a DC magnetic field was applied up to 2.4 T parallel (solid line) and perpendicular (dashed line) to the film plane. As can be seen, an increase in temperature leads to a decrease in magnetoresistance. In addition, the magnetoresistance is lower when the magnetic field is perpendicular to the surface of the film than when it is parallel. Detailed results are presented in the inset in this figure and show the absolute change in *MR* due to the angle between the field and the normal vector to the surface of the film:

$$\Delta MR[\%] = |MR(\theta) - MR(0°)| \quad (3.3.2)$$

As one can see, this change is relatively small, amounting to less than 1%. Therefore, the error in measuring the value of the magnetic field is also small (less than 2.5 %) and decreases with increasing magnetic field strength, as can be seen from Figure 3.3.5c.

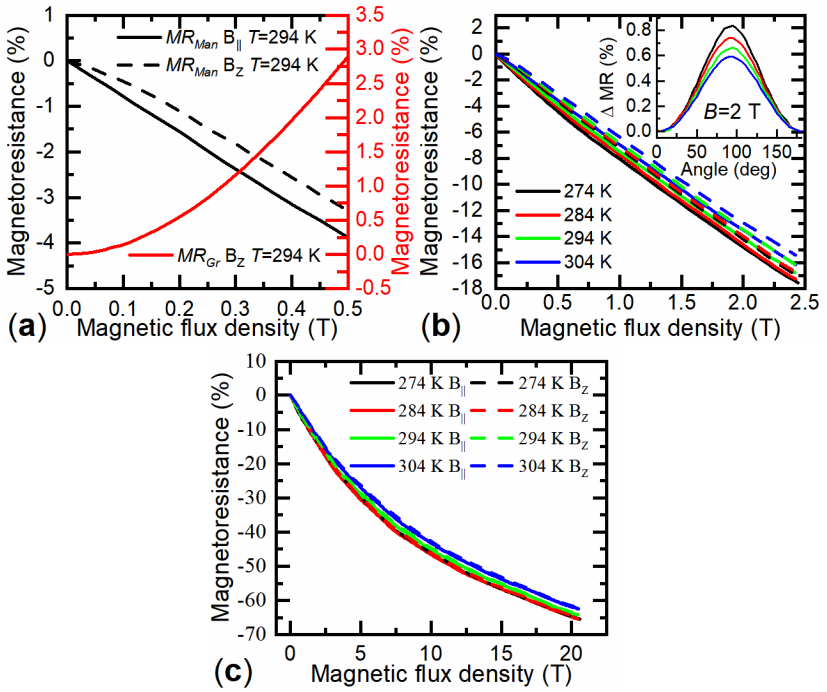


Figure 3.3.5 (a) Room temperature low-field *MR* of the graphene and the manganite sensors. (b) The manganite *MR vs*. magnetic field dependence at different temperatures when a magnetic field was applied parallel (solid line) and perpendicular (dashed line) to the film plane. Inset: *MR* dependence *vs*. angle between the magnetic field and the normal vector to the surface of the film. (c) The *MR vs*. magnetic field dependence of manganite at different temperatures, when a magnetic field was applied parallel and perpendicular to the film plane.

3.3.5 Design and fabrication of a hybrid lanthanum manganite-graphene sensor

The results were used to develop the hybrid manganite-graphene sensor shown in Figures 3.3.6a and 3.3.6b. It contains two sensing elements – a $La_{0.9}Sr_{0.1}Mn_{1.2}O_3$ manganite film and a graphene layer – on a 250 μm thick polycrystalline Al_2O_3 substrate. The LSMO-graphene hybrid sensor was fabricated in several steps. First, an LSMO film was deposited onto an Al_2O_3 substrate using the PI MOCVD method. Silver electrodes were then formed by photolithography and silver deposition. The spacing between these electrodes defined the active resistance-sensing region of the LSMO sensor. Next, an Al_2O_3 insulating layer was deposited to partially cover the LSMO film and its electrodes, preventing the subsequently deposited graphene layer from direct electrical contact with the LSMO film and its contacts. A graphene monolayer was then transferred onto the insulating layer, followed by the

formation of silver electrodes on the top. One of the graphene contacts was electrically connected to one of the LSMO contacts, thereby forming a common contact for the two sensing elements. The elements form a voltage divider supplied by a constant voltage of 0.5 V, as shown in Figure 3.3.6c. The circuit current (I) and voltage across the manganite element (V_{Man}) were measured, allowing the resistance changes of the two elements to be measured separately. As demonstrated by Lukose et al. [9], connecting negative-MR manganite and positive-MR graphene elements in series under a constant supply voltage can increase the hybrid sensor's sensitivity by several times.

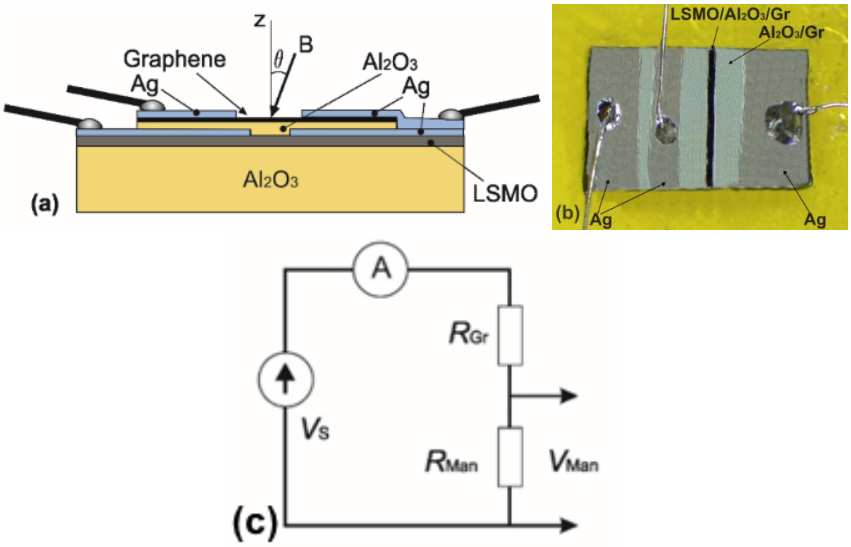


Figure 3.3.6 The schematic drawing (a), top view (b) and electrical circuit (c) of the hybrid sensor. R_{Gr} represents the resistance of the graphene layer, while R_{Man} represents the resistance of the LSMO manganite film.

3.3.6 Testing results of hybrid sensor

The sensor was tested using magnetic-field pulses with a duration of 1 ms and amplitudes up to 21 T (Figure 3.3.7a). The pulses were generated by discharging a capacitor bank through a coil in a non-destructive pulsed magnet, as described in Chapter 3. The sensor chip was tilted to vary the angle between the field and the sensor. Figures 3.3.7b and 3.3.7c show the resulting changes in circuit current and the voltages across the manganite film (solid line) and graphene layer (dashed line).

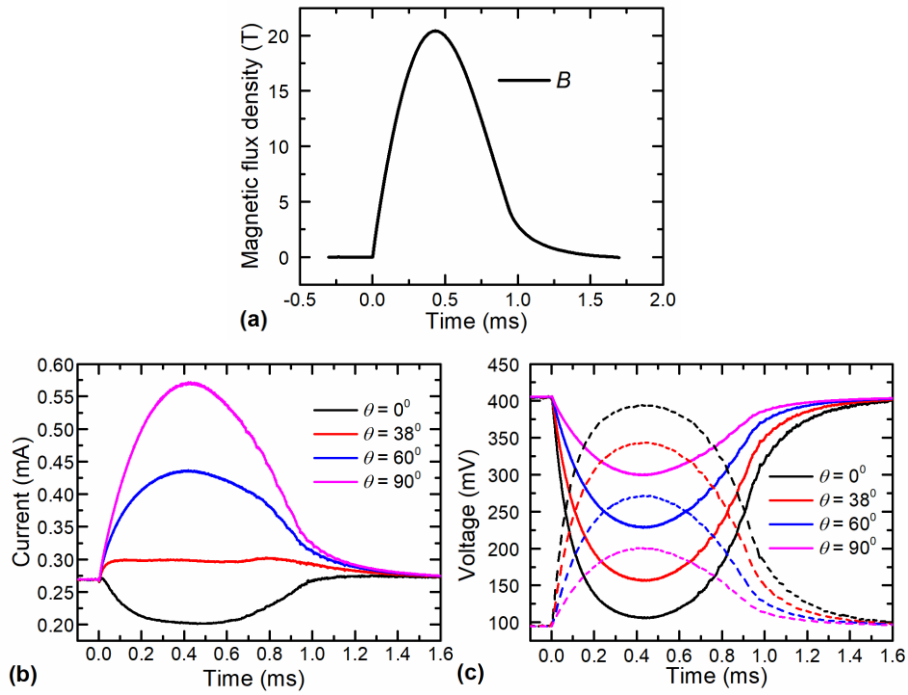


Figure 3.3.7 (a) Pulse of the magnetic field. (b) Change of current in the circuit in the pulsed magnetic field, when the hybrid sensor is tilted to different angles between the direction of the magnetic field and the normal of the sensor plane. (c) Voltage drop across the manganite (solid lines) and graphene (dashed lines) at different angles.

The zero-field resistances of the manganite and graphene elements were 1.5 kΩ and 0.35 kΩ, respectively. Their opposite magnetoresistive responses produce different current variations depending on the sensor orientation. When the field is aligned with the normal to the sensor plane, $\theta = 0°$, the circuit current decreases as the field increases (Figure 3.3.7b). At angles of 38° and above, the reduction in manganite resistance outweighs the increase in graphene resistance, causing the current to rise. With the field parallel to the sensor surface, graphene contributes no magnetoresistive resistance change, and the current variation is governed by the manganite element alone. Figure 3.3.7c shows that the field-induced increase in graphene resistance enhances the voltage response across the manganite film. The resulting sensitivity is highest when the field is perpendicular to the graphene plane, $\theta = 0°$, and lowest when it is parallel to that plane, $\theta = 90°$.

It should also be noted that when the direction of the magnetic field is known, we can adjust the initial resistance ratio of the manganite and graphene layers to achieve the maximum voltage change along the manganite film in the desired magnetic field. This is the case when, in a given magnetic field,

the resistance of the manganite is equal to that of the graphene. In our experiment, for example, when the magnetic field is perpendicular to the sensor's surface the largest voltage change occurs at a magnetic field of $B = 6$ T (0.06 ms after the start of the pulse).

Generally, combining two magnetoresistive sensors in a potentiometric circuit with a constant voltage source leads to a current $I(B)$ flowing in the circuit that is equal to:

$$I(B) = \frac{V_S}{R_1(B)+R_2(B)}. \tag{3.3.3}$$

Here V_s is the source voltage and $R_1(B)$ and $R_2(B)$ are magnetic field dependent resistances (in the current case R_1 and R_2 would be the resistances of the manganite R_{Man} and graphene R_{Gr} films, respectively). Expressing these resistances in a standardised form:

$$R_1(B) = R_{10}\big(1 + MR_1(B)\big) = R_{10}f_1(B), \tag{3.3.4}$$

$$R_2(B) = R_{20}\big(1 + MR_2(B)\big) = R_{20}f_2(B), \tag{3.3.5}$$

where R_{10} and R_{20} are zero-field resistances and MR_1 and MR_2 are magnetoresistances defined in fractional form, not percentage as in Equation (3.3.1), an expression for normalised middle node voltage V_{mid} between the magnetoresistors R_1 and R_2 can be written as:

$$\frac{V_{mid}}{V_S} = \frac{1}{1+k\zeta(B)}, \tag{3.3.6}$$

where $k=R_{20}/R_{10}$ and $\zeta(B)=f_2(B)/f_1(B)$. In our case $V_{mid} = V_{Man}$ (see Figure 3.3.6b). The sensitivity is defined as a derivative of the normalised midpoint voltage with respect to magnetic field and in this case is equal to:

$$S(B) = \left|\frac{d}{dB}\left(\frac{V_{mid}}{V_S}\right)\right| = \left|-\frac{k\zeta'(B)}{(k\zeta(B)+1)^2}\right|. \tag{3.3.7}$$

This equation shows a clear dependence of sensitivity on k. This dependence is not monotonic and has an extremum at:

$$k = \frac{1}{\zeta(B)} = \frac{f_1(B)}{f_2(B)}. \tag{3.3.8}$$

This shows that the sensor's sensitivity can be optimised for a chosen magnetic flux density by choosing the zero-field resistances of the sensors so that their ratio matches the magnetoresistance ratio at the chosen field. Determining the peak sensitivity, however, requires knowing $\zeta(B)$ and can be found by solving:

$$\frac{2k^2\big(\zeta'(B)\big)^2}{(k\zeta(B)+1)^3} - \frac{k\zeta'\prime(B)}{(k\zeta(B)+1)^2} = 0 \tag{3.3.9}$$

with respect to B. The initial resistance ratio of the manganite and graphene layers can be chosen to achieve the maximum possible voltage sensitivity along the manganite film in the desired magnetic field. Figure 3.3.8 shows the calculated midpoint voltage sensitivities (absolute values) for different initial

resistance ratios if experimental $f_1(B)$ and $f_2(B)$ are maintained. As can be seen from the figure, changing the value of k shifts the sensitivity curves. In the experimental case for the present graphene-manganite sensor, k was approximately R_{Gr}/R_{Man} =0.23. With this value, the sensitivity is maximised at ~6 T; however, the global peak sensitivity of ~60 mV/(V·T) was observed in the range of 0.9–2.5 T for the hybrid sensor, which is comparable with Si-based Hall sensors (~100 mV/(V·T)) [115].

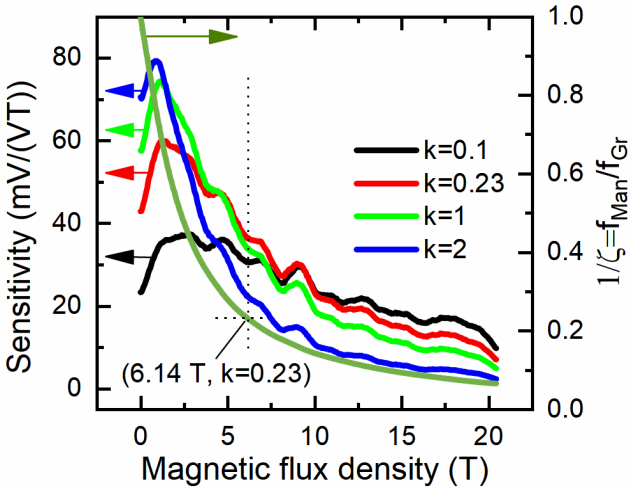


Figure 3.3.8 Calculated sensor's sensitivity curves at different initial resistance ratios and the experimental ratio between normalised resistance changes of manganite and graphene films.

The results provide the basis for a measurement device that determines magnetic-field magnitude and orientation relative to the sensor plane. The electronic system supplies the sensor, measures the voltage across the manganite film, and transfers the acquired data to a personal computer (PC). It follows the design reported in [11], providing 16-bit resolution and a sampling rate of 12.5 MS/s. The system was adapted by reducing the supply voltage and adding a measurement of the sensor-circuit current. Its software comprises firmware running in the measurement module and a control program on the PC. The firmware manages signal sampling, data storage, and transfer to the PC through the implemented communication protocol. Data acquisition accounts for three quantities: the initial manganite voltage, V_{0Man}, the time-dependent manganite voltage, $V_{Man}(t)$, and the circuit current, $I(t)$. V_{0Man} is proportional to the zero-field sensor resistance and therefore depends on temperature; it is treated as constant during an individual magnetic-field pulse. The field-dependent voltage across the manganite film, V_{Man} = f(|B|), reflects its magnetoresistive response.

Calibration is required because the resistances of both sensing elements depend nonlinearly on magnetic flux density, B, and also vary with temperature. The calibration establishes the relationship between the field-induced resistance change, ΔR, and the corresponding field magnitude. Orientation must also be considered for graphene and for the manganite film at low fields. Using the high-field generator described in Chapter 3, calibration curves were obtained at different temperatures and stored on the PC. Graphene was calibrated with the field perpendicular to the layer, whereas manganite was calibrated for both perpendicular and parallel field orientations. Examples of the resulting $R_{\mathrm{Gr}}(B)$ and $R_{\mathrm{Man}}(B)$ curves are presented in Figure 3.3.9a. For static or slowly varying fields, temperature changes must be measured independently so that their influence can be accounted for. A temperature sensor could be incorporated into the device while maintaining a compact design.

Figure 3.3.9b illustrates a simplified procedure for determining the magnitude and orientation of a magnetic field. In this regime, the low-field anisotropy of manganite magnetoresistance can be neglected, allowing the manganite response to determine the field magnitude, $|B|$. The graphene response depends on the component normal to the sensor's plane, denoted B_z. These quantities are related by $B_z = |B|\cos\theta$, where θ is the angle between the field and the sensor normal. The measured manganite resistance is therefore used to obtain $|B|$, while the graphene resistance provides B_z through its calibration. Combining these measurements yields both the field magnitude and its angle relative to the normal.

Figure 3.3.9b shows the measured voltages across the LSMO and graphene sensors, together with the corresponding changes in the current flowing through both sensing elements, during exposure to a pulsed magnetic field. The surface of the hybrid sensor was oriented at an angle of 50° to the magnetic field direction. The procedure for determining the magnetic field magnitude and the angle between the sensor's surface and the magnetic field direction is illustrated in this figure. For example, the measurements obtained at time instance t_1 indicate a magnetic field magnitude of 15 T and the normal component 9.4 T giving an angle θ of 51°. A series of experiments showed that the angular measurement accuracy was approximately ±2°. These calculations are performed for the entire pulse and displayed on the computer screen.

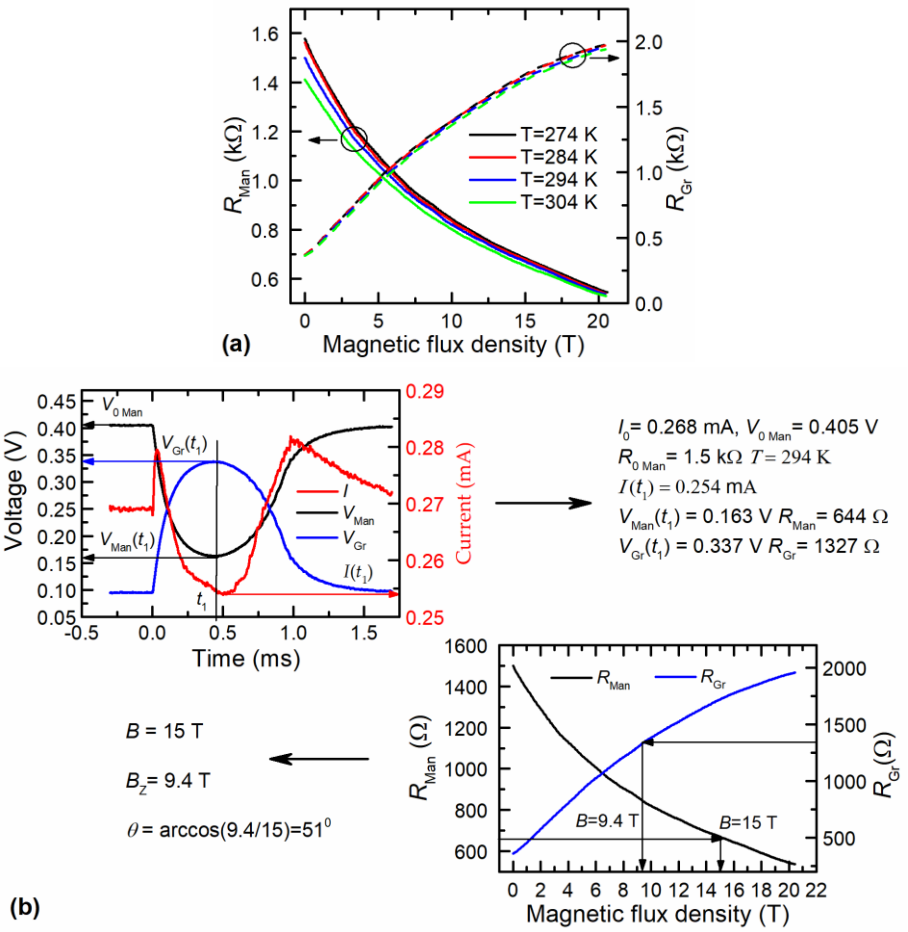


Figure 3.3.9 (a) A family of manganite (left scale) and graphene (right scale) calibration curves $R(B)$ at different temperatures. The same colour of solid and dashed curves corresponds to the same temperature. (b) Example of the procedure for measuring the magnitude and angle of the magnetic field.

The complete data-processing procedure also accounts for manganite magnetoresistance anisotropy. This correction is particularly important at low fields, where the angular variation represents a substantial fraction of the total magnetoresistive response (Figure 3.3.5a). During calibration, the manganite resistance was measured over a range of fields and temperatures for both parallel and perpendicular field orientations, and these dependences were stored on the PC. Graphene was calibrated with the field normal to its surface because its response is determined by B_z. The angular dependence of manganite resistance can then be represented by the following empirical expression:

$$R_{Man}(|B|,\theta) = R_{Man\parallel}(|B|) - \left(R_{Man\parallel}(|B|) - R_{Man\perp}(|B|)\right)\cos^2\theta \qquad (3.3.10)$$

Since $\cos(\theta)=B_z/|B|$ and B_z can be directly obtained from the resistance measurement of the graphene sensor, the $R_{\mathrm{Man}}(|B|, \theta)$ becomes $R_{\mathrm{Man}}(|B|)$. The absolute magnetic flux density can then be found by numerically solving for $|B|$. When using this algorithm, the accuracy of the measurement of the magnitude of the magnetic field and the angle depends only on the calibration accuracy of the individual sensor elements and the precision of the voltage and current measurements in the circuit, with minimal dependence on the anisotropy of the magnetoresistance of the manganite films. With the current measurement system, the sensor can measure both the absolute value and direction of B when B>30 mT. However, if the field direction is known and the sensor can be positioned accordingly, then the sensitivity of the hybrid sensor at low fields is increased due to the manganite film, and one can use the sensor from B>5 mT. These experiments showed similar accuracy of ±2° as in the case of high-field, which example is presented in Figure 3.3.9b.

The developed hybrid manganite-graphene sensor combines magnetic-field magnitude and direction measurements with increased sensitivity. The negative magnetoresistance of manganite and positive magnetoresistance of graphene improve the response over a broad range of fields and angles. Optimisation of the electrode spacing and layer dimensions increases magnetoresistance and sensitivity, particularly when the field is perpendicular to the sensor surface. The integrated acquisition system processes the outputs in real time to determine the field magnitude and orientation. These results support the use of the hybrid structure in applications requiring reliable measurements over wide magnetic-field and operating-temperature ranges.

GENERAL CONCLUSIONS

1. The Sr content in the range $0.05 \leq x \leq 0.3$ and the Mn ratio $y = \mathrm{Mn}/(\mathrm{La} + \mathrm{Sr}) > 1$ strongly influence the transport and magnetic properties of nonstoichiometric $La_{1-x}Sr_xMn_yO_3$ films:

1.1 The metal-insulator transition temperature T_m reaches its maximum at $x = 0.15$–0.18 for films with $y = 1.05$. Increasing Mn excess to $y = 1.15$ shifts this maximum towards lower Sr content, $x = 0.10$–0.17. This shift may be associated with La vacancies induced by Mn excess, which increase the Mn^{4+}/Mn^{3+} ratio and enhance ferromagnetic behaviour.

1.2 Films with $x = 0.3$ and $y = 1.15$ exhibit enhanced low-field magnetoresistance ranging from −1.23% to −0.8% over 250–290 K at $B = 50$ mT. This response may be explained by spin-polarized tunnelling through thin grain boundaries between crystallites of high structural quality. The high *Curie* temperature ($T_C = 383$ K) and saturation magnetization ($M = 870$ emu/cm³) support the presence of a saturated ferromagnetic state even at room temperature.

2. Nonstoichiometric $La_{1-x}Sr_xMn_yO_3$ films with $x = 0.3$ and $y = 1.15$, grown on polycrystalline Al_2O_3 substrates, could be used to develop sensors with predetermined characteristics for weak magnetic-field measurements (< 1 T) at room temperature. Films with $x = 0.1$–0.2 and $y > 1.1$ are preferable for high-field measurements.

3. Accelerated thermal ageing in argon at approximately 100 °C for 20 hours stabilises the resistance and magnetoresistance of nonstoichiometric $La_{1-x}Sr_xMn_yO_3$ films within 5 % for longer times (tested after 6 months), regardless of further increase in resistance during longer thermal treatment.

4. The accompanying increase in resistivity during thermal treatment can be described by hierarchically limited relaxation dynamics with a stretched-exponential time dependence characteristic of topologically disordered systems. The ageing behaviour is more likely associated with oxygen depletion and diffusion within grain boundaries than with nonstoichiometric disorder of the crystallites caused by Mn excess.

5. The design of hybrid nonstoichiometric manganite-graphene structure $Al_2O_3//La_{1-x}Sr_xMn_yO_3/Al_2O_3$ Graphene in which graphene is transferred on the top of manganite film using protective Al_2O_3 layer allows to minimize the dimensions of the active manganite-graphene sensing area enabling simultaneous local measurements of magnetic field magnitude and direction.

6. Connecting the single elements of the hybrid structure in a manganite-graphene voltage divider, the magnetic field at which the sensitivity is the highest is set by the ratio of the zero-field resistances of the two elements, $k = R_{Gr}/R_{Man}$, and the sensor can be tuned to a chosen field range by selecting this ratio. A hybrid structure of manganite $La_{0.9}Sr_{0.1}Mn_{1.2}O_3$ and graphene with $k = 0.23$ reached a peak sensitivity of about 60 mV/(V·T) at 0.9–2.5 T, comparable to Si-based Hall sensors.

SANTRAUKA

ĮVADAS

Darbo motyvacija ir problemos formulavimas

Tikslus magnetinių laukų matavimas bei jų krypties nustatymas yra labai svarbūs įvairiose taikymo srityse [1]. Tai apima magnetometriją, magnetinę duomenų atmintį, automatizavimą ir įvairias pramonės šakas, įskaitant automobilių pramonę. Šiuolaikinės technologijos reikalauja jutiklių, kurie būtų ne tik labai jautrūs, bet ir kompaktiški bei efektyviai veiktų plačiame temperatūrų intervale. Skirtingoms taikymo sritims keliami skirtingi jautrio, temperatūros ir magnetinio lauko verčių intervalų, tikslumo ir kitų parametrų reikalavimai. Komerciniai magnetorezistyviniai (MR) jutikliai, tokie kaip tunelinės magnetovaržos (TMR), gigantiškos magnetovaržos (GMR), anizotropinės magnetovaržos (AMR)ir kiti, pasižymi dideliu jautriu silpniems magnetiniams laukams (mažesniems nei 1 T) ir yra naudojami šio diapazono magnetiniams laukams matuoti [2]. Tačiau stipresniuose magnetiniuose laukuose jų atsakas pasiekia sotį, todėl šie jutikliai negali būti naudojami stiprių magnetinių laukų matavimams. Šis apribojimas yra ypač svarbus pažangioms magnetinių laukų generavimo sistemoms [3], kurios išplečia naudojamų magnetinių laukų diapazoną moksliniuose tyrimuose, pramonėje ir medicinoje. Šioms taikymo sritims reikalingi jutikliai, galintys matuoti magnetinius laukus plačiame intervale ir esant skirtingoms temperatūroms, kartu nustatant magnetinio lauko kryptį su galimybe stebėti jos pokyčius. Todėl medžiagų, pasižyminčių specifinėmis savybėmis, parinkimas ir efektyvių jutiklio elementų projektavimas yra labai svarbūs kuriant jutiklius, veikiančius plačiame magnetinio lauko diapazone [4].

Iš įvairių tiriamų medžiagų manganitai ir grafenas yra ypač perspektyvūs kandidatai dėl savo unikalių magnetinių savybių esant stipriems magnetiniams laukams [5, 6, 7, 8]. Naujausiame tyrime buvo pasiūlytas hibridinis jutiklis [9], sudarytas iš vienasluoksnio grafeno (SLG) ir plono, nanostruktūrizuoto $La_{0,8}Sr_{0,2}MnO_3$ (LSMO) manganito sluoksnio. Šiame jutiklyje SLG ir LSMO elementai buvo sujungti įtampos daliklio konfigūracijoje, išnaudojant du skirtingus šiose nanomedžiagose pasireiškiančius fizikinius efektus. Nanostruktūrizuoto manganito sluoksnis užaugintas ant polikristalinio padėklo, pasižymi neigiamu kolosaliosios magnetovaržos (CMR) efektu ir yra jautrus magnetiniams laukams plačiame temperatūrų (4–320 K) ir magnetinio lauko (nuo militeslų iki šimtų teslų) diapazone [10]. Šis efektas siejamas su dvigubos pamaininės sąveikos

mechanizmu, kai mangano jonų magnetiniai momentai išsirikiuoja išorinio magnetinio lauko kryptimi, dėl ko didėja sluoksnio laidumas. Be to, šie sluoksniai, esant stipriems magnetiniams laukams, yra santykinai nejautrūs magnetinio lauko krypčiai, todėl yra tinkami B-skalario jutiklių taikymams [11]. Taip pat ankstesni tyrimai parodė, kad nestechiometrinių lantano mangano $La_{1-x}Sr_xMn_yO_3$ sluoksnių, kuriuose mangano pertekliaus santykis y = Mn/(La+Sr) > 1, metalo-izoliatoriaus virsmo temperatūra T_m pasislenka į aukštesnes temperatūras, o savitosios varžos maksimumas sumažėja. Tai pagerina sluoksnių magnetovaržines savybes temperatūrose, aukštesnėse už kambario temperatūrą [12]. Tačiau nėra pakankamai tyrimų, įvertinančių nestechiometrinės cheminės sudėties įtaką sluoksnių savitosios varžos ir magnetovaržinių savybių stabilumui.

Iš kitos pusės, grafenas kaip dvimatis, nulinio energijų draudžiamojo tarpo pusmetalis, taip pat pasižymi dideliu potencialu magnetinių laukų matavimuose [8, 9]. Jis pasižymi itin dideliu krūvininkų judriu ir varžos pokyčiu magnetiniame lauke dėl teigiamos magnetovaržos, kurią sukelia Lorenco jėga. Taip pat buvo parodyta, kad dviejų jutiklių kombinacija, kai grafeno sluoksnis pasižymi didele teigiama magnetovarža, o nanostruktūrizuotas manganito-kobaltito (LSMCO) sluoksnis – neigiama kolosaliąja magnetovarža, leidžia reikšmingai padidinti jautrį, palyginus su atskirais grafeno ir LSMCO jutikliais [13]. Be to, priešingai nei nanostruktūrizuotas manganitas, kurio atsakas į magnetinio lauko kryptį dideliuose laukuose (didesniuose nei 0,5 T) yra izotropinis, grafeno magnetovarža stipriai priklauso nuo magnetinio lauko krypties. Todėl manganito ir grafeno magnetovaržinių savybių tyrimas bei jų optimizavimas, siekiant sukurti šiuolaikinius magnetinio lauko jutiklius, pasižyminčius platesnėmis taikymo galimybėmis, yra labai svarbus.

Darbo tikslas

Ištirti nestechiometrinių lantano manganito $La_{1-x}Sr_xMn_yO_3$ sluoksnių neigiamosios magnetovaržos ir grafeno teigiamosios magnetovaržos ypatumus bei sukurti kompaktišką hibridinį manganito-grafeno jutiklį, pasižymintį didesniu jautriu nei atskiri grafeno ar manganito jutikliai bei išplėsti jo funkcines galimybes, kurios leistų matuoti tiek magnetinio lauko stiprį, tiek ir jo kryptį jutiklio plokštumos atžvilgiu.

Darbo uždaviniai

1. Ištirti, kaip ant polikristalinio Al_2O_3 padėklo užaugintų nestechiometrinių $La_{1-x}Sr_xMn_yO_3$ sluoksnių cheminė sudėtis įtakoja jų magnetovaržą plačiame temperatūrų (5–300 K) ir magnetinių laukų (iki 20 T) ruožuose.
2. Ištirti pagreitinto terminio sendinimo įtaką nestechiometrinių $La_{1-x}Sr_xMn_yO_3$ sluoksnių savybėms ir nustatyti optimalias sąlygas, kurios galėtų būti naudojamos šių sluoksnių varžai ir magnetovaržai stabilizuoti.
3. Ištirti grafeno teigiamą magnetovaržą kambario temperatūroje, esant silpniems (0,1–2,4 T) ir stipriems (iki 20 T) magnetiniams laukams.
4. Suformuoti hibridinę nestechiometrinio lantano manganito-grafeno struktūrą ir ištirti, kaip manganito neigiama magnetovarža ir grafeno teigiama magnetovarža bei šių atskirų elementų pradinių (be magnetinio lauko) varžų santykis veikia hibridinės struktūros magnetovaržines savybes.
5. Sukurti stiprių impulsinių magnetinių laukų jutiklį, pagrįstą hibridine manganito-grafeno struktūra, gebantį matuoti magnetinio lauko stiprį ir kryptį jutiklio plokštumos atžvilgiu.

Mokslinis naujumas

- Ištirta cheminės sudėties įtaka nestechiometrinių $La_{1-x}Sr_xMn_yO_3$ sluoksnių, užaugintų ant polikristalinių Al_2O_3 padėklų metalo-izoliatoriaus virsmo temperatūrai ir magnetovaržai 5–300 K temperatūrų ir iki 20 T magnetinių laukų ruožuose bei nustatyti mechanizmai, lemiantys šias sluoksnių charakteristikas.
- Buvo nustatyti pagrindiniai mechanizmai, lemiantys nestechiometrinių $La_{1-x}Sr_xMn_yO_3$ sluoksnių pagreitintą terminį sendinimą 100 °C temperatūroje ir nustatytos optimalios sąlygos, galinčios stabilizuoti šių sluoksnių varžą ir magnetovaržą.
- Sukurta hibridinė nestechiometrinio lantano manganito-grafeno struktūra ir ištirtos jos magnetovaržinės savybės, siekiant sukurti hibridinį stiprių impulsinių magnetinių laukų jutiklį, gebantį išmatuoti magnetinio lauko vertę ir kryptį į jutiklio plokštumą.

Praktinė reikšmė

Sukurtas hibridinis lantano manganito-grafeno struktūra pagrįstas stiprių impulsinių magnetinių laukų jutiklis. Ištirtos ir optimizuotos jo savybės, siekiant matuoti tiek magnetinio lauko stiprį, tiek jo kryptį jutiklio plokštumos atžvilgiu. Šis naujas jutiklis yra svarbus didelės galios pramoniniams taikymams, kai magnetinio lauko kryptis nėra žinoma.

Ginamieji teiginiai

1. Nestechiometriniuose $La_{1-x}Sr_xMn_yO_3$ sluoksniuose ($y \geq 1{,}05$), užaugintuose ant polikristalinių Al_2O_3 padėklų, metalo-izoliatoriaus virsmo temperatūra pasiekia maksimumą ties x = 0,15–0,18 intervale $0{,}05 \leq x \leq 0{,}3$ (kai y = 1,05) ir gali būti dar padidinta, didinant Mn perteklių y. Padidinus y iki 1,15, kambario temperatūros silpno lauko magnetovarža padidėja du kartus, esant 50–100 mT magnetiniams laukams.
2. Pagreitintas terminis nestechiometrinių $La_{1-x}Sr_xMn_yO_3$ sluoksnių sendinimas argono atmosferoje 100 °C temperatūroje sukelia monotonišką kambario temperatūros varžos augimą, kuris atitinka ištemptosios eksponentės augimo dėsnį ir artėja prie soties po maždaug 20 valandų terminio kaitinimo. Ištemptosios eksponentės kinetika atitinka relaksaciją topologiškai netvarkiose sistemose ir identifikuoja deguonies išsiskyrimo bei persiskirstymo tarpkristalitinėse ribose procesą kaip pagrindinį sendinimo mechanizmą, o ne Mn pertekliaus sukeltą kristalinės gardelės iškraipymą. Šią interpretaciją taip pat patvirtina tai, kad magnetovarža per visą sendinimo procesą pakinta ne daugiau kaip 5%.
3. Hibridinė nestechiometrinio manganito-grafeno struktūra – Al_2O_3//$La_{1-x}Sr_xMn_yO_3$/Al_2O_3/grafenas, sujungta kaip įtampos daliklis, leidžia vienu metu išmatuoti išorinio magnetinio lauko stiprį ir kampą su jutiklio plokštuma. Magnetinių laukų ruožas, atitinkantis didžiausią hibridinio jutiklio jautrį, yra nulemtas atskirų grafeno ir manganito elementų pradinių (B=0) varžų santykio $k=R_{Gr}/R_{Man}$, kuris suteikia praktinę galimybę derinti jutiklį pasirinktai magnetinio lauko matavimo sričiai, šiame darbe pasiekiant didžiausią 60 mV/(V·T) jautrį 0,9–2,5 T magnetinio lauko ruože, kai k=0,23.

Autoriaus indėlis

Visi šioje disertacijoje pateikti rezultatai buvo gauti autoriui bendradarbiaujant su straipsnių bendraautoriais. Autorius atliko eksperimentų parengiamuosius darbus, vykdė LSMO ir grafeno sluoksnių magnetovaržinių bei krūvio pernašos savybių tyrimus visame temperatūrų ir magnetinių laukų ruože ir apdorojo gautus duomenis. Gautų rezultatų interpretaciją ir analizę autorius atliko kartu su moksline vadove ir straipsnių bendraautoriais.

Disertacijos struktūra

Disertaciją sudaro įvadas, trys pagrindiniai skyriai, bendrosios išvados, literatūros sąrašas ir autoriaus publikacijų sąrašas. Tris pagrindinius disertacijos skyrius sudaro: literatūros apžvalga; bandinių paruošimo ir matavimo įrangos aprašymas; gautų rezultatų pristatymas ir jų analizė.

1. LANTANO MANGANITŲ IR GRAFENO FIZIKINIŲ SAVYBIŲ APŽVALGA

Šiame skyriuje apžvelgiamos lantano perovskitų, ypač mangano pagrindu sudarytų junginių (manganitų), fizikinės savybės. Pristatomi magnetovaržos reiškiniai, ypatingą dėmesį skiriant kolosaliajai magnetovaržai ir jos taikymams. Taip pat yra aptariamos grafeno magnetinės savybės.

Skyrius baigiamas šio darbo motyvacija, atsižvelgiant į šiuolaikinius pasiekimus manganitų ir grafeno tyrimų srityse. Pabrėžiama, kad, nepaisant įvairių komercinių magnetinio lauko jutiklių, pagrįstų GMR, TMR ir AMR efektais, vis dar išlieka poreikis naujoms sistemoms, skirtoms vidutinio ir didelio stiprumo magnetiniams laukams matuoti. Pažangioms magnetinių laukų generavimo sistemoms reikalingi jutikliai, galintys matuoti magnetinius laukus plačiame stiprių laukų ruože ir esant skirtingoms temperatūroms, kartu nustatant šių laukų kryptį ir stebint jų pokyčius. Todėl specialiomis savybėmis pasižyminčių medžiagų parinkimas ir efektyvių jutiklio elementų projektavimas yra labai svarbūs.

Daug pastangų buvo skirta kolosalios magnetovaržos CMR jutiklių, pagrįstų stechiometrinės sudėties polikristaliniais $La_{1-x}Sr_xMn_yO_3$ sluoksniais, kūrimui. Tačiau, siekiant optimizuoti jų veikimą, būtina išsamiai ištirti, kaip cheminė sudėtis (x ir y) veikia jų magnetovaržines savybes ir stabilumą. Be to, poreikis atlikti lokalius magnetinio lauko ir jo krypties matavimus skatina ieškoti pažangių medžiagų arba jų hibridinių struktūrų su dvimačiais sluoksniais, pasižyminčiais naujomis funkcinėmis galimybėmis.

2. BANDINIŲ PARUOŠIMAS IR MATAVIMO METODIKA

2.1 Bandinių paruošimas ir jų charakterizavimas

Šiame poskyryje aprašomi šiame darbe tirtų bandinių paruošimo metodai ir jų charakterizavimo metodikos. LSMO sluoksniai buvo suformuoti siekiant ištirti jų individualias savybes bei panaudoti juos hibridinėms manganito-grafeno struktūroms formuoti. Grafeno sluoksnis buvo tiriamas po jo perkėlimo ant Al_2O_3 sluoksnio.

2.1.1 La-Sr-Mn-O sluoksnių nusodinimas PI MOCVD metodu

Lantano manganito $La_{1-x}Sr_xMn_yO_3$ (LSMO) sluoksniai, pasižymintys skirtinga Sr koncentracija (x) ir Mn pertekliumi (y), buvo nusodinami ant polikristalinių Al_2O_3 padėklų naudojant impulsinį-injekcinį metaloorganinių

junginių nusodinimo iš garų fazės (PI MOCVD) metodą. Sluoksnių augimo metu padėklo temperatūra buvo palaikoma T_{pad}=750 °C. Sluoksnių storis, nustatytas profilometru, siekė 350–360 nm.

Kaip pradinės medžiagos (prekursoriai) buvo naudojami toluene ištirpinti $La(thd)_3$, $Sr(thd)_2$ ir $Mn(thd)_3$ junginiai, kuriuose thd žymi 2,2,6,6-tetrametil-3,5-heptandionatą. Organinio tirpalo, kuriame buvo ištirpęs prekursorių mišinys, maždaug 3 mg masės mikrodozės į reakcijos zoną buvo įpurškiamos 2 Hz dažniu. Mikrodozių staigus išgarinimas buvo vykdomas ~270 °C temperatūroje. Susidaręs garų mišinys į reakcijos kamerą link įkaitinto padėklo buvo pernešamas ~95 l/h dujų srautu, sudarytu iš argono ir deguonies, kurių santykiu buvo 5:1. Visų tirtų LSMO sluoksnių augimo greitis buvo apie 28 nm/min.

Buvo suformuotos kelios LSMO sluoksnių grupės, pasižyminčios skirtingu Mn pertekliaus santykiu y = Mn/(La + Sr). Prekursorių tirpalo sudėtis buvo parinkta taip, kad Mn kiekis būtų pastovus (y = 1,05; 1,10; 1,15 ir 1,20), o Sr koncentracija būtų keičiama intervale x = 0,05–0,3.

Siekiant suformuoti grynos perovskitinės struktūros sluoksnius, nusodinimo sąlygos iš pradžių buvo optimizuojamos auginant LSMO sluoksnius ant monokristalinių $LaAlO_3$ (LAO) padėklų. Optimizavus nusodinimo parametrus, LSMO sluoksniai buvo formuojami ant polikristalinių Al_2O_3 padėklų. Be to, galutinio skirtingos cheminės sudėties LSMO sluoksnių formavimo metu buvo naudojami tiek Al_2O_3, tiek LAO padėklai, siekiant palyginti ant skirtingų padėklų suformuotų sluoksnių savybes.

Po nusodinimo LSMO sluoksniai buvo atkaitinami 750 °C temperatūroje 10 min gryno deguonies atmosferoje. Vėliau bandiniai buvo lėtai, maždaug 4,7 °C/min greičiu, atvėsinami iki 350 °C. Bandinių struktūriniai elementai buvo suformuoti naudojant fotolitografijos metodą. Elektrodams suformuoti termiškai buvo nusodinamas Cr pasluoksnis ir Ag kontaktinės aikštelės. Po elektrodų suformavimo buvo 1 valandą atliekamas papildomas atkaitinimas 450 °C temperatūroje Ar atmosferoje.

Kaip pateikta 2.1 lentelėje, tiriamieji bandiniai buvo suskirstyti į kelias grupes pagal jų paruošimo sąlygas ir tyrimų paskirtį.

1 grupės LSMO sluoksniai buvo formuojami palaikant pastovų Mn pertekliaus santykį ir keičiant Sr koncentraciją. 2 grupės sluoksniai buvo formuojami palaikant pastovią Sr koncentraciją ir keičiant Mn kiekį. 3 grupės sluoksnių cheminė sudėtis buvo parinkta siekiant padidinti hibridinės manganito-grafeno struktūros jutiklio darbinę temperatūrą iki 90 °C. Visais atvejais sluoksnių formavimo metu padėklo temperatūra buvo palaikoma vienoda.

2.1 Lentelė. Ištirtų polikristalinių LSMO bandinių grupės ir pagrindinės jų savybės.

	T_{pad}, °C	T_m, K	ρ_m, Ωcm	Sr/(La+Sr)	Mn/(La+Sr)
1 grupė	750	260	0,58	0,08	1,15
	750	270	0,27	0,18	1,15
	750	255	0,09	0,3	1,15
2 grupė	750	240	0,47	0,18	1,05
	750	255	0,37	0,18	1,1
	750	270	0,27	0,18	1,15
3 grupė	750	280	0,35	0,1	1,20

2.1.2 Grafeno perkėlimo procedūra

Vienasluoksnis grafenas buvo perkeltas naudojant šlapio pernešimo metodą. Šiam procesui buvo naudojamas komerciškai prieinamas aukštos kokybės vienasluoksnis grafenas, užaugintas ant varinės folijos ir padengtas poli(metilmetakrilato) (PMMA) sluoksniu.

Varinė folija buvo pašalinama ėsdinant ją amonio persulfato tirpalu. Po šio proceso ėsdinimo tirpalo paviršiuje susidaręs grafeno/PMMA sluoksnis laisvai plūduriavo tirpalo paviršiuje. Grafeno/PMMA sluoksnis kelis kartus buvo plaunamas dejonizuotu vandeniu ir perkeltas ant suformuoto Al_2O_3 sluoksnio.

PMMA sluoksnis, atlikęs atraminio ir apsauginio sluoksnio funkciją grafeno perkėlimo metu, buvo pašalintas nuo grafeno paviršiaus. Vėliau ant grafeno sluoksnio termiškai buvo suformuoti du elektrodai. Elektrodų geometrija buvo parinkta taip, kad vienas iš jų būtų bendras ir elektriškai sujungtas su vienu iš manganito elektrodų, o kitas būtų atskiras. Atstumas tarp elektrodų buvo 100 μm, o jų plotis – 0,7 mm.

2.1.3 Grafeno ir manganito struktūros charakterizavimas

Perkelto vienasluoksnio grafeno kokybei ir sluoksnių skaičiui įvertinti buvo taikoma Ramano spektroskopija. Ramano spektrai registruoti naudojant „InVia Raman“ mikroskopą („Renishaw“, JK), kuriame įrengtas termiškai aušinamas (−70 °C) CCD detektorius ir 532 nm bangos ilgio lazerio spinduliuotės šaltinis.

Matavimo žingsnis *x* ir *y* kryptimis buvo 4 × 4 μm. Kiekvieną matavimo žemėlapį sudarė 50 matavimo taškų, kuriuose spektrų kaupimo trukmė buvo 20 s. Lazerio spinduliuotės galia bandinio paviršiuje siekė 0,23 mW. Lazerio spindulys buvo fokusuojamas naudojant 50×/0,75 NA objektyvą („Leica“).

2D ir G juostų intensyvumų santykis (2D/G) buvo apskaičiuojamas naudojant „Wire 5.5“ programinę įrangą („Renishaw“, JK). Didelė 2D/G santykio vertė (2,9) patvirtino, kad tirtas grafenas buvo vienasluoksnis, nepažeistas ir pasižymėjo aukšta struktūrine kokybe.

LSMO sluoksnių nanostruktūrai ir cheminei sudėčiai charakterizuoti buvo taikomi keli eksperimentiniai metodai. Sluoksnių elementinei cheminei sudėčiai nustatyti naudota induktyviai susietos plazmos didelės skiriamosios gebos masių spektrometrija (ICP-MS). LSMO sluoksnių paviršiaus morfologija tirta skenuojančiuoju elektroniniu mikroskopu (SEM, „Hitachi SU70“). Kristalinei struktūrai ir elementinei sudėčiai lokaliose srityse nustatyti naudotas peršviečiamas elektroninis mikroskopas (TEM, „Tecnai G2F20 X-TWIN“) su energijos dispersijos rentgeno spindulių spektrometru (EDAX).

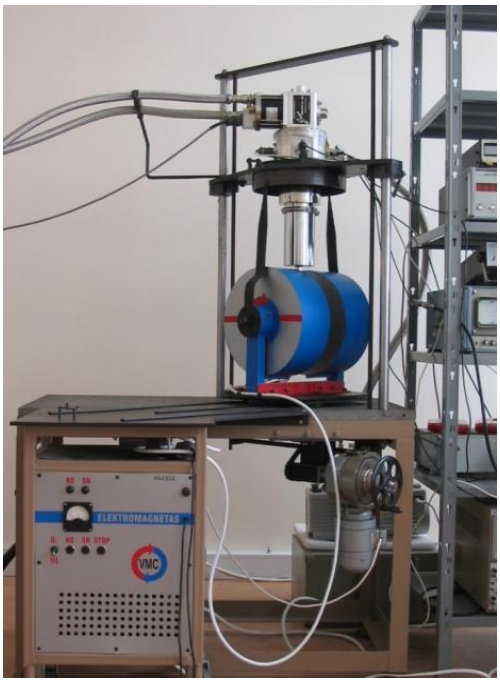
LSMO sluoksnių paviršiaus topografija taip pat buvo tiriama atominių jėgų mikroskopijos (AFM) metodu. Matavimai atlikti tiek LSMO sluoksniams be apsauginio Al_2O_3 sluoksnio, tiek juo padengtiems sluoksniams.

Magnetinės savybės buvo tiriamos iki 50 kOe stiprio magnetiniuose laukuose naudojant MPMS-5 SQUID („Quantum Design“) magnetometrą. Buvo registruojamos magnetinio momento priklausomybės nuo magnetinio lauko esant pasirinktoms temperatūroms. Magnetinės histerezės kilpos buvo matuojamos 1000 Oe stiprio magnetiniame lauke, temperatūrų intervale nuo 320 iki 220 K. Įmagnetėjimo matavimai buvo atlikti Lenkijos mokslų akademijos Fizikos institute.

2.2 Matavimo aparatūra ir metodai

2.2.1 Savitosios varžos ir silpno magnetinio lauko magnetovaržos matavimo sistema

Savitoji varža ir magnetovarža, esant silpno stiprio magnetiniams laukams, buvo matuojamos atitinkamai T = 5–310 K ir T = 25–300 K temperatūrų intervaluose, naudojant uždaro ciklo helio dujų kriogeninę sistemą („Janis 4K“) ir elektromagnetą (iki 0,8 T). Varža buvo matuojama dviejų kontaktų metodu, kurį galima buvo panaudoti dėl specialios sukurtos kontaktų su bifiliariškai susuktais laidais technologijos [6]. Pagrindinė matavimo sistema pavaizduota 2.2.1 pav.

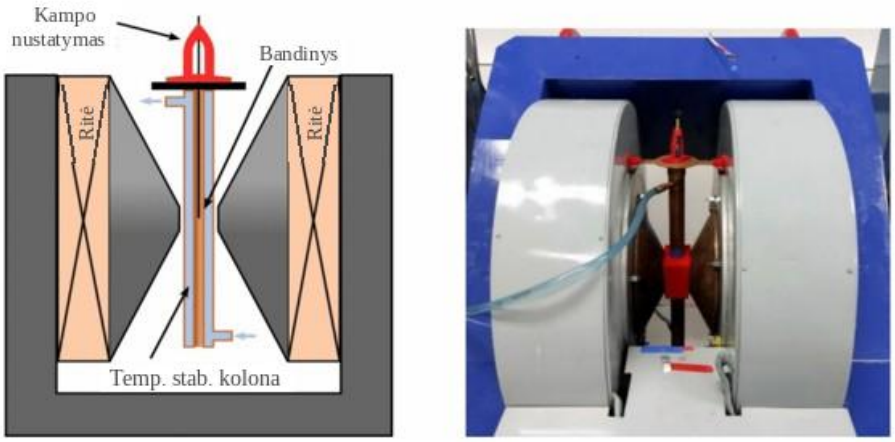


2.2.1 pav. Savitosios varžos ir silpno magnetinio lauko magnetovaržos matavimo sistema.

2.2.2 Magnetovaržos priklausomybės nuo magnetinio lauko krypties matavimo sistema

Magnetovarža buvo matuojama nuolatiniame magnetiniame lauke, kurį tarp magnetinio lauko koncentratoriaus polių generavo elektromagnetas, galintis sukurti iki 2,4 T stiprio magnetinį lauką. Eksperimentinė matavimo sistema pavaizduota 2.2.2 pav.

Bandinys buvo įtvirtintas temperatūros stabilizavimo kolonoje, kuri talpinama tarp elektromagneto polių. Pats bandinys buvo pritvirtintas prie strypo, kurį buvo galima rankiniu būdu sukti. Stabilizavus temperatūrą, buvo įjungiamas magnetinis laukas ir registruojamos varžos vertės, bandinį sukant nuo 0° iki 180°. Po to magnetinio lauko stipris buvo padidinamas ir matavimo procedūra pakartojama.

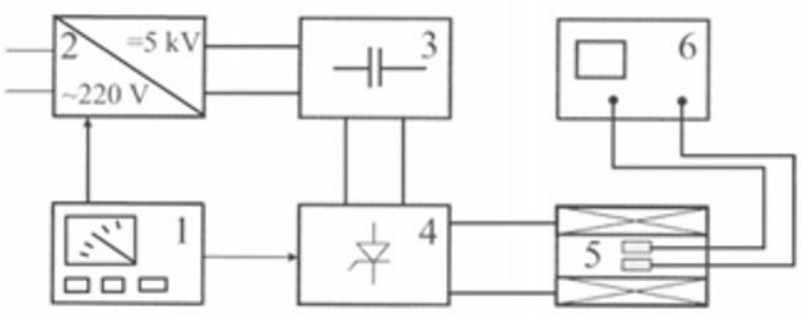


2.2.2 pav. Eksperimentinės matavimo sistemos schema (kairėje) ir vaizdas (dešinėje). Temperatūros stabilizavimo kolona, įrengta tarp elektromagneto polių. Kampo reguliavimo rankenėlė matoma kolonos viršuje.

2.2.3 Magnetovaržos matavimo sistema esant stipriems magnetiniams laukams

Magnetovarža stipriuose magnetiniuose laukuose buvo matuojama impulsiniuose, iki 20 T magnetiniuose laukuose, esant (80–363) K temperatūrai. Matavimams buvo naudojamas impulsinio magnetinio lauko generatorius, pagrįstas kondensatorių baterijos iškrova per ritę. Pagrindinė stipraus magnetinio lauko impulsų generatoriaus blokinė schema pateikta 2.2.3 pav.

Čia: 1 – įkrovimo ir iškrovimo valdymo įtaisas, 2 – kondensatorių baterijos įkrovimo įrenginys, 3 – kondensatorių baterija, 4 – didelės galios puslaidininkinis jungiklis, 5 – ritė, 6 – matavimo įrenginys.



2.2.3 pav. Stipraus magnetinio lauko generatoriaus blokinė schema.

3. REZULTATAI IR JŲ APTARIMAS

3.1 Nanostruktūrizuotų lantano manganito sluoksnių magnetovarža

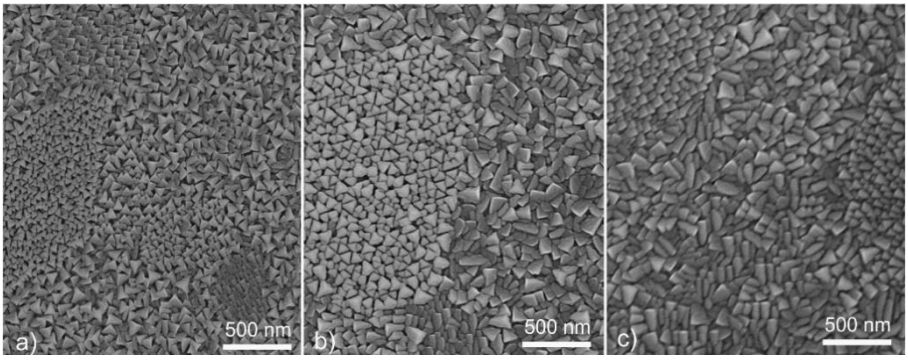
Šiame poskyryje pateikiami tyrimų rezultatai, parodantys, kaip ant polikristalinio Al_2O_3 padėklo užaugintų nestechiometrinių nanostruktūrizuotų $La_{1-x}Sr_xMn_yO_3$ sluoksnių cheminė sudėtis veikia jų magnetovaržos vertes plačiame temperatūrų (5–300 K) ir magnetinių laukų intervale [P1].

3.1.1 LSMO sluoksnių morfologija ir mikrostruktūra

LSMO sluoksnių, užaugintų esant skirtingam Sr kiekiui (x) ir pastoviam Mn pertekliaus kiekiui (y = 1,15), paviršiaus morfologijos SEM vaizdai pateikti 3.1.1 pav.

Kai x = 0,08 (3.1.1a pav.), paviršiuje daugiausia stebimi trikampio formos kristalitai, tačiau kai kuriose srityse matomos įvairaus dydžio ir formos kristalitų salelės. Tai siejama su polikristalinio Al_2O_3 padėklo paviršiaus kristalografinių plokštumų ir kristalitų dydžio įvairove. Kai kuriose padėklo srityse susidaro gerai orientuota trikampio formos kristalitų struktūra, o kitose kristalitai yra labiau atsitiktinai orientuoti.

Padidinus Sr kiekį iki x = 0,18 (3.1.1b pav.), greta trikampio formos kristalitų pradeda vyrauti pailgos stačiakampio formos kristalitai. Toliau didinant Sr kiekį iki x = 0,30 (3.1.1c pav.), būtent pailgos stačiakampio formos kristalitai tampa dominuojantys. Visuose bandiniuose taip pat išlieka mažesnių trikampio formos kristalitų salelės.

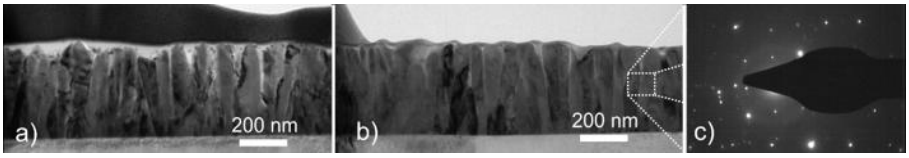


3.1.1 pav. LSMO sluoksnių paviršiaus SEM vaizdai, esant skirtingam Sr kiekiui (x) ir pastoviam Mn/(La + Sr) kiekiui (y = 1,15): (a) x = 0,08, (b) x = 0,18, (c) x = 0,30.

Vidutinis kristalitų dydis nuo Sr kiekio stipriai nepriklauso ir siekia apie 75, 80 ir 85 nm, atitinkamai esant x = 0,08, 0,18 ir 0,30. Stebimą kristalitų formos kitimą, didėjant Sr koncentracijai, galima sieti su kristalinės gardelės

deformacija ir (arba) kristalinės struktūros pokyčiais, lemiančiais skirtingą kristalitų orientaciją sluoksnio paviršiaus atžvilgiu.

Siekiant išsiaiškinti LSMO sluoksnių augimo ypatumus, buvo analizuojami TEM vaizdai. Mažo didinimo skerspjūvio TEM vaizdai, kai Sr kiekis x = 0,08 ir 0,18, pateikti atitinkamai 3.1.2a ir 3.1.2b pav. Sluoksnius sudaro vertikaliai orientuotos kolonos, kurių ilgoji ašis yra statmena padėklo paviršiui. Kolonų plotis viršutinėje sluoksnio dalyje siekia apie 60–75 nm, o prie padėklo – 30–50 nm. Kai x = 0,08, sluoksnio mikrostruktūra yra labai porėta, joje stebimos tarpkoloninės ir kolonų viduje esančios tuštumos bei ryškus dendritinis raštas. Kolonos sudarytos iš kelių monokristalinių blokų, tarp kurių susidaro mikrolaipteliai. Didėjant Sr kiekiui, struktūra tampa tankesnė ir taisyklingesnė: kristalitų šoniniai paviršiai ir jų ribos tampa lygūs, o atskiri kristalitai yra monokristaliniai, nors gali būti pasisukę padėklo plokštumos atžvilgiu. Tai patvirtina 3.1.2c pav. pateiktas kelių kristalitų difrakcijos vaizdas. Sluoksnių, kuriuose x = 0,30, mikrostruktūra yra panaši į sluoksnių, kuriuose x = 0,18.

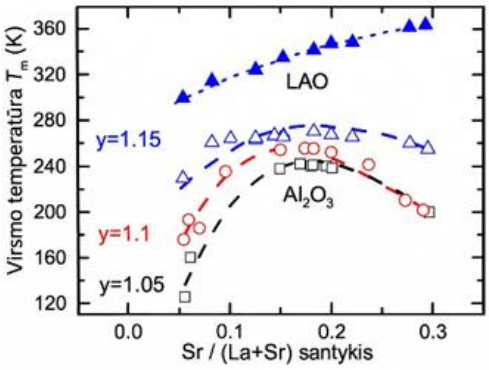


3.1.2 pav. LSMO sluoksnių TEM vaizdai, esant skirtingam Sr kiekiui (x) ir pastoviam Mn kiekiui (y = 1,15): (a) x = 0,08, (b) x = 0,18. (c) Atrinktosios srities elektronų difrakcijos vaizdas iš 3.1.2b pav. pažymėtos srities, kai Sr kiekis sluoksnyje x = 0,18.

3.1.2 Nanostruktūrizuotų LSMO sluoksnių savitosios varžos ir metalo-izoliatoriaus virsmo temperatūros priklausomybė nuo Sr kiekio ir Mn pertekliaus

Siekiant ištirti x = Sr/(La + Sr) ir y = Mn/(La + Sr) santykių kitimo įtaką metalo-izoliatoriaus virsmo temperatūros T_m vertei, buvo atlikti nanostruktūrizuotų LSMO sluoksnių savitosios varžos priklausomybės nuo temperatūros matavimai. Tyrimų rezultatai apibendrinti 3.1.3 pav.

Matome, kad didėjant Mn/(La + Sr) santykiui y, metalo-izoliatoriaus virsmo temperatūra Tm didėja, ypač esant mažesniam Sr kiekiui. Didėjant y, maksimumas Tm šiek tiek pasislenka mažesnių Sr koncentracijų link. Tai galima sieti su didesniu La vakansijų kiekiu, susidarančiu didėjant Mn pertekliui, ir dėl to didėjančiu Mn^{4+} kiekiu. Todėl tam pačiam Mn^{4+}/Mn^{3+} santykiui, kuris yra svarbus manganitų elektrinėms krūvio pernašos savybėms, pasiekti reikia mažesnio Sr kiekio [101].



3.1.3 pav. Nanostruktūrizuotų Al_2O_3//LSMO ir epitaksinių LAO//LSMO sluoksnių T_m priklausomybė nuo Sr kiekio x, esant skirtingoms y = Mn/(La + Sr) santykio vertėms (simboliai). Kreivės nubrėžtos, kad vizualiai aprašytų eksperimentinius duomenis.

Didėjant Mn/(La + Sr) santykiui, Tm vertės linkusios pasiekti sotį. Didžiausios Tm vertės nanostruktūrizuotuose Al_2O_3//LSMO sluoksniuose gaunamos, kai $y \approx 1{,}15$ ir $x \approx 0{,}17$–$0{,}18$. Tuo tarpu epitaksiniuose LAO//LSMO sluoksniuose Tm didėja visame tirtame $x = 0{,}05$–$0{,}30$ intervale ir pasiekia didesnes vertes nei polikristaliniuose sluoksniuose. Šį skirtumą galima sieti su skirtinga sluoksnių mikrostruktūra ir kristalitų ribų įtaka krūvio pernašai [103, 104].

Savitosios varžos priklausomybės nuo temperatūros parodė, kad visuose tirtuose LSMO sluoksniuose vyksta metalo-izoliatoriaus virsmas, o T_m atitinka savitosios varžos maksimumą ρ_m. Šių sluoksnių savitosios varžos maksimumas ρ_m mažėjo, didėjant x visame tirtame Sr kiekio intervale ($0{,}05 \leq x \leq 0{,}30$).

3.1.3 Nanostruktūrizuotų LSMO sluoksnių magnetovarža

Magnetovarža (*MR*) buvo apibrėžta taip:

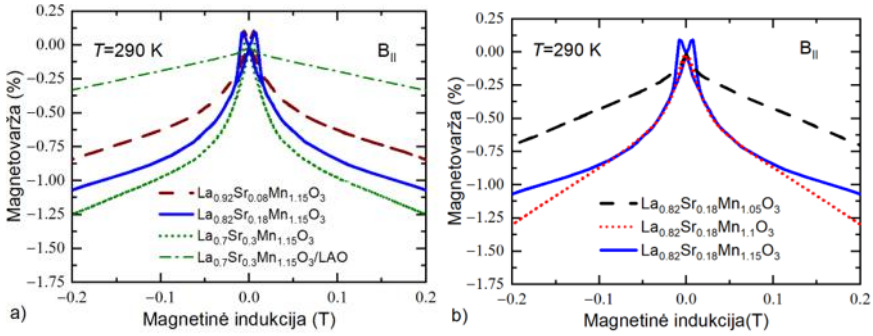
$$MR(B) = 100\% \times (\rho(B) - \rho(0))/\rho(0) \qquad (3.1.1)$$

čia $\rho(B)$ ir $\rho(0)$ yra atitinkamai savitoji varža, esant magnetinei indukcijai B, ir savitoji varža, be magnetinio lauko.

3.1.4 pav. pateiktos magnetovaržos priklausomybės nuo magnetinės indukcijos B, išmatuotos kambario temperatūroje (290 K), kai magnetinis laukas buvo nukreiptas lygiagrečiai sluoksnio plokštumai. Nanostruktūrizuotuose sluoksniuose, kuriuose $x = 0{,}18$–$0{,}30$, esant silpniems laukams stebimas ryškus neigiamos magnetovaržos pokytis, po kurio, didėjant laukui, pasireiškia lėtesnis kitimas. Šie efektai atitinkamai vadinami silpno lauko magnetovarža (LFMR) ir stipraus lauko magnetovarža (HFMR).

LFMR vertės priklauso nuo Sr kiekio: esant B = 50 mT, ji siekia apie −0,8 % (x = 0,30) ir −0,48 % (x = 0,08), o esant 0,8 T HFMR vertės atitinkamai siekia apie −4 % ir −2,5 %. Epitaksiniuose LSMO/LAO sluoksniuose LFMR nebuvo stebima, o tai rodo, kad jos kilmė daugiausia susijusi su kristalitų ir tarpkristalitinių ribų struktūra, o ne su kristalinės gardelės pokyčiais, atsirandančiais keičiant Sr kiekį.

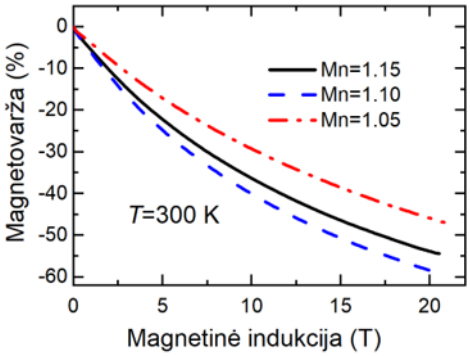
Mn pertekliaus įtaka LFMR taip pat reikšminga. Kai y = 1,10 ir 1,15, gautos panašios LFMR vertės, o beveik stechiometriniuose sluoksniuose (y = 1,05) LFMR buvo labai maža dėl žemesnės virsmo temperatūros, dėl ko kambario temperatūroje šie sluoksniai yra paramagnetinėje fazėje. Esant 0,8 T, didžiausia magnetovarža (~4,5 %) nustatyta sluoksnyje, kuriame y = 1,10. Tai galima sieti su didesne tarpkristalinių ribų struktūros netvarka, dėl kurios magnetinis laukas orientuodamas Mn magnetinius momentus stipriau sumažina sluoksnio varžą.



3.1.4 pav. Silpnų laukų magnetovaržos priklausomybės nuo magnetinės indukcijos nanostruktūrizuotuose sluoksniuose, esant skirtingam Sr kiekiui (a) ir Mn pertekliui (b). Siekiant palyginti, (a) dalyje papildomai pateikta epitaksinio LSMO sluoksnio (x = 0,30, y = 1,15) ant LAO priklausomybė. Matavimai atlikti 290 K temperatūroje.

LFMR paprastai būdinga polikristaliniams manganitams, kuriuose tarp feromagnetinių kristalitų esančios ribos sudaro barjerą per kurį vyksta poliarizuotų elektronų sukinių tuneliavimas. Nors kambario temperatūroje *LFMR* dažniausiai išnyksta, tinkamai parinkta nanostruktūrizuotų LSMO sluoksnių cheminė sudėtis leidžia šį efektą stebėti ir kambario temperatūroje. Tai rodo šių sluoksnių potencialą silpnų magnetinių laukų jutikliams. Nustatyta, kad *LFMR* didėja didėjant Sr koncentracijai ir ryškiau pasireiškia, kai Mn perteklius y > 1,10.

3.1.5 pav. pateiktos stiprių laukų magnetovaržos priklausomybės nuo Mn pertekliaus. Matyti, kad didžiausios magnetovaržos vertės kambario temperatūroje gaunamos sluoksniuose, kuriuose Mn pertekliaus santykis y = 1,10–1,15.



3.1.5 pav. $La_{1-x}Sr_xMn_yO_3$ sluoksnių magnetovaržos priklausomybės nuo magnetinio lauko, kai x = 0,20 ir skirtingas y = Mn/(La + Sr) santykis, esant 300 K temperatūrai. Magnetinis laukas nukreiptas lygiagrečiai sluoksnio plokštumai.

Siekiant paaiškinti kambario temperatūroje stebimos silpnų laukų magnetovaržos (LFMR) kilmę, buvo ištirtas LSMO sluoksnių įmagnetėjimas.

3.1.6 pav. pateiktos įmagnetėjimo M priklausomybės nuo temperatūros, išmatuotos 1000 Oe magnetiniame lauke. Siekiant palyginti skirtingus sluoksnius, įmagnetėjimo vertės normalizuotos pagal jų vertes esant 10 K. Didėjant temperatūrai, M mažėja, o visuose sluoksniuose stebimas fazinis perėjimas iš feromagnetinės į paramagnetinę būseną. Kiuri temperatūra T_C nustatoma pagal išvestinės dM/dT minimumą. Kai x = 0,08, gauta $T_C \approx 300$ K. Kitų sluoksnių T_C dėl riboto matavimo temperatūrų intervalo buvo įvertinta pagal Kiuri-Veiso dėsnį, aprašant eksperimentinius duomenis formule:

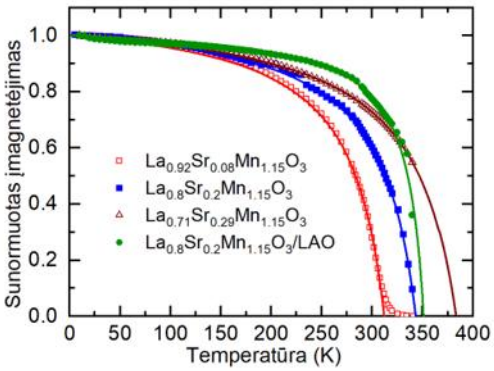
$$M=a/(T-\theta)+b \qquad (3.1.2)$$

3.1.6 pav. pateiktos aproksimavimo kreivės. Sluoksniams, kuriuose x = 0,18 ir 0,30, atitinkamai gautos $T_C \approx 343$ K ir 383 K. Taigi, visuose sluoksniuose, kurių Mn pertekliaus santykis y = 1,15, T_C yra aukštesnė už kambario temperatūrą, todėl galima paaiškinti kambario temperatūroje stebimą LFMR.

Taip pat nustatyta, kad ant polikristalinio Al_2O_3 ir monokristalinio LAO padėklų užaugintų sluoksnių T_C vertės yra beveik vienodos; skiriasi tik kreivių nuolydis temperatūroje žemiau fazinio virsmo. Ankstesni tyrimai [105, 106] parodė, kad tarpfazinės deformacijos gali reikšmingai paveikti manganitų T_C, keisdamos Mn–O–Mn ryšių ilgį ir kampą bei taip susilpnindamos dvigubą pamainininę sąveiką.

Mūsų atveju sluoksniai sudaryti iš per visą jų storį išsidėsčiusių koloninių kristalitų, kurių ilgosios ašys orientuotos statmenai padėklo paviršiui. Kristalitų plotis siekia apie 70–80 nm, o tarpkristalitinių sričių– tik apie 2–3 nm. Tokia mikrostruktūra, kai dideli kristalitai atskirti siauromis tarpkristalitinėmis ribomis, ypač sluoksniuose, kuriuose yra daugiau Mn ir Sr,

gali paaiškinti panašias T_C vertes ant monokristalinių ir polikristalinių padėklų užaugintuose sluoksniuose.



3.1.6 pav. Simboliais pateikti eksperimentiniai įmagnetėjimo rezultatai išmatuoti magnetiniame lauke vėsinant bandinį (FC), H_{FC} = 1000 Oe. Priklausomybės nuo temperatūros normalizuotos pagal įmagnetėjimą esant 10 K, kai skiriasi Sr kiekis, o Mn kiekis yra pastovus (y = 1,15). Kreivės – aproksimavimo pagal Kiuri-Veiso dėsnį rezultatai (3.1.2).

Ištirtų nestechiometrinių LSMO sluoksnių (y = 1,15) magnetinių histerezių tyrimai parodė, kad didėjant Sr kiekiui nuo x = 0,08 iki 0,30, didėja sluoksnių soties įmagnetėjimas (atitinkamai M = 840 ± 10 emu/cm^3 iki 1004 emu/cm^3) ir gerėja jų feromagnetinės savybės. Esant x = 0,30, kambario temperatūroje sluoksnis yra feromagnetinės būsenos ir pasižymi didele soties įmagnetėjimo verte bei labai maža koercityvine lauko verte (~2–3 mT), o esant x = 0,08 sluoksnis šiomis sąlygomis jau yra artimas paramagnetinei būsenai.

Gauti rezultatai rodo, kad tinkamai parinkus Sr/(La + Sr) santykį ir padidinus Mn perteklių galima suformuoti vertikaliai orientuotą nanostruktūrą su siauromis ir kokybiškomis tarpkristalitinėmis sritimis. Tokia mikrostruktūra užtikrina gerą magnetinę sąveiką tarp kristalitų ir sudaro palankias sąlygas silpnų laukų magnetovaržai (LFMR) pasireikšti kambario temperatūroje. Svarbu tai, kad norint sustiprinti LFMR nebūtina į LSMO sluoksnį įterpti papildomos izoliacinės fazės – reikiamas savybes galima pasiekti optimizuojant vienfazės LSMO nanostruktūros cheminę sudėtį ir mikrostruktūrą.

Apibendrinant galima teigti, kad ant polikristalinių Al_2O_3 padėklų užauginti nanostruktūrizuoti lantano manganito $La_{1-x}Sr_xMn_yO_3$ sluoksniai, kuriuose x = 0,3 ir Mn pertekliaus santykis y = 1,15, gali būti naudojami magnetinio lauko jutikliams, pasižymintiems iš anksto nustatytais parametrais, skirtais silpnų magnetinių laukų matavimams kambario temperatūroje. Stiprių magnetinių laukų matavimams tinkamesni sluoksniai, kuriuose x = 0,1–0,2.

3.2 Nestechiometrinių LSMO sluoksnių pagreitintas sendinimas

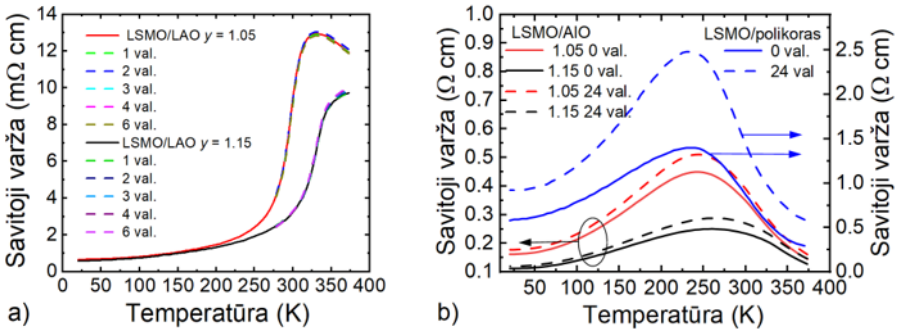
Šiame poskyryje pateikiami ant polikristalinio Al_2O_3 padėklo užaugintų nestechiometrinių nanostruktūrizuotų $La_{1-x}Sr_xMn_yO_3$ sluoksnių sendinimo proceso, jo mechanizmų bei sendinimo įtakos šių sluoksnių varžos ir magnetovaržos verčių stabilumui tyrimų rezultatai [P2].

Pagrindinis CMR jutiklių veikimo principas grindžiamas savitosios varžos priklausomybe nuo magnetinio lauko. Tačiau pradinę varžą ir jautrumą magnetiniam laukui stipriai veikia aplinkos temperatūra ir ilgalaikis sluoksnio struktūros stabilumas [73, 74]. Todėl krūvio pertašos bei magnetovaržinių savybių stabilizavimas yra vienas svarbiausių patikimo praktinio jutiklių naudojimo reikalavimų. Nanostruktūrizuotuose manganito sluoksniuose sendinimas daugiausia siejamas su defektų migracija, deguonies vakansijų persiskirstymu ir netvarkingų tarpkristalitinių ribų sričių relaksacija [78, 81, 82, 84, 112].

Atskiras šio tyrimo motyvas – nestechiometrinių $La_{1-x}Sr_xMn_yO_3$ sluoksnių, kuriuose yra Mn perteklius, naudojimas. Padidinus Mn/(La + Sr) santykį virš vieneto, metalo-izoliatoriaus virsmo temperatūrą T_m galima paslinkti aukštesnių temperatūrų link, o savitąją varžą ties T_m sumažinti, todėl tokie sluoksniai yra perspektyvūs aukštatemperatūriams impulsinio magnetinio lauko jutikliams [102]. Vis dėlto pagreitinto sendinimo įtaka Mn pertekliaus turinčių sluoksnių magnetotransporto savybėms iki šiol nėra pakankamai išsamiai ištirta. Todėl tirti ir analizuoti sluoksniai, kuriuose y = 1,05 ir y = 1,15, siekiant nustatyti, kaip mangano nestichiometrija ir tarpkristalitinių ribų struktūra veikia varžos dreifą ir magnetovaržos stabilumą.

3.2.1 Pagreitinto sendinimo įtaka savitajai varžai

Savitosios varžos matavimai (žr. 3.2.1 pav.) parodė, kad mangano kiekis ir padėklo tipas turi didelę įtaką elektrinio transporto savybėms. Ant monokristalinio $LaAlO_3$ padėklo užaugintuose sluoksniuose terminis apdorojimas 100 °C temperatūroje Ar aplinkoje beveik nepakeitė nei savitosios varžos, nei metalo-izoliatoriaus virsmo temperatūros (3.2.1a pav.). Tai rodo, kad pasirinktomis sendinimo sąlygomis kristalitai išlieka stabilūs. Priešingai, ant polikristalinio Al_2O_3 ir Polikoro padėklų užaugintuose sluoksniuose po sendinimo stebimas ryškus savitosios varžos padidėjimas, patvirtinantis, kad pagrindiniai sendinimo procesai vyksta tarpkristalitinėse srityse (3.2.1b pav.).



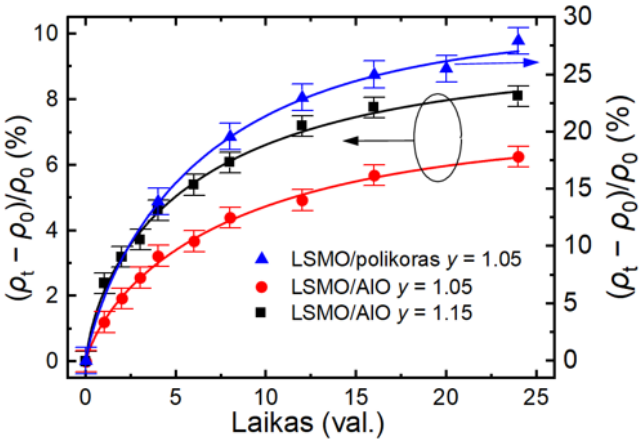
3.2.1 pav. Savitosios varžos priklausomybės nuo temperatūros: (a) ant monokristalinio $LaAlO_3$ padėklo užaugintų LSMO sluoksnių po skirtingos trukmės pagreitinto sendinimo; (b) ant polikristalinio Al_2O_3 ir Polikoro padėklų užaugintų LSMO sluoksnių prieš terminį apdorojimą ir po 24 val. terminio apdorojimo 100 °C temperatūroje Ar atmosferoje.

Santykinis savitosios varžos pokytis $(\rho_t - \rho_0)/\rho_0$ sendinimo metu (3.2.2 pav.) buvo aprašytas ištemptosios eksponentės relaksacijos modeliu [81, 82, 84]. Šis modelis tinka topologiškai netvarkingoms sistemoms, kuriose atskiri relaksacijos įvykiai nėra nepriklausomi, o jų eigą riboja ankstesni vietiniai struktūros persitvarkymai. Normalizuotas savitosios varžos pokytis išreiškiamas:

$$(\rho_t - \rho_0)/\rho_0 = [(\rho_\infty - \rho_0)/\rho_0] \times \{1 - \exp[-(t/\tau)^k]\}. \qquad (3.2.1)$$

Čia ρ_0 – pradinė savitoji varža, ρ_t – savitoji varža po sendinimo trukmės (t), ρ_∞ – ribinė savitoji varža po ilgo sendinimo, (τ) – būdingasis relaksacijos laikas, o (k) – ištemptosios eksponentės rodiklis. Al_2O_3 padėklų atveju abiejų Mn koncentracijų sluoksnių aproksimavimo parametrai buvo panašūs: kai y=1,05, τ=8,5 h ir k=0,75, o kai y=1,15, τ=6,8 h ir k=0,68. Vertės (k>0,6) rodo hierarchiškai ribojamą relaksacijos mechanizmą [81]. Polikoro padėklo pagrindu pagamintame sluoksnyje savitosios varžos pokytis buvo gerokai didesnis, o tai patvirtina, kad kristalitinių ribų netvarkos įtaka sendinimui yra reikšmingesnė nei nedidelis Mn nestechiometrijos skirtumas.

Pažymėtina, kad, nepaisant sluoksnių varžos pokyčio po pagreitinto sendinimo, tirtų sluoksnių rentgeno spindulių difrakcijos vaizduose reikšmingų pokyčių nenustatyta. Tai rodo, kad atkaitinimas 100 °C temperatūroje nepakeitė sluoksnių kristalinės struktūros. Gauti rezultatai leidžia teigti, kad sendinimo procesas daugiausia susijęs su silpnai surištu deguonimi, o deguonies praradimas ir difuzija vyksta daugiausia tarpkristalitinėmis ribomis, o ne dėl kristalitų struktūros pokyčių.



3.2.2 pav. Pagreitinto sendinimo metu LSMO sluoksnių santykinės savitosios varžos pokyčio kinetika, T=300 K temperatūroje, kai y = 1,05 ir y = 1,15. Sluoksniai buvo užauginti ant Al_2O_3 padėklų, o y = 1,05 sluoksnis – ant Polikoro padėklo. Taškai – eksperimentiniai duomenys, kreivės – aproksimavimo pagal (3.2.1) lygtį rezultatai.

Nustatyta, kad pagreitintas terminis sendinimas 100 °C temperatūroje 20 valandų stabilizuoja nestechiometrinių $La_{1-x}Sr_xMn_yO_3$ sluoksnių varžą, kuri ilgesnį laikotarpį (patikrinta po 6 mėnesių) išlieka nepakitusi 5 % ribose, nepaisant to, kad ilginant terminio apdorojimo trukmę varža toliau didėja (žr. 3.2.2 pav.).

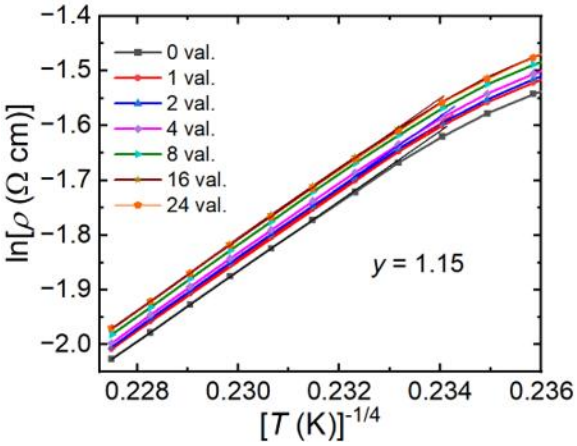
Temperatūroje, aukštesnėje už T_m, savitosios varžos duomenys buvo analizuojami taikant kintamo atstumo Mott'o šuolinio atstumo (VRH) modelį [28]. Šis modelis aprašo krūvininkų pernašą paramagnetinėje būsenoje, kai krūvininkai yra lokalizuoti bei laidumą galima aprašyti jų šuoliais tarp tam tikrų lokalizuotų būsenų. Savitoji varža išreiškiama:

$$\rho = \rho_\infty \exp[(T_0/T)^{1/4}] \qquad (3.2.2)$$

Būdingoji temperatūra T_0 yra susijusi su lokalizacijos ilgiu a ir būsenų tankiu Fermio lygmenyje $N(E\mathrm{F})$ taip:

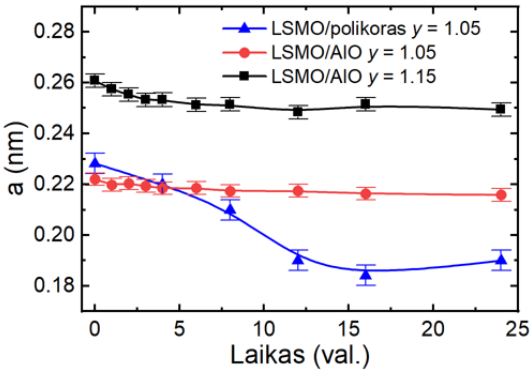
$$T_0 = 18/[a^3 \, k_B \, N(E_F)] \qquad (3.2.3)$$

3.2.3 pav. pateiktos y = 1,15 bandinio savitosios varžos priklausomybės nuo temperatūros, išmatuotos esant skirtingai atkaitinimo trukmei ir aproksimuotos taikant Mott'o VRH modelį. Eksperimentiniai duomenys gerai sutampa su (3.2.2) lygtimi temperatūroje, aukštesnėje nei 340 K. Tai rodo, kad temperatūroje, aukštesnėje už T_m, elektrinio laidumo mechanizmą lemia lokalizuotų krūvininkų šuoliai pagal Mott'o mechanizmą.



3.2.3 pav. ln ρ priklausomybės nuo $T^{-1/4}$ bandiniui, kuriame y = 1,15, po skirtingos bendrosios atkaitinimo trukmės 100 °C temperatūroje.

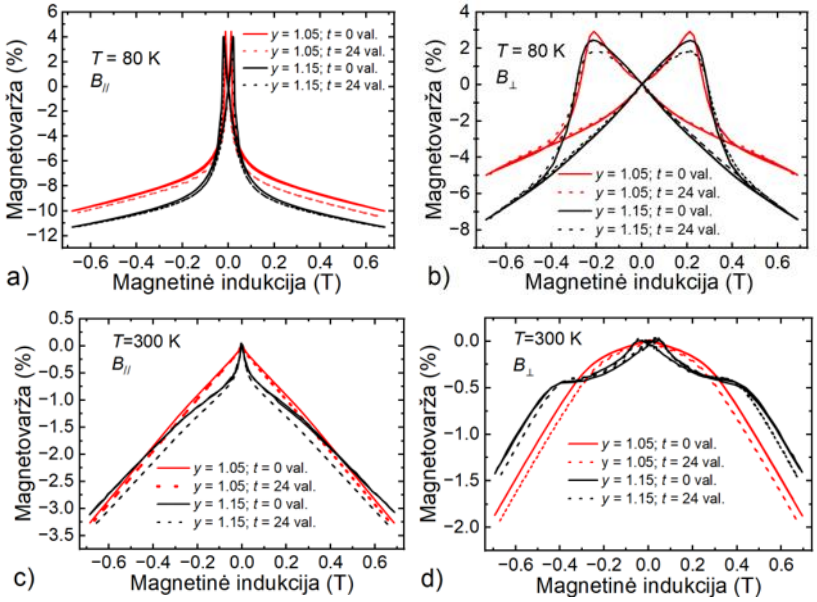
3.2.4 pav. parodytas lokalizacijos ilgio kitimas skirtinguose bandiniuose atkaitinimo metu. Šios vertės apskaičiuotos pagal (3.2.3) lygtį. Pažymėtina, kad gautos lokalizacijos ilgio vertės neturi tiesioginės fizikinės prasmės, nes lokalizacijos ilgis turi būti didesnis už Mn^{3+} – Mn^{4+} atstumą [28]. Tačiau lokalizacijos ilgio kitimas, priklausantis nuo terminio apdorojimo trukmės, gali būti naudojamas krūvininkų pernašos analizei. Lokalizacijos ilgio mažėjimas atkaitinimo metu patvirtina išvadą, kad deguonies kiekio sumažėjimas riboja Mn^{3+}– O – Mn^{4+} dvigubos pamainininės pernašos kelią. Didžiausias pokytis vyksta per pirmąsias kelias terminio apdorojimo valandas, o vėliau sistema artėja prie stabilesnės būsenos. Panašūs rezultatai buvo gauti ankstesniame mūsų darbe, tiriant stechiometrinius Polikoras//LSMO sluoksnius [73].



3.2.4 pav. Lokalizacijos ilgio kitimas atkaitinimo metu LSMO bandiniuose, kuriuose y = 1,05 ir y = 1,15.

3.2.2 Pagreitinto sendinimo įtaka magnetovaržai

Magnetovaržos atsakas buvo analizuojamas tiek silpnuose, tiek stipriuose magnetiniuose laukuose. Silpnų laukų matavimai iki 0,7 T buvo atlikti 80 K ir 300 K temperatūroje, magnetinį lauką nukreipiant lygiagrečiai arba statmenai sluoksnio plokštumai (žr. 3.2.5 pav.). Esant 80 K temperatūrai (3.2.5a pav.), *MR*(*B*) kreivėse buvo stebima tipinė polikristaliniams manganitų sluoksniams būdinga silpno lauko magnetovarža ir jos histerezė. Šis elgesys susijęs su poliarizuotų krūvininkų sukinių tuneliavimu per tarpkristalitines sritis. Magnetinį lauką nukreipus statmenai sluoksnio plokštumai (3.2.5b pav.), histerezė tampa platesne dėl ploniesiems sluoksniams būdingo demagnetizacijos efekto. Skirtingos magnetovaržos vertės sluoksniuose, kuriuose Mn koncentracija skirtinga, buvo susijusios su skirtingomis maksimalios savitosios varžos temperatūros T_m vertėmis, kurios buvo didesnės sluoksniuose, kuriuose y = 1,15.



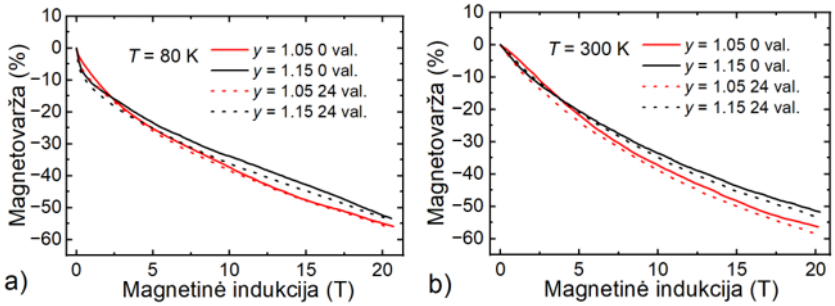
3.2.5 pav. Al_2O_3//LSMO sluoksnių, kuriuose y = 1,05 ir y = 1,15, silpnų laukų magnetovaržos priklausomybė nuo magnetinės indukcijos prieš sendinimą ir po 24 h sendinimo: (a) 80 K, *B* lygiagreti sluoksnio plokštumai; (b) 80 K, *B* statmena sluoksnio plokštumai; (c) 300 K, *B* lygiagreti sluoksnio plokštumai; (d) 300 K, *B* statmena sluoksnio plokštumai.

Esminis rezultatas yra tai, kad pagreitintas sendinimas magnetovaržos kreives pakeitė tik nežymiai. Nors po 24 val. atkaitinimo savitoji varža padidėjo, santykinis savitosios varžos pokytis dėl magnetinio lauko poveikio išliko beveik nepakitęs. Tai reiškia, kad sendinimas keičia absoliutinę

tarpkristalitinių sričių varžą, tačiau reikšmingai nekeičia magnetinio lauko sukeliamos sukinių orientacijos, lemiančios magnetovaržą, ir todėl turi silpnesnę įtaką tolimojo nuotolio sąveikai tarp kristalitų.

Nežymūs pokyčiai po Al_2O_3//LSMO sluoksnių terminio apdorojimo 100 °C temperatūroje taip pat buvo stebimi ir kambario temperatūroje (žr. 3.2.5c,d pav.).

Stiprių laukų magnetovaržos matavimai iki 20 T patvirtino magnetovaržos atsako stabilumą (3.2.6 pav.). Abiejų sudėčių sluoksniuose, esant 80 K ir 300 K temperatūrai, magnetovaržos pokytis po pagreitinto sendinimo neviršijo ~ 1%. Tai galima paaiškinti dvigubų mainų mechanizmu. Deguonies kiekio sumažėjimas kristalitų ribose sumažina aktyvių Mn^{3+}–O–Mn^{4+} šuolių centrų skaičių ir padidina savitąją varžą, tačiau santykis $\rho(B)/\rho(0)$ išlieka beveik nepakitęs, nes Mn magnetinių momentų orientacija išlieka.



3.2.6 pav. Al_2O_3//LSMO sluoksnių, kuriuose y = 1,05 ir y = 1,15, stiprių laukų magnetovaržos priklausomybės nuo magnetinės indukcijos B prieš pagreitintą sendinimą ir po jo: (a) 80 K; (b) 300 K.

Apibendrinant, pagreitinto sendinimo procedūra stabilizuoja transporto savybes, nepablogindama magnetovaržos stipriuose magnetiniuose laukuose. Šis rezultatas yra svarbus impulsinio magnetinio lauko jutikliams, kuriems būtinas stabilus kalibravimas ir atkuriamos magnetovaržos vertės atliekant pakartotinius matavimus.

3.3 Lantano manganito-grafeno struktūrų magnetovaržinės savybės

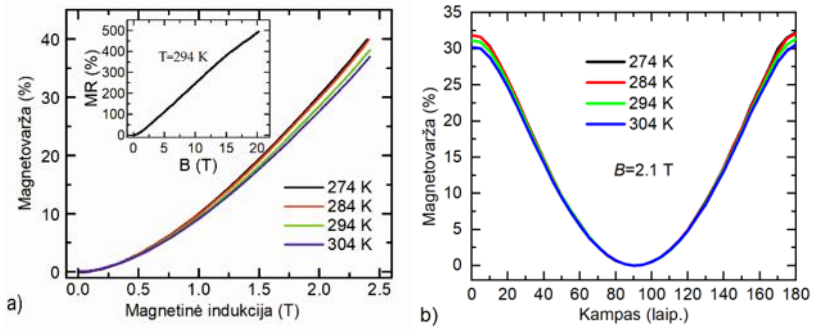
Šiame poskyryje pateikiami hibridinės manganito-grafeno struktūros magnetovaržinių savybių tyrimų ir šios struktūros pagrindu sukurto naujo magnetinio lauko jutiklio rezultatai. Parodyta, kad, matuojant hibridinės jutiklio sistemos išėjimo įtampas ir taikant specialų algoritmą, galima nustatyti magnetinio lauko stiprį ir kryptį [P3].

3.3.1 Grafeno magnetovarža

Grafeno sluoksnio varža priklauso nuo magnetinio lauko stiprio, temperatūros ir kampo tarp magnetinio lauko krypties bei grafeno sluoksnio plokštumos. 3.3.1a pav. pateikta grafeno magnetovaržos priklausomybė nuo magnetinio lauko, išmatuota esant keturioms skirtingoms temperatūroms. Šiuo atveju magnetovarža apibrėžiama taip:

$$MR_{Gr}(B) = 100\% \times [R_{Gr}(B) - R_{Gr0}]/R_{Gr0}, \qquad (3.3.1)$$

Čia $R_{Gr}(B)$ ir R_{Gr0} atitinkamai yra varžos vertės esant magnetiniam laukui (B) ir nuliniam magnetiniam laukui. Kaip matyti iš 3.3.1a pav., ši priklausomybė yra parabolinė magnetiniams laukams nuo nulio iki 1,5 T, o stipresniuose magnetiniuose laukuose ji tampa beveik tiesinė (žr. įterptą grafiką). Be to, ši priklausomybė tik silpnai priklauso nuo temperatūros.



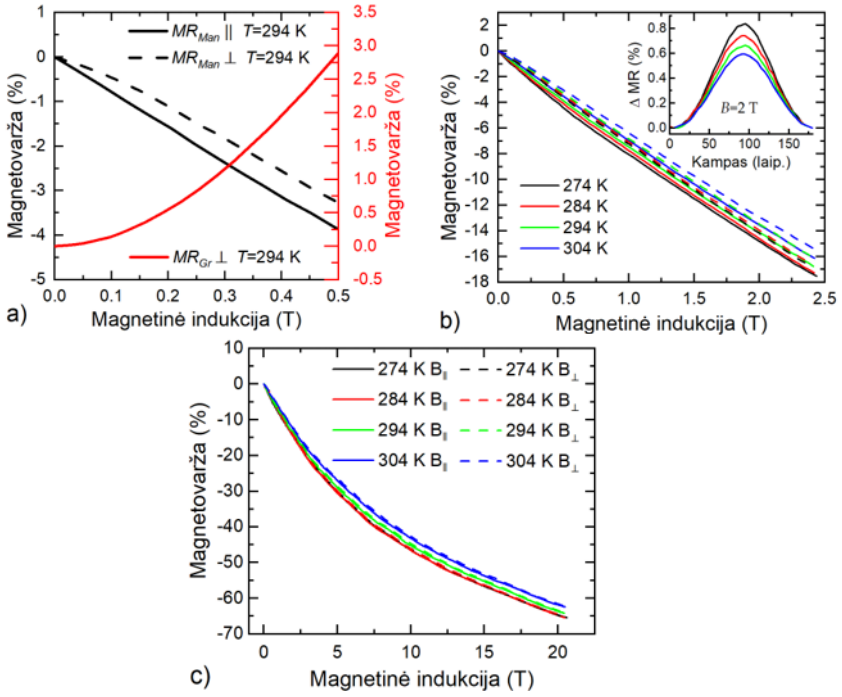
3.3.1 pav. (a) Grafeno sluoksnio magnetovarža esant skirtingoms temperatūroms, kai magnetinė indukcija (B) nukreipta statmenai sluoksnio plokštumai. Intarpe – grafeno MR esant magnetinei indukcijai B iki 21 T. (b) Grafeno sluoksnio magnetovarža, esant skirtingiems kampams (θ) tarp magnetinio lauko krypties ir sluoksnio plokštumai normalės, kai magnetinės indukcijos stipris yra 2,1 T ir temperatūra skirtinga.

Kitas svarbus parametras, leidžiantis nustatyti kampą θ tarp magnetinio lauko krypties ir jutiklio plokštumai normalės, yra varžos pokyčio priklausomybė nuo šio kampo. Šiuo požiūriu grafenas yra ideali medžiaga, nes magnetinį lauką nukreipus lygiagrečiai grafeno sluoksnio paviršiui ($\theta = 90°$), varžos pokytis yra lygus nuliui. 3.3.1b pav. pateikta grafeno sluoksnio magnetovaržos priklausomybė nuo kampo θ, esant 2,1 T magnetinei indukcijai ir skirtingoms temperatūroms. Ši priklausomybė buvo naudojama kampui tarp magnetinio lauko krypties ir jutiklio plokštumai normalės nustatyti.

3.3.2 Manganito magnetovarža

Siūlomame hibridiniame jutiklyje magnetinio lauko absoliučiajai vertei matuoti buvo naudojami nestechiometriniai $La_{1-x}Sr_xMn_yO_3$ manganito sluoksniai, kuriuose yra Mn perteklius. Kaip parodyta 3.1 skyriuje, magnetovaržos vertė priklauso nuo sluoksnio cheminės sudėties. Nustatyta, kad didinant Mn/(La + Sr) santykį iki $y \approx 1{,}15$, magnetovarža didėja. Todėl hibridinei struktūrai formuoti buvo parinkti sluoksniai, kuriuose Mn pertekliaus santykis yra $y \approx 1{,}15$. Hibridinei manganito-grafeno struktūrai užaugintų sluoksnių cheminė sudėtis, nustatyta ICP-MS metodu, buvo $La_{0,9}Sr_{0,1}Mn_{1,2}O_3$.

Manganito sluoksnio magnetovarža ir jos anizotropija pateiktos 3.3.2a pav. Tame pačiame paveiksle taip pat pateikta grafeno silpnų laukų magnetovarža. 3.3.2b pav. pateikta manganito magnetovaržos priklausomybė nuo magnetinio



3.3.2 pav. (a) Grafeno ir manganito jutiklių silpnų laukų magnetovarža kambario temperatūroje. (b) Manganito magnetovaržos priklausomybė nuo magnetinio lauko, išmatuota esant skirtingoms temperatūroms, kai magnetinis laukas buvo nukreiptas lygiagrečiai (ištisinė linija) ir statmenai (punktyrinė linija) sluoksnio plokštumai. Įterptame grafike – magnetovaržos priklausomybė nuo kampo tarp magnetinio lauko krypties ir sluoksnio paviršiaus normalės. (c) Manganito magnetovaržos priklausomybė nuo magnetinio lauko, išmatuota esant skirtingoms temperatūroms, kai magnetinis laukas buvo nukreiptas lygiagrečiai ir statmenai sluoksnio plokštumai.

lauko, išmatuota esant skirtingoms temperatūroms, kai nuolatinis magnetinis laukas iki 2,4 T buvo nukreiptas lygiagrečiai (ištisinė linija) arba statmenai (punktyrinė linija) sluoksnio plokštumai. Kaip matyti, didėjant temperatūrai magnetovarža mažėja. Be to, magnetovarža yra mažesnė, kai magnetinis laukas nukreiptas statmenai sluoksnio paviršiui, nei tada, kai jis nukreiptas lygiagrečiai sluoksnio plokštumai.

Išsamūs rezultatai pateikti šio paveikslo intarpe, kuriame parodytas absoliutinis magnetovaržos pokytis dėl kampo tarp magnetinio lauko krypties ir sluoksnio paviršiaus normalės:

$$\Delta MR[\%]=|MR(\theta)-MR(0°)| \qquad (3.3.2)$$

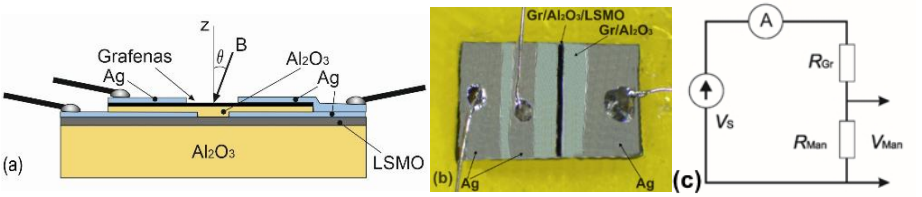
Kaip matyti, šis pokytis yra palyginti nedidelis ir neviršija 1 %. Todėl magnetinio lauko stiprio matavimo paklaida taip pat yra nedidelė (mažesnė nei 2,5 %) ir mažėja didėjant magnetinio lauko stipriui, kaip matyti 3.3.2c pav.

3.3.3 Hibridinio lantano manganito-grafeno jutiklio kūrimas

Remiantis gautais rezultatais, buvo sukurtas hibridinis manganito-grafeno jutiklis (žr. 3.3.3a ir 3.3.3b pav.). Jutiklį sudaro du jautrūs elementai: lantano manganito $La_{0,9}Sr_{0,1}Mn_{1,2}O_3$ (LSMO) sluoksnis ir grafeno sluoksnis, abu užauginti ant 250 μm storio polikristalinio Al_2O_3 padėklo. LSMO ir grafeno sluoksniai buvo sujungti į įtampos daliklio schemą ir prijungti prie pastovios 0,5 V įtampos šaltinio, kaip schematiškai pavaizduota 3.3.3c pav.

Atsako signalas buvo registruojamas kaip grandine tekanti srovė (I) ir įtampos pokytis (V_{Man}) manganito jutiklyje. Ši grandinė leidžia atskirai matuoti manganito ir grafeno sluoksnių varžos pokyčius.

Pažymėtina, kad, kaip jau parodė Lukose ir kt. [9], dėl priešingų manganito ir grafeno magnetovaržos ženklų – manganitui būdingos neigiamos, o grafenui teigiamos magnetovaržos – šiuos elementus sujungus nuosekliai ir grandinę maitinant pastovia įtampa, hibridinio jutiklio jautrį galima padidinti kelis kartus.

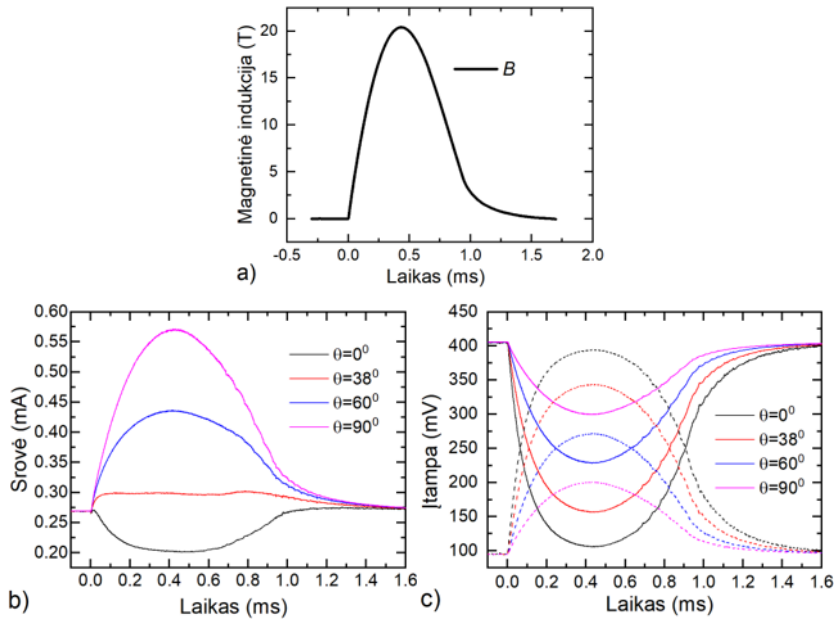


3.3.3 pav. Hibridinio jutiklio struktūra (a), vaizdas iš viršaus (b) ir elektrinė schema (c). R_{Gr} žymi grafeno sluoksnio varžą, o R_{Man} – LSMO manganito sluoksnio varžą.

3.3.4 Hibridinio jutiklio testavimo rezultatai

Jutiklis buvo išbandytas impulsiniame magnetiniame lauke, kurio impulso trukmė buvo 1 ms, o amplitudė siekė iki 21 T (žr. 3.3.4a pav.). Magnetinį lauką generavo impulsinis generatorius, pagrįstas kondensatorių baterijos iškrova per magnetinę ritę (žr. 3 skyrių). Eksperimentai buvo atliekami esant skirtingiems kampams tarp jutiklio ir magnetinio lauko, keičiant kampą jutiklio plokštumos atžvilgiu.

Grandine tekančios srovės ir įtampos manganito sluoksnyje (ištisinė kreivė) bei grafeno sluoksnyje (punktyrinė kreivė) pokyčių rezultatai pateikti atitinkamai 3.3.4b ir 3.3.4c pav.



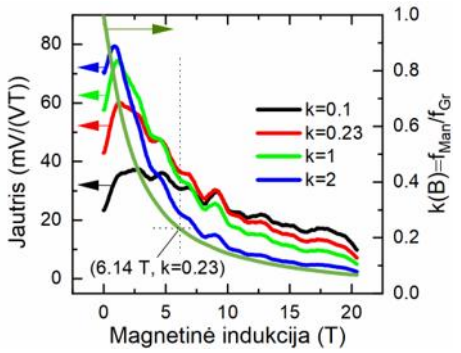
3.3.4 pav. (a) Magnetinio lauko impulsas. (b) Srovės pokytis grandinėje impulsiniame magnetiniame lauke, kai hibridinis jutiklis buvo pakreiptas skirtingais kampais tarp magnetinio lauko krypties ir jutiklio plokštumai normalės. (c) Įtampos kritimas manganito (ištisinės linijos) ir grafeno (punktyrinės linijos) sluoksniuose, esant skirtingiems kampams.

Pradinė (be magnetinio lauko) manganito sluoksnio ir grafeno sluoksnio varža atitinkamai buvo 1,5 kΩ ir 0,35 kΩ. Kaip matyti, kai kampas tarp magnetinio lauko krypties ir jutiklio plokštumai normalės yra $\theta = 0°$, didėjant magnetinio lauko stipriui, grandine tekanti srovė mažėja (3.3.4b pav.). Tačiau, kai jutiklis pakreipiamas $\theta = 38°$ ar didesniu kampu, manganito sluoksnio varžos mažėjimas yra didesnis už grafeno sluoksnio varžos didėjimą, todėl grandine tekanti srovė didėja.

Akivaizdu, kad jutiklį orientavus taip, jog jo paviršius būtų lygiagretus magnetinio lauko krypčiai, srovės pokytį lemia tik manganito sluoksnio varžos pokytis, nes grafeno sluoksnis šiuo atveju nedalyvauja. Kaip matyti iš 3.3.4c pav., grafeno varžos pokytis magnetiniame lauke padidina jutiklio jautrį, vertinamą pagal įtampos pokytį manganito sluoksnyje. Didžiausias jautris pasiekiamas, kai magnetinis laukas yra lygiagretus grafeno sluoksnio normalei (θ = 0°), o mažiausias – kai magnetinis laukas yra statmenas šiai normalei (θ = 90°).

Taip pat pažymėtina, kad, žinant magnetinio lauko kryptį, galima parinkti pradinį manganito ir grafeno sluoksnių varžų santykį taip, kad pageidaujamame magnetiniame lauke būtų pasiektas didžiausias įtampos pokytis manganito sluoksnyje (jutiklio atsako signalas didžiausias). Tai pasiekiama, kai tam tikrame magnetiniame lauke manganito sluoksnio varža tampa lygi grafeno sluoksnio varžai. Pavyzdžiui, mūsų eksperimente, kai magnetinis laukas buvo statmenas jutiklio paviršiui, didžiausias įtampos pokytis buvo stebimas esant B = 6 T magnetiniam laukui (praėjus 0,06 ms nuo impulso pradžios). Buvo pademonstruota, kad tokio hybridinio jutiklio jautris stipriai priklauso nuo pradinių grafeno ir manganito varžų santykio $k = R_{Gr}/R_{Man}$ (3.3.5 pav.) Mūsų atveju k=0.23. Jautrį apibrėžėme kaip elektrinės schemos (žr. 3.3.3b pav.) vidurio taško įtampos normuotos į šaltinio įtampą išvestinė magnetinio lauko stiprio atžvilgiu:

$$S(B) = \left|\frac{d}{dB}\left(\frac{V_{mid}}{V_s}\right)\right| . \qquad (3.3.3)$$



3.3.5 pav. Apskaičiuotos jutiklio jautrio kreivės, esant skirtingiems pradiniams varžų santykiams k, ir eksperimentiniu būdu nustatytas manganito bei grafeno sluoksnių normuotų varžos pokyčių santykis (dešinės pusės skalė).

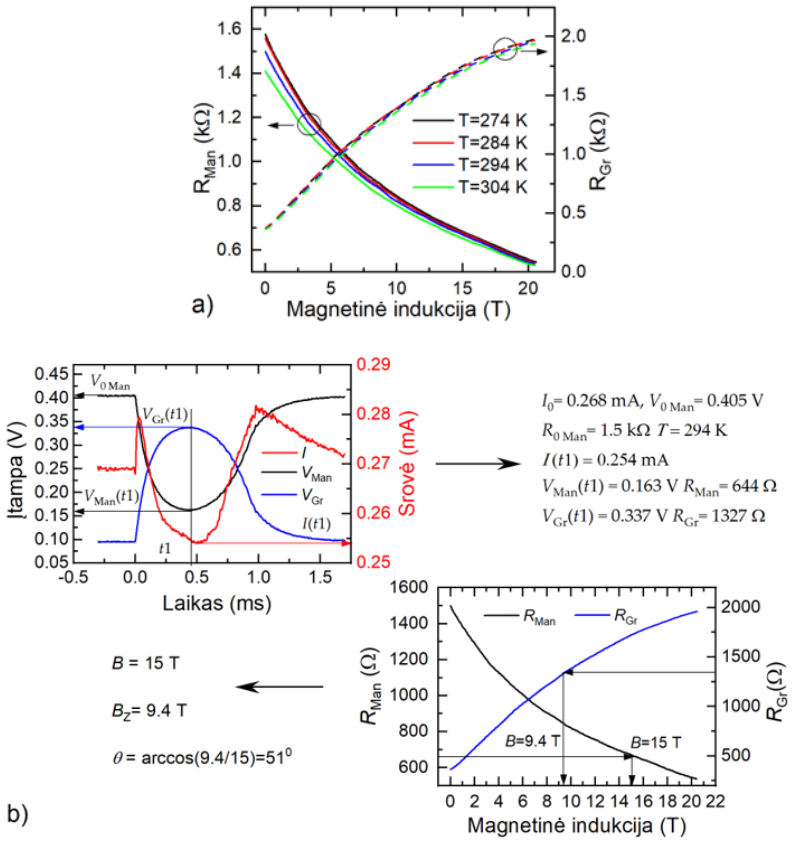
Kaip matyti iš 3.3.5 pav., keičiant k vertes, jautrumo kreivių maksimumai pasislenka. Eksperimentiniu atveju nagrinėjamame grafeno-manganito jutiklyje k buvo maždaug lygus 0,23. Esant šiai k vertei, jautris yra didžiausias ties ~6 T. Tačiau maksimalus jutiklio jautris, siekęs ~60 mV/(V·T) (raudona

kreivė), buvo stebimas 0,9–2,5 T magnetinio lauko intervale. Ši vertė yra panaši į Si pagrindu veikiančių Holo jutiklių jautrį (~100 mV/(V·T)) [115].

Remiantis gautais rezultatais, pasiūlytas naujas magnetinio lauko matuoklis, leidžiantis nustatyti magnetinio lauko vertę ir jo orientaciją jutiklio plokštumos atžvilgiu. Elektroninė sistema, skirta jutikliui maitinti, įtampai manganito sluoksnyje matuoti ir duomenims perduoti į asmeninį kompiuterį (PC), pagrįsta [11] šaltinyje aprašyta konstrukcija, pasižyminčia 16 bitų skiriamąja geba ir 12,5 MS/s diskretizavimo sparta. Patobulinimai buvo atlikti įvedus srovės matavimo galimybę.

Jutiklių varža yra netiesinė magnetinės indukcijos B funkcija ir priklauso nuo temperatūros, todėl norint iš varžos pokyčio ΔR nustatyti magnetinio lauko stiprį, būtina kalibruoti tiek grafeno, tiek manganito jutiklius. Kalibravimas buvo atliktas naudojant 2 skyriuje aprašytą stipraus magnetinio lauko generatorių. Skirtingoms temperatūroms sudarytos ir kompiuteryje išsaugotos kalibravimo kreivių šeimos $R_{Gr}(B)$ ir $R_{Man}(B)$, kai magnetinis laukas buvo nukreiptas atitinkamai statmenai grafeno sluoksnio paviršiui ir statmenai bei lygiagrečiai manganito sluoksnio plokštumai. Kalibravimo kreivių pavyzdys pateiktas 3.3.6a pav.

Supaprastintas stipraus impulsinio magnetinio lauko stiprio ir jo kampo θ su jutiklio plokštumos normale nustatymo algoritmas pateiktas 3.3.6b pav. Manganito jutiklis leidžia nustatyti magnetinio lauko indukcijos absoliučiąją vertę ($|B|$), o grafeno jutiklio varža priklauso tiek nuo ($|B|$), tiek nuo kampo θ. Stiprių magnetinių laukų atveju galima nepaisyti manganito magnetovaržos anizotropijos. Grafeno atsakas priklauso nuo magnetinio lauko projekcijos į jutiklio plokštumos normalę ir aprašomas ryšiu $B_z=|B|\cos\theta$. Todėl, išmatavus manganito ir grafeno sluoksnių varžas, galima nustatyti tiek magnetinio lauko indukcijos absoliučiąją vertę ($|B|$), tiek jo kryptį apibūdinantį kampą θ. 3.3.6b pav. pateiktame pavyzdyje hibridinis jutiklis buvo pasuktas 50° kampu. Matuojant srovę ir įtampas pasirinktu laiko momentu t_1, nustatytos varžos, ir tada iš manganito varžos priklausomybės nuo magnetinio lauko nustatyta magnetinės indukcijos absoliučioji vertė – 15 T, o iš grafeno varžos priklausomybės – jos dedamoji normalės kryptimi 9,4 T. Iš šių verčių nustatoma, kad kampas θ tarp magnetinio lauko krypties ir jutiklio paviršiaus normalės yra 51°. Eksperimentų serija parodė, kad kampo matavimo tikslumas buvo maždaug ±2°. Šie skaičiavimai atliekami viso magnetinio lauko impulso metu, o gauti rezultatai pateikiami kompiuterio ekrane.



3.3.6 pav. (a) Manganito (kairioji skalė) ir grafeno (dešinioji skalė) kalibravimo kreivių $R(B)$ šeima, gauta esant skirtingoms temperatūroms. Vienoda ištisinių ir punktyrinių kreivių spalva atitinka tą pačią temperatūrą. (b) Magnetinio lauko stiprio ir kampo matavimo procedūros pavyzdys.

Apibendrinant galima teigti, kad buvo sėkmingai sukurtas naujas hibridinis manganito-grafeno jutiklis, leidžiantis padidintu jautriu matuoti tiek magnetinio lauko stiprį, tiek jo kryptį. Manganitui būdingos neigiamos ir grafenui – teigiamos magnetovaržos derinys pagerino jutiklio charakteristikas ir sudarė galimybę tiksliai nustatyti magnetinį lauką plačiame jo verčių ir krypčių intervale.

Optimizavus jutiklio konstrukciją, įskaitant elektrodų atstumą ir sluoksnių matmenis, reikšmingai padidėjo magnetovarža ir jautris, ypač kai magnetinis laukas buvo statmenas jutiklio paviršiui.

Sukurtas hibridinis jutiklis parodė potencialą taikymams, kuriuose reikalingas patikimas magnetinio lauko stiprio ir krypties matavimas plačiame magnetinių laukų ir darbinės temperatūros intervale.

BENDROSIOS IŠVADOS

1. Sr kiekis $x = 0{,}05–0{,}30$ ir Mn santykis $y = \mathrm{Mn}/(\mathrm{La} + \mathrm{Sr}) > 1$ nestechiometriniuose nanostruktūrizuotuose $La_{1-x}Sr_xMn_yO_3$ manganitų sluoksniuose turi didelę įtaką pagrindinėms šių sluoksnių elektros pernašos ir magnetinėms savybėms:

   1.1 Nanostruktūrizuotų $La_{1-x}Sr_xMn_yO_3$ sluoksnių metalo-izoliatoriaus virsmo temperatūros T_m didžiausia vertė, kai $y = 1{,}05$, pasiekiama esant $x \approx 0{,}18$. Didėjant Mn pertekliui iki $y = 1{,}15$, šis maksimumas pasislenka mažesnių Sr koncentracijų link ($x = 0{,}10–0{,}17$). Tai aiškinama Mn pertekliumi, dėl kurio susidaro La vakansijos, didėja Mn^{4+}/Mn^{3+} santykis ir stiprėja sluoksnių feromagnetinės savybės.

   1.2 Nanostruktūrizuotuose $La_{1-x}Sr_xMn_yO_3$ sluoksniuose, kurių cheminė sudėtis $x = 0{,}30$ ir $y = 1{,}15$, nustatyta padidėjusi silpnų laukų magnetovarža – (−1,23–−0,8) %, esant 250–290 K temperatūrai ir $B = 50$ mT magnetinei indukcijai. Tai galima paaiškinti poliarizuotų spinų krūvininkų tuneliavimu per plonas tarpkristalitines ribas, skiriančias aukštos struktūrinės kokybės kristalitus. Šie kristalitai net kambario temperatūroje yra soties feromagnetinėje būsenoje, ką patvirtina aukšta Kiuri temperatūra ($T_C = 383$ K) ir didelė soties įmagnetėjimo vertė ($M = 870$ emu/cm³).

2. Ant polikristalinių Al_2O_3 padėklų užauginti nanostruktūrizuoti $La_{1-x}Sr_xMn_yO_3$ sluoksniai, kurių $x = 0{,}3$ ir $y = 1{,}15$, gali būti naudojami magnetinio lauko jutikliams, skirtiems silpnų magnetinių laukų (< 1 T) matavimams kambario temperatūroje. Stiprių magnetinių laukų matavimams tinkamesni sluoksniai, kurių $x = 0{,}1–0{,}2$ ir $y > 1{,}1$.

3. Nestechiometrinių nanostruktūrizuotų $La_{1-x}Sr_xMn_yO_3$ sluoksnių pagreitintas terminis sendinimas argono atmosferoje 100 °C temperatūroje 20 valandų stabilizuoja šių sluoksnių varžos ir magnetovaržos vertes, kurios ilgesnį laikotarpį (patikrinta po 6 mėnesių) išlieka nepakitusios 5 % ribose, nepaisant to, kad ilginant terminio apdorojimo trukmę varža toliau didėja.

4. Sendinimo kinetika lemia reikšmingą sluoksnių savitosios varžos padidėjimą, kurį galima paaiškinti topologiškai netvarkingoms sistemoms būdingu hierarchiškai ribojamos relaksacijos dinamikos modeliu, aprašomu ištemptąja eksponente. Labiausiai tikėtina, kad šį procesą lemia deguonies kiekio sumažėjimas ir jo difuzija nanostruktūrizuotų manganito

sluoksnių tarpkristalitinėse ribose, o ne netvarki kristalitų struktūra susijusi su sluoksnių nestechiometriškumu dėl Mn pertekliaus.

5. Hibridinės nestechiometrinio manganito ir grafeno struktūros Al_2O_3//$La_{1-x}Sr_xMn_yO_3$/Al_2O_3/Grafenas dizainas, kai grafenas perkeliamas ant manganito sluoksnio viršaus naudojant apsauginį Al_2O_3 sluoksnį, leidžia sumažinti aktyviosios manganito-grafeno jutiklio srities matmenis ir taip sudaryti sąlygas vienu metu lokaliai matuoti magnetinio lauko stiprį bei kryptį.
6. Sujungus hibridinės struktūros manganito ir grafeno elementus įtampos daliklyje, magnetinio lauko, kuriam esant jautris yra didžiausias, vertė nustatoma abiejų elementų pradinių (B=0) varžų santykiu $k = R_{Gr}/R_{Man}$, o jutiklį galima derinti į pasirinktam lauko ruožui, parenkant šį santykį. Manganito $La_{0,9}Sr_{0,1}Mn_{1,2}O_3$ ir grafeno hibridinė struktūra su k = 0,23 pasiekė didžiausią jautrį 60 mV/(V·T), esant 0,9–2,5 T magnetiniam laukui, kuris yra palyginamas su silicio Holo jutiklių jautriu.

REFERENCES

[1] Yole Intelligence. Magnetic Sensors 2024. 2024. https://www.yolegroup.com/product/report/magnetic-sensors-2024/.

[2] He, G.; Zhang, Y.; Xiao, G. Sensitivity Enhancement and Random Telegraph Noise in Magnetic Tunnel Junctions with Compensated Anisotropy. *Phys. Rev. Appl.* 2023, 19, 024069.

[3] Battesti, R.; Beard, J.; Böser, S.; Bruyant, N.; Budker, D.; Crooker, S.A.; Daw, E.J.; Flambaum, V.V.; Inada, T.; Irastorza, I.G.; Karbstein, F.; Kim, D.L.; Kozlov, M.G.; Melhem, Z.; Phipps, A.; Pugnat, P.; Rikken, G.; Rizzo, C.; Schott, M.; Semertzidis, Y.K.; ten Kate, H.H.J.; Zavattini, G. High magnetic fields for fundamental physics. *Phys. Rep.* 2018, 765–766, 1–39.

[4] Žurauskienė, N. Engineering of Advanced Materials for High Magnetic Field Sensing: A Review. *Sensors* 2023, 23, 2939.

[5] Kozlova, N.; Walter, T.; Dörr, K.; Eckert, D.; Handstein, A.; Skourski, Y.; Müller, K.-H.; Schultz, L. Intergrain Magnetoresistance and Resistance Relaxation of La0.7Sr0.3MnO3 Thin Films in Pulsed Magnetic Fields up to 60 T. *Physica B: Condens. Matter* 2004, 346–347, 74–78.

[6] Žurauskienė, N.; Balevičius, S.; Cimmperman, P.; Stankevič, V.; Keršulis, S.; Schneider, M.; Liebfried, O.; Plaušinaitienė, V.; Abrutis, A. B-scalar sensor using CMR effect in thin polycrystalline manganite films. *IEEE Trans. Plasma Sci.* 2011, 39, 411–416.

[7] Novoselov, K.S.; Geim, A.K.; Morozov, S.V.; Jiang, D.; Katsnelson, M.I.; Grigorieva, I.V.; Dubonos, S.V.; Firsov, A.A. Two-dimensional gas of massless Dirac fermions in graphene. *Nature* 2005, 438, 197–200.

[8] Kisslinger, F.; Ott, C.; Heide, C.; Kampert, E.; Butz, B.; Spiecker, E.; Shallcross, S.; Weber, H.B. Linear magnetoresistance in mosaic-like bilayer graphene. *Nat. Phys.* 2015, 11, 650–653.

[9] Lukose, R.; Zurauskiene, N.; Balevicius, S.; Stankevic, V.; Keršulis, S.; Plausinaitiene, V.; Navickas, R. Hybrid graphene-manganite thin film structure for magnetoresistive sensor application. *Nanotechnology* 2019, 30, 355503.

[10] Balevičius, S.; Žurauskienė, N.; Stankevič, V.; Keršulis, S.; Plaušinaitienė, V.; Abrutis, A.; Zherlitsyn, S.; Herrmannsdörfer, T.; Wosnitza, J.; Wolff-Fabris, F. Nanostructured thin manganite films in megagauss magnetic field. *Appl. Phys. Lett.* 2012, 101, 092407.

[11] Stankevič, T.; Medišauskas, L.; Stankevič, V.; Balevičius, S.; Žurauskienė, N.; Liebfried, O.; Schneider, M. Pulsed magnetic field measurement system based on colossal magnetoresistance-B-scalar sensors for railgun investigation. *Rev. Sci.* Instrum. 2014, 85, 044704.

[12] Stankevič, V.; Keršulis, S.; Dilys, J.; Bleizgys, V.; Viliūnas, M.; Vertelis, V.; Maneikis, A.; Rudokas, V.; Plaušinaitienė, V.; Žurauskienė, N. Measurement System for Short-Pulsed Magnetic Fields. *Sensors* 2023, 23, 1435. https://doi.org/10.3390/s23031435.

[13] Lukose, R.; Zurauskiene, N.; Stankevic, V.; Vagner, M.; Plausinaitiene, V.; Niaura, G.; Kersulis, S.; Balevicius, S.; Bolli, E.; Mezzi, A.; Kaciulis, S. Room temperature Co-doped manganite/graphene sensor operating at high pulsed magnetic fields. *Sci. Rep.* 2019, 9, 9497.

[14] Coey, J.M.D.; Viret, M.; von Molnár, S. Mixed-valence manganites. *Adv. Phys.* 1999, 48 (2), 167–293.

[15] Dörr, K. Ferromagnetic manganites: spin-polarized conduction versus competing interactions. *J. Phys. D: Appl. Phys.* 2006, 39 (7), R125.

[16] Haghiri-Gosnet, A.-M.; Renard, J.-P. CMR manganites: physics, thin films and devices. *J. Phys. D: Appl. Phys.* 2003, 36 (8), R127–R150.

[17] Zener, C. Interaction between the d shells in the transition metals. *Phys. Rev.* 1951, 81 (3), 440.

[18] Zener, C. Interaction between the d-shells in the transition metals. II. Ferromagnetic compounds of manganese with perovskite structure. *Phys. Rev.* 1951, 82 (3), 403.

[19] Anderson, P.W.; Hasegawa, H. Considerations on double exchange. *Phys. Rev.* 1955, 100 (2), 675.

[20] Ramirez, A.P. Colossal magnetoresistance. *J. Phys.: Condens. Matter* 1997, 9, 8171–8199.

[21] de Gennes, P.-G. Effects of Double Exchange in Magnetic Crystals. *Phys. Rev.* 1960, 118, 141–154.

[22] De Teresa, J.M.; Ibarra, M.R.; Algarabel, P.A.; Ritter, C.; Marquina, C.; Blasco, J.; García, J.; del Moral, A.; Arnold, Z. Evidence for magnetic polarons in the magnetoresistive perovskites. *Nature* 1997, 386 (6622), 256–259.

[23] Palstra, T.T.M.; Ramirez, A.P.; Cheong, S.-W.; Zegarski, B.R.; Schiffer, P.; Zaanen, J. Transport mechanisms in doped $LaMnO_3$: Evidence for polaron formation. *Phys. Rev. B* 1997, 56 (9), 5104–5107.

[24] Worledge, D.C.; Snyder, G.J.; Beasley, M.R.; Geballe, T.H.; Hiskes, R.; DiCarolis, S. Anneal-tunable Curie temperature and transport of $La_{0.67}Ca_{0.33}MnO_3$. *J. Appl. Phys.* 1996, 80 (9), 5158–5161.

[25] Kasuya, T. Mobility of the antiferromagnetic large polaron. *Solid State Commun.* 1970, 8 (20), 1635–1638.

[26] Snyder, G.J.; Hiskes, R.; DiCarolis, S.; Beasley, M.R.; Geballe, T.H. Intrinsic electrical transport and magnetic properties of La0.67Ca0.33MnO3 and La0.67Sr0.33MnO3 MOCVD thin films and bulk material. *Phys. Rev. B* 1996, 53 (21), 14434–14444.

[27] Jia, Y.X.; Lu, L.; Khazeni, K.; Yen, D.; Lee, C.S.; Zettl, A. Pr-doping of the high-magnetoresistance perovskite Nd2/3Sr1/3MnO3. *Solid State Commun.* 1995, 94 (11), 917–920.

[28] Viret, M.; Ranno, L.; Coey, J.M.D. Magnetic localization in mixed-valence manganites. *Phys. Rev. B* 1997, 55 (13), 8067–8070.

[29] Coey, J.M.D.; Viret, M.; Ranno, L.; Ounadjela, K. Electron Localization in Mixed-Valence Manganites. *Phys. Rev. Lett.* 1995, 75, 3910–3913.

[30] von Helmolt, R.; Wecker, J.; Holzapfel, B.; Schultz, L.; Samwer, K. Giant Negative Magnetoresistance in Perovskite-like $La_{2/3}Ba_{1/3}MnO_X$ Ferromagnetic Films. *Phys. Rev. Lett.* 1993, 71, 2331–2333.

[31] Jin, S.; Tiefel, T.H.; McCormack, M.; Fastnacht, R.A.; Ramesh, R.; Chen, L.H. Thousandfold Change in Resistivity in Magnetoresistive La-Ca-Mn-O Films. *Science* 1994, 264, 413–415.

[32] Levy, P.M. Giant Magnetoresistance in Magnetic Layered and Granular Materials. *Science* 1992, 256, 972–973.

[33] Urushibara, A.; Moritomo, Y.; Arima, T.; Asamitsu, A.; Kido, G.; Tokura, Y. Insulator-Metal Transition and Giant Magnetoresistance in $La_{1-X}Sr_XMnO_3$. *Phys. Rev. B* 1995, 51, 14103–14109.

[34] Millis, A.J.; Littlewood, P.B.; Shraiman, B.I. Double Exchange Alone Does Not Explain the Resistivity Of $La_{1-X}Sr_xMnO_3$. *Phys. Rev. Lett.* 1995, 74, 5144–5147.

[35] Pla, D.; Jimenez, C.; Burriel, M. Engineering of Functional Manganites Grown by MOCVD for Miniaturized Devices. *Adv. Mater. Interfaces* 2017, 4, 1600974.

[36] Dagotto, E.; Hotta, T.; Moreo, A. Colossal Magnetoresistant Materials: The Key Role of Phase Separation. *Phys. Rep.* 2001, 344, 1–153.

[37] Salamon, M.B.; Jaime, M. The Physics of Manganites: Structure and Transport. *Rev. Mod. Phys.* 2001, 73, 583–628.

[38] Ziese, M. Extrinsic Magnetotransport Phenomena in Ferromagnetic Oxides. *Rep. Prog. Phys.* 2002, 65, 143–249.

[39] van Tendeloo, G.; Lebedev, O.I.; Hervieu, M.; Raveau, B. Structure and Microstructure of Colossal Magnetoresistant Materials. *Rep. Prog. Phys.* 2004, 67, 1315–1365.

[40] Goodenough, J.B. Electronic and Ionic Transport Properties and Other Physical Aspects of Perovskites. *Rep. Prog. Phys.* 2004, 67, 1915–1993.

[41] Tokura, Y. Critical Features of Colossal Magnetoresistive Manganites. *Rep. Prog. Phys.* 2006, 69, 797–851.

[42] Israel, C.; Calderon, M.J.; Mathur, N.D. ChemInform Abstract: The Current Spin on Manganites. *ChemInform* 2008, 39.

[43] Pękała, M.; Pękała, K.; Drozd, V. Magnetotransport Study of Nanocrystalline and Polycrystalline Manganites $La_{0.8}Sr_{0.2}MnO_3$ in High Magnetic Fields. *J. Appl. Phys.* 2015, 117, 175902.

[44] Hwang, H.Y.; Cheong, S.-W.; Ong, N.P.; Batlogg, B. Spin-Polarized Intergrain Tunneling in $La_{2/3}Sr_{1/3}MnO_3$. *Phys. Rev. Lett.* 1996, 77, 2041–2044.

[45] Lee, S.; Hwang, H.Y.; Shraiman, B.I.; Ratcliff, W.D., II; Cheong, S.-W. Intergrain magnetoresistance via second-order tunneling in perovskite manganites. *Phys. Rev. Lett.* 1999, 82, 4508–4511.

[46] Evetts, J.E.; Blamire, M.G.; Mathur, N.D.; Isaac, S.P.; Teo, B.-S.; Cohen, L.F.; Macmanus-Driscoll, J.L. Defect-Induced Spin Disorder and Magnetoresistance in Single-Crystal and Polycrystal Rare-Earth Manganite Thin Films. *Philos. Trans. R. Soc. Lond. Ser. A Math. Phys. Eng. Sci.* 1998, 356, 1593–1615.

[47] Wagner, P.H.; Metlushko, V.; Trappeniers, L.; Vantomme, A.; Vanacken, J.; Kido, G.; Moshchalkov, V.V.; Bruynseraede, Y. Magnetotransport in Epitaxial Thin Films of the Magnetic Perovskite $Pr_{0.5}Sr_{0.5}MnO_3$. *Phys. Rev. B* 1997, 55, 3699–3707.

[48] Wagner, P.; Gordon, I.; Trappeniers, L.; Vanacken, J.; Herlach, F.; Moshchalkov, V.V.; Bruynseraede, Y. Spin Dependent Hopping and Colossal Negative Magnetoresistance in Epitaxial $Nd_{0.52}Sr_{0.48}MnO_3$ Films in Fields up to 50 T. *Phys. Rev. Lett.* 1998, 81, 3980–3983.

[49] Lu, Y.; Li, X.W.; Gong, G.Q.; Xiao, G.; Gupta, A.; Lecoeur, P.; Sun, J.Z.; Wang, Y.Y.; Dravid, V.P. Large magnetotunneling effect at low magnetic fields in micrometer-scale epitaxial $La_{0.67}Sr_{0.33}MnO_3$ tunnel junctions. *Phys. Rev. B* 1996, 54, R8357–R8360.

[50] Sadhu, A.; Bhattacharyya, S. Enhanced Low-Field Magnetoresistance in $La_{0.71}Sr_{0.29}MnO_3$ Nanoparticles Synthesized by the Nonaqueous Sol–Gel Route. *Chem. Mater.* 2014, 26, 1702–1710.

[51] Sun, J.Z.; Gallagher, W.J.; Duncombe, P.R.; Krusin-Elbaum, L.; Altman, R.A.; Gupta, A.; Lu, Y.; Gong, G.Q.; Xiao, G. Observation of large low-field magnetoresistance in trilayer perpendicular transport devices made using doped manganate perovskites. *Appl. Phys. Lett.* 1996, 69, 3266–3268.

[52] Stankevic, V.; Zurauskiene, N.; Kersulis, S.; Plausinaitiene, V.; Lukose, R.; Klimantavicius, J.; Tolvaišienė, S.; Skapas, M.; Selskis, A.; Balevicius, S. Nanostructured Manganite Films Grown by Pulsed Injection MOCVD: Tuning Low- and High-Field Magnetoresistive Properties for Sensors Applications. *Sensors* 2022, 22, 605.

[53] Balcells, L.; Fontcuberta, J.; Martínez, B.; Obradors, X. High-Field Magnetoresistance at Interfaces in Manganese Perovskites. *Phys. Rev. B* 1998, 58, R14697–R14700.

[54] Kozlova, N.; Dörr, K.; Eckert, D.; Walter, T.; Müller, K.-H. Intergrain Magnetoresistance of $La_{0.7}Sr_{0.3}MnO_3$ in Pulsed Magnetic Fields up to 50T. *J. Magn. Magn. Mater.* 2003, 261, 48–55.

[55] Pękała, M.; Kozlova, N.; Drozd, V. Comparison of Magnetotransport Properties of Nano- and Microcrystalline $La_{0.7}Ca_{0.3}MnO_3$ Manganites in High Magnetic Field. *J. Appl. Phys.* 2008, 104, 123902.

[56] Tokunaga, M.; Miura, N.; Tomioka, Y.; Tokura, Y. High-Field Magnetization Process in $R_{1/2}Ca_{1/2}MnO_3$(R=Sm and Y) up to 100 T. *Phys. Rev. B* 1999, 60, 6219–6222.

[57] Gangineni, R.B.; Dörr, K.; Kozlova, N.; Nenkov, K.; Müller, K.-H.; Schultz, L.; Seetha Lakshmi, L. Dependence of the High-Field Grain-Boundary Magnetoresistance of Ferromagnetic Manganites on Curie Temperature. *J. Appl. Phys.* 2006, 99, 053904.

[58] Zurauskiene, N.; Balevicius, S.; Pavilonis, D.; Stankevic, V.; Plausinaitiene, V.; Zherlitsyn, S.; Herrmannsdorfer, T.; Law, J.M.; Wosnitza, J. Magnetoresistance and Resistance Relaxation of Nanostructured La-Ca-MnO Films in Pulsed Magnetic Fields. *IEEE Trans. Magn.* 2014, 50, 6100804.

[59] Žurauskienė, N.; Balevičius, S.; Stankevič, V.; Keršulis, S.; Klimantavičius, J.; Plaušinaitienė, V.; Kubilius, V.; Skapas, M.; Juškėnas, R.; Navickas, R. Magnetoresistive properties of thin nanostructured manganite films grown by metalorganic chemical vapour deposition onto glass-ceramics substrates. *J. Mater. Sci.* 2018, 53, 12996–13009. https://doi.org/10.1007/s10853-018-2567-y.

[60] Žurauskienė, N.; Pavilonis, D.; Klimantavičius, J.; Balevičius, S.; Stankevič, V.; Keršulis, S.; Plaušinaitienė, V.; Abrutis, A.; Lukošė, R.; Skapas, M.; Juškėnas, R.; Knašienė, B.; Naujalis, E.; Law, J.M. Influence of MOCVD Growth Pressure on Magnetoresistance of Nanostructured La-Ca-Mn-O Films Used for Magnetic Field Sensors. *IEEE Trans. Plasma Sci.* 2017, 45, 2780–2786.

[61] Žurauskienė, N.; Rudokas, V.; Keršulis, S.; Stankevič, V.; Pavilonis, D.; Plaušinaitienė, V.; Vagner, M.; Balevičius, S. Magnetoresistance and Its Relaxation of Nanostructured La-Sr-Mn-Co-O Films: Application for Low Temperature Magnetic Sensors. *J. Magn. Magn. Mater.* 2021, 539, 168340.

[62] Rudokas, V.; Žurauskienė, N.; Lukošė, R.; Keršulis, S.; Stankevič, V.; Pavilonis, D.; Balevičius, S.; Plaušinaitienė, V.; Vagner, M.; Skapas, M.; Arsenijevic, S. La–Sr–Mn–Co–O Films for High Pulsed Magnetic Field Measurements at Cryogenic Temperatures. *IEEE Trans. Plasma Sci.* 2019, 47, 4541–4546.

[63] Xu, Y.; Memmert, U.; Hartmann, U. Magnetic Field Sensors from Polycrystalline Manganites. *Sens. Actuators A: Phys.* 2001, 91, 26–29.

[64] Krichene, A.; Boujelben, W.; Mukherjee, S.; Shah, N.A.; Solanki, P.S. An Empirical Model for Magnetic Field Dependent Resistivity and Magnetoresistance in Manganites: Application on Polycrystalline Charge-Ordered $La_{0.4}Gd_{0.1}ca_{0.5}MnO_3$. *Phys. Chem. Chem. Phys.* 2018, 20, 12608–12617.

[65] Dhieb, S.; Krichene, A.; Fettar, F.; Chniba Boudjada, N.; Boujelben, W. Stability of Charge Ordering in $La_{0.5-X}Ho_XCa_{0.5}MnO_3$ Polycrystalline Manganites. *Appl. Phys. A* 2021, 127, 700.

[66] Das, K.; Dasgupta, P.; Poddar, A.; Das, I. Significant Enhancement of Magnetoresistance with the Reduction of Particle Size in Nanometer Scale. *Sci. Rep.* 2016, 6, 20351.

[67] Gamzatov, A.G.; Gadzhimuradov, T.A. Low-Temperature Intergranular Spin Transport in $La_{0.5}Ca_{0.4}Li_{0.1}MnO_3$ Manganite Under High Magnetic Field (1T≤H≤14T). *J. Low Temp. Phys.* 2016, 185, 590–596.

[68] Balevičius, S.; Žurauskienė, N.; Stankevič, V.; Keršulis, S.; Baškys, A.; Bleizgys, V.; Dilys, J.; Lucinskis, A.; Tyshko, A.; Brazil, S. Hand-Held Magnetic Field Meter Based on Colossal Magnetoresistance-B-Scalar Sensor. *IEEE Trans. Instrum. Meas.* 2020, 69 (6), 2808–2815. https://doi.org/10.1109/TIM.2019.2932165.

[69] Haran, T.L.; Hoffman, R.B.; Lane, S.E. Diagnostic capabilities for electromagnetic railguns. *IEEE Trans. Plasma Sci.* 2013, 41, 1526–1532.

[70] Schneider, M.; Schneider, R.; Stankevic, V.; Balevicius, S.; Zurauskien, N. Highly Local Measurements of Strong Transient Magnetic Fields during Railgun Experiments Using CMR-Based Sensors. *IEEE Trans. Magn.* 2007, 43, 370–375.

[71] Schneider, M.; Liebfried, O.; Stankevic, V.; Balevicius, S.; Zurauskiene, N. Magnetic Diffusion in Railguns: Measurements Using CMR-Based Sensors. *IEEE Trans. Magn.* 2009, 45, 430–435.

[72] Žurauskaitė, L.; Balevičius, S.; Žurauskienė, N.; Keršulis, S.; Stankevič, V.; Šimkevičius, Č.; Novickij, J.; Tolvaišienė, S. Ageing effects on electrical resistivity and magnetoresistance of nanostructured manganite films. *Lith. J. Phys.* 2012, 52 (3), 224–230.

[73] Šimkevičius, Č.; Keršulis, S.; Stankevič, V.; Pavilonis, D.; Žurauskienė, N.; Balevičius, S.; Tolvaišienė, S. Accelerated ageing effects in nanostructured La0.83Sr0.17MnO3 films. *Thin Solid Films* 2015, 589, 331–337.

[74] Stankevič, V.; Šimkevičius, Č.; Keršulis, S.; Balevičius, S.; Žurauskienė, N.; Pavilonis, D.; Tolvaišienė, S. Improvement in the long-term stability of parameters of encapsulated magnetic field sensors based on LaSrMnO thin films. *Sens. Actuators A: Phys.* 2015, 228, 112–117.

[75] Saranya, A.M.; Pla, D.; Morata, A.; Cavallaro, A.; Canales-Vázquez, J.; Kilner, J.A.; Burriel, M.; Tarancón, A. Engineering mixed ionic electronic conduction in La0.8Sr0.2MnO3+δ nanostructures through fast grain boundary oxygen diffusivity. *Adv. Energy Mater.* 2015, 5, 1500377.

[76] Abdelmoula, N.; Guidara, K.; Cheikh-Rouhou, A.; Dhahri, E.; Joubert, J.C. Effects of the oxygen nonstoichiometry on the physical properties of La0.7Sr0.3$MnO_{3-\delta}$ manganites ($0 \leq \delta \leq 0.15$). *J. Solid State Chem.* 2000, 151, 139–144.

[77] De Souza, R.A.; Kilner, J.A.; Walker, J.F. SIMS Study of Oxygen Tracer Diffusion and Surface Exchange in La0.8Sr0.2MnO3+δ. *Mater. Lett.* 2000, 43, 43–52.

[78] Mira, J.; Rivas, J.; Breijo, M.P.; Rodriguez, M.A.S.; Sanchez, R.D. Effects of ageing on the electrical resistivity of $La_{1-x}B_xCoO_3$ perovskites (B=Sr, Ca, Ba; $0.20 \leq x \leq 0.30$). *Sens. Actuators A: Phys.* 2000, 81, 23–26.

[79] Markovich, V.; Jung, G.; Yuzhelevski, Y.; Gorodetsky, G.; Mukovskii, Y.M. Intrinsic metastability of low doped manganites: $La_{0.8}Ca_{0.2}MnO_3$ case. *Eur. Phys. J. B* 2005, 48, 41–46.

[80] Prokhorov, V.G.; Kaminsky, G.G.; Komashko, V.A.; Lee, Y.P.; Park, J.S.; Ri, H.C. Oxygen-deficiency-activated phase transition in a longaged $La_{0.8}Ca_{0.2}MnO_3$ film. *Appl. Phys. Lett.* 2002, 80, 2707–2709.

[81] Phillips, J.C. Stretched exponential relaxation in molecular and electronic glasses. *Rep. Prog. Phys.* 1996, 59, 1133–1207.

[82] Vakiv, M.M.; Shpotyuk, O.I.; Balitska, V.O.; Butkiewicz, B.; Shpotyuk, L.I. Ageing behavior of electrical resistance in manganite NTC ceramics. *J. Eur. Ceram. Soc.* 2004, 24, 1243–1246.

[83] Emelianova, E.V.; Hertogen, P.; Arkhipov, V.I.; Adriaenssens, G.J. A model of photoinduced anisotropy in chalcogenide glasses. *J. Non-Cryst. Solids* 2000, 266–269, 954–958.

[84] Balitska, V.O.; Butkievich, B.; Shpotyuk, O.I.; Vakiv, M.M. On the Analytical Description of Ageing Kinetics in Ceramic Manganite-Based NTC Thermistors. *Microelectron. Reliab.* 2002, 42, 2003–2007.

[85] Ferrari, A.C.; Bonaccorso, F.; Fal'ko, V.; Novoselov, K.S.; Roche, S.; Bøggild, P.; Borini, S.; Koppens, F.H.L.; Palermo, V.; Pugno, N.; Garrido, J.A.; Sordan, R.; Bianco, A.; Ballerini, L.; Prato, M.; Lidorikis, E.; Kivioja, J.; Marinelli, C.; Ryhänen, T.; Morpurgo, A.; Coleman, J.N.; Nicolosi, V.; Colombo, L.; Fert, A.; Garcia-Hernandez, M.; Bachtold, A.; Schneider, G.F.; Guinea, F.; Dekker, C.; Barbone, M.; Sun, Z.; Galiotis, C.; Grigorenko, A.N.; Konstantatos, G.; Kis, A.; Katsnelson, M.; Vandersypen, L.; Loiseau, A.; Morandi, V.; Neumaier, D.; Treossi, E.; Pellegrini, V.; Polini, M.; Tredicucci, A.; Williams, G.M.; Hong, B.H.; Ahn, J.-H.; Kim, J.M.; Zirath, H.; van Wees, B.J.; van der Zant, H.; Occhipinti, L.; Di Matteo, A.; Kinloch, I.A.; Seyller, T.; Quesnel, E.; Feng, X.; Teo, K.; Rupesinghe, N.; Hakonen, P.; Neil, S.R.T.; Tannock, Q.; Löfwander, T.; Kinaret, J. Science and Technology Roadmap for Graphene, Related Two-Dimensional Crystals, and Hybrid Systems. *Nanoscale* 2015, 7, 4598–4810.

[86] Li, F.; Huang, Y.; Huang, K.; Lin, J.; Huang, P. Functional Magnetic Graphene Composites for Biosensing. *Int. J. Mol. Sci.* 2020, 21, 390.

[87] Jayaprakash, G.K. Pre-Post Redox Electron Transfer Regioselectivity at the Alanine Modified Nano Graphene Electrode Interface. *Chem. Phys. Lett.* 2022, 789, 139295.

[88] Friedman, A.L.; Tedesco, J.L.; Campbell, P.M.; Culbertson, J.C.; Aifer, E.; Perkins, F.K.; Myers-Ward, R.L.; Hite, J.K.; Eddy, C.R.; Jernigan, G.G.; Gaskill, D.K. Quantum Linear Magnetoresistance in Multilayer Epitaxial Graphene. *Nano Lett.* 2010, 10, 3962–3965.

[89] Orlita, M.; Escoffier, W.; Plochocka, P.; Raquet, B.; Zeitler, U. Graphene in High Magnetic Fields. *C. R. Phys.* 2013, 14, 78–93.

[90] Wang, W.J.; Gao, K.H.; Li, Z.Q.; Lin, T.; Li, J.; Yu, C.; Feng, Z.H. Classical Linear Magnetoresistance in Epitaxial Graphene on SiC. *Appl. Phys. Lett.* 2014, 105, 182102.

[91] Liu, Y.; Yudhistira, I.; Yang, M.; Laksono, E.; Luo, Y.Z.; Chen, J.; Lu, J.; Feng, Y.P.; Adam, S.; Loh, K.P. Phonon-Mediated Colossal Magnetoresistance in Graphene/Black Phosphorus Heterostructures. *Nano Lett.* 2018, 18, 3377–3383.

[92] Wang, Q.; Gao, T.; Harumoto, T.; Ando, K.; Nakamura, Y.; Shi, J. Enhanced Room-Temperature Positive Magnetoresistance of Graphene by Decorating Co Particles on the Surface. *Mater. Lett.* 2021, 293, 129730.

[93] Hu, J.; Gou, J.; Yang, M.; Omar, G.J.; Tan, J.; Zeng, S.; Liu, Y.; Han, K.; Lim, Z.; Huang, Z.; Wee, A.T.S.; Ariando, A. Room-Temperature Colossal Magnetoresistance in Terraced Single-Layer Graphene. *Adv. Mater.* 2020, 32, 2002201.

[94] Hu, J.; Rosenbaum, T.F. Classical and Quantum Routes to Linear Magnetoresistance. *Nat. Mater.* 2008, 7, 697–700.

[95] Parish, M.M.; Littlewood, P.B. Non-Saturating Magnetoresistance in Heavily Disordered Semiconductors. *Nature* 2003, 426, 162–165.

[96] Parish, M.M.; Littlewood, P.B. Classical Magnetotransport of Inhomogeneous Conductors. *Phys. Rev. B* 2005, 72, 094417.

[97] Khouri, T.; Zeitler, U.; Reichl, C.; Wegscheider, W.; Hussey, N.E.; Wiedmann, S.; Maan, J.C. Linear Magnetoresistance in a Quasifree Two-Dimensional Electron Gas in an Ultrahigh Mobility GaAs Quantum Well. *Phys. Rev. Lett.* 2016, 117, 256601.

[98] Gopinadhan, K.; Shin, Y.J.; Jalil, R.; Venkatesan, T.; Geim, A.K.; Neto, A.H.C.; Yang, H. Extremely Large Magnetoresistance in Few-Layer Graphene/Boron–Nitride Heterostructures. *Nat. Commun.* 2015, 6, 8337.

[99] Liu, Y.; Yang, R.; Yang, H.; Wang, D.; Zhan, Q.; Zhang, G.; Xie, Y.; Chen, B.; Li, R.-W. Anomalous Anisotropic Magnetoresistance Effects in Graphene. *AIP Adv.* 2014, 4, 097101.

[100] Pezeshki, A.; Hamdi, A.; Yang, Z.; Lubio, A.; Shackery, I.; Ruediger, A.; Razzari, L.; Orgiu, E. Effect of Extrinsic Disorder on the Magnetoresistance Response of Gated Single-Layer Graphene Devices. *ACS Appl. Mater. Interfaces* 2021, 13, 26152–26160.

[101] Marozau, I.; Das, P.T.; Döbeli, M.; Storey, J.G.; Uribe-Laverde, M.A.; Das, S.; Wang, C.; Rössle, M.; Bernhard, C. Influence of La and Mn Vacancies on the Electronic and Magnetic Properties of $LaMnO_3$ Thin Films Grown by Pulsed Laser Deposition. *Phys. Rev. B* 2014, 89, 174422.

[102] Zurauskiene, N.; Stankevic, V.; Kersulis, S.; Klimantavicius, J.; Simkevicius, C.; Plausinaitiene, V.; Vagner, M.; Balevicius, S. Increase of Operating Temperature of Magnetic Field Sensors Based on La–Sr–Mn–O Films with Mn Excess. *IEEE Trans. Plasma Sci.* 2019, 47, 4530–4535.

[103] Cadieu, F.J.; Chen, L.; Li, B.; Theodoropoulos, T. Enhanced room temperature magnetoresistance response in textured $La_{0.7}Sr_{0.3}MnO_3$ strips made by pulsed laser deposition. *J. Appl. Phys.* 2000, 87, 6770–6772.

[104] Pradhan, A.K.; Roul, B.K.; Wen, J.G.; Ren, Z.F.; Muralidhar, M.; Dutta, P.; Sahu, D.R.; Mohanty, S.; Patro, P.K. Enhanced room-temperature magnetoresistance in partially melted $La_{0.67}Ca_{0.33}MnO_3$ manganites. *Appl. Phys. Lett.* 2000, 76, 763–765.

[105] Chen, A.; Zhang, W.; Jian, J.; Wang, H.; Tsai, C.-F.; Su, Q.; Jia, Q.; MacManus-Driscoll, J.L. Role of boundaries on low-field magnetotransport properties of $La_{0.7}Sr_{0.3}MnO_3$-based nanocomposite thin films. *J. Mater. Res.* 2013, 28, 1707–1714.

[106] Moshnyaga, V.; Damaschke, B.; Shapoval, O.; Belenchuk, A.; Faupel, J.; Lebedev, O.I.; Verbeeck, J.; van Tendeloo, G.; Mücksch, M.; Tsurkan, V.; Tidecks, R.; Samwer, K. Structural phase transition at the percolation threshold in epitaxial (La0.7Ca0.3MnO3)1−x:(MgO)x nanocomposite films. *Nat. Mater.* 2003, 2, 247–252.

[107] Wu, Y.J.; Wang, Z.J.; Ning, X.K.; Wang, Q.; Liu, W.; Zhang, Z.D. Room temperature magnetoresistance properties in self-assembled epitaxial $La_{0.7}Sr_{0.3}MnO_3$:NiO nanocomposite thin films. *Mater. Res. Lett.* 2018, 6, 489–494.

[108] Zhang, W.; Chen, A.; Khatkhatay, F.; Tsai, C.-F.; Su, Q.; Jiao, L.; Zhang, X.; Wang, H. Integration of selfassembled vertically aligned nanocomposite $(La_{0.7}Sr_{0.3}MnO_3)_{1-x:}(ZnO)_x$ thin films on silicon substrates. *ACS Appl. Mater. Interfaces* 2013, 5, 3995–3999.

[109] Staruch, M.; Gao, H.; Gao, P.-X.; Jain, M. Low-field magnetoresistance in $La_{0.67}Sr_{0.33}MnO_3$:ZnO composite film. *Adv. Funct. Mater.* 2012, 22, 3591–3595.

[110] Chen, A.; Bi, Z.; Hazariwala, H.; Zhang, X.; Su, Q.; Chen, L.; Jia, Q.; MacManus-Driscoll, J.L.; Wang, H. Microstructure, magnetic, and low-field magnetotransport properties of self-assembled $(La_{0.7}Sr_{0.3}MnO_3)0.5:(CeO_2)_{0.5}$ vertically aligned nanocomposite thin films. *Nanotechnology* 2011, 22, 315712.

[111] Kang, B.S.; Wang, H.; MacManus-Driscoll, J.L.; Li, Y.; Jia, Q.X.; Mihut, I.; Betts, J.B. Low field magnetotransport properties of $(La_{0.7}Sr_{0.3}MnO_3)_{0.5}:(ZnO)_{0.5}$ nanocomposite films. *Appl. Phys. Lett.* 2006, 88, 192514.

[112] Egilmez, M.; Saber, M.M.; Abdelhadi, M.; Chow, K.H.; Jung, J. Anomalous Ageing and Strain Induced Time Dependent Phenomena in Ultra-Thin La0.65Ca0.35MnO3 Films. *Phys. Lett. A* 2011, 375, 4049–4052.

[113] Schroder, D.K. *Semiconductor Material and Device Characterization*; 3rd ed.; John Wiley & Sons, 2005. https://doi.org/10.1002/0471749095.

[114] Zurauskiene, N.; Lukose, R.; Balevicius, S.; Stankevic, V.; Kersulis, S.; Plausinaitiene, V.; Vagner, M.; Navickas, R. Compact Manganite-Graphene Magnetoresistive Sensor. *IEEE Magn. Lett.* 2019, 10, 8105605.

[115] Dauber, J.; Sagade, A.A.; Oellers, M.; Watanabe, K.; Taniguchi, T.; Neumaier, D.; Stampfer, C. Ultra-sensitive Hall sensors based on graphene encapsulated in hexagonal boron nitride. *Appl. Phys. Lett.* 2015, 106, 193501.

Curriculum Vitae

Education:

2020–2026 — Center for Physical Sciences and Technology, Vilnius, Lithuania — Doctoral studies.

2018–2023 — National Technical University of Ukraine “Igor Sikorsky Kyiv Polytechnic Institute”, Kyiv, Ukraine — Doctoral studies.

2016–2018 — National Technical University of Ukraine “Igor Sikorsky Kyiv Polytechnic Institute”, Kyiv, Ukraine — Master’s degree.

2012–2016 — National Technical University of Ukraine “Igor Sikorsky Kyiv Polytechnic Institute”, Kyiv, Ukraine — Bachelor’s degree.

Vilniaus universiteto leidykla
Saulėtekio al. 9, III rūmai, LT-10222 Vilnius
El. p. info@leidykla.vu.lt, www.leidykla.vu.lt
bookshop.vu.lt, journals.vu.lt
Tiražas 25 egz.